UNIVERSIDADE DE LISBOA
FACULDADE DE CIÊNCIAS

Study of ground state properties of halo nuclei via quasi-free scattering reactions

" Documento Definitivo"

Doutoramento em Física

Paulo Jorge Fernandes Velho

Tese orientada por:
Prof. Doutor Daniel Galaviz Redondo
Prof. Doutora Maria Raquel Nunes Pereira Crespo
Prof. Doutora Adelaide Pedro de Jesus

Documento especialmente elaborado para a obtenção do grau de doutor

2019

UNIVERSIDADE DE LISBOA
FACULDADE DE CIÊNCIAS

Study of ground state properties of halo nuclei via quasi-free scattering reactions

Doutoramento em Física

Paulo Jorge Fernandes Velho

Tese orientada por:
Prof. Doutor Daniel Galaviz Redondo
Prof. Doutora Maria Raquel Nunes Pereira Crespo
Prof. Doutora Adelaide Pedro de Jesus

Júri:

Presidente:

- Doutora Margarida Maria Telo da Gama, Professora Catedrática, Faculdade de Ciências da Universidade de Lisboa

Vogais:

- Doutor Héctor Álvarez Pol, *Profesor Titular, Facultad de Física da Universidade de Santiago de Compostela*, Espanha
- Doutor Eduardo Garrido Bellido, *Investigador Científico*, *Instituto de Estructura de la Materia* (IEM), do *Centro de Física Miguel Antonio Catalan* (CFMAC) do *Consejo Superior de Investigaciones Científicas* (CSIC), Espanha
- Doutor Alberto Blanco Castro, Investigador Auxiliar, Laboratório de Instrumentação e Física Experimental de Partículas - LIP
- Doutor Sérgio Eduardo de Campos Costa Ramos, Professor Auxiliar, Instituto Superior Técnico da Universidade de Lisboa
- Doutor Daniel Galaviz Redondo, Professor Auxiliar, Faculdade de Ciências da Universidade de Lisboa (orientador)

Documento especialmente elaborado para a obtenção do grau de doutor

2019

Acknowledgments

I would like to thank Prof. Dr. Daniel Galaviz, Prof. Dr. Raquel Crespo and Prof. Dr. Adelaide Jesus for the orientation and co-orientation of this thesis work. I also would like to thank Dr. Micaela Fonseca, Dr. Helio Luís, Dr. Ana Henriques, Dr. Pamela Teubig, Dr. Jorge Machado, Dr. Pablo Cabanelas, Dr. Ángel Benitez and to all R^3B collaboration. Finally I would like to thank my friends and family, especially to Maria Inês Sardinha, Janete Velho, Agostinho Velho, Iolanda Velho, José Lucas and Teresa Matilde for their support.

Abstract

The main goal of this work was the analysis and interpretation of experimental data obtained for the reaction (p,pn) of the one neutron halo nucleus ^{15}C on a proton target. The measurement, performed at the GSI laboratory, was part of an experimental campaign (Experiment S393) of the R^{3}B collaboration and the first step towards the measurement of fully exclusive reaction cross sections on exotic nuclei.

The so-called halo nuclei are of high interest as they consist of bound nuclei characterized by one or more valence nucleons orbiting at larger distances from a core. These are novel quantum systems appearing at the limits of the dripline. Furthermore, halo nuclei are characterized by low separation energies, resulting in very narrow momentum distributions of the core in nucleon knockout reactions at relativistic energies.

One neutron-halo nucleus of particularly high interest is ^{15}C, which has a neutron separation energy of S_n = 1.218 MeV. Ground state and spectroscopic information have been extracted experimentally from Coulomb dissociation studies resulting in a consistent picture with a dominant (^{14}C(0^+) x $2s_{1/2}$) configuration. Momentum distributions of the core extracted from single neutron knockout reactions exhibited a width of 67 MeV/c, consistent with larger separation energy and the same dominant configuration. However, calculations failed to reproduce the tail of the measured momentum distributions. The momentum distributions are inclusive measurements and thus it is desirable to measure exclusive observables which incorporate more physics information.

The Faddeev/AGS formalism is a non-relativistic three-body multiple scattering framework that treats equally all opening channels (elastic, breakup and transfer) and has been used to assess the validity of approximations considered in traditional scattering frameworks. This has highlighted that traditional reaction approaches may not be adequate to study the nuclei under consideration. It was also successfully applied to the study of reactions involving halo nuclei as well as light/medium

nuclear systems.

The ^{15}C case, due to its dominant ground state configuration of ^{14}C core in its ground state and a s-wave valence neutron (^{14}C(0^+) x $2s_{1/2}$), constitutes a very suitable case to apply the Fadeev/AGS reaction formalism to the study of the ^{15}C.

Keywords

Halo nuclei, nuclear structure, quasi-free scattering, neutron knockout reactions.

Resumo

O principal objectivo do trabalho consiste no estudo da reacção ^{15}C(p,pn)^{14}C num alvo de protões. Serão apresentadas as distribuições de momento transverso, as distribuições angulares de protões e neutrões emergentes da reacção, a análise do espectro gamma da reacção assim como as secções eficazes obtidas pela a análise dos dados experimentais e a comparação com os valores teóricos previstos pelo formalismo Faddeev/AGS.

Os denominados núcleos halo são de elevado interesse e consistem num núcleo ligado caracterizado por terem um ou mais nucleões de valência a orbitar a grandes distâncias do seu "core". Estes são novos sistemas que aparecem nos limites do vale de estabilidade nuclear. Para além disso, estes núcleos apresentam energias de separação bastante baixas resultando em distribuições de momento estreitas em reações "knockout" a energias relativistas.

O ^{15}C é um núcleo halo que apresenta uma energia de separação do neutrão de valência de $S_n = 1.218$ MeV. A sua informação espectroscópica do estado fundamental foi extraída experimentalmente por reacções de dissociação colombiana resultando numa imagem consistente de uma configuração dominante (^{14}C(0^+) x $2s_{1/2}$), ou seja um "core" de ^{14}C no estado fundamental e um neutrão no estado $2s_{1/2}$. As distribuições de momento do "core" extraídas de reações "knockout" de um neutrão apresentaram uma largura (FWHM) de 67 MeV/c consistentes com a sua energia de separação da configuração dominante. Por outro lado, o formalismo Faddeev/AGS é um "framework" de dispersão múltipla não relativístico que trata de igual forma todos os canais da reacção (elástico, breakup e transfer) e que pode ser aplicado ao estudo de reacções nucleares com núcleos halo permitindo a obtenção da sua informação de estrutura nuclear, onde os formalismos mais tradicionais poderão não ser aplicaveis.

A campanha experimental S393 da colaboração R^{3}B realizou-se em 2010 no laboratório GSI em Darmstadt na Alemanha onde foram estudadas diferentes reacções com diversos isótopos exóticos com uma carga Z a variar entre ($4 < Z < 10$) e o

rácio massa por carga A/Z a variar entre ($1.5 < A/Z < 3$), utilizando-se o mesmo setup experimental. O feixe de núcleos exóticos foi produzido pelo método de "In-Flight Separation", onde um feixe primário de ^{40}Ar foi acelerado a aproximadamente 490 MeV/u e levado a incidir num alvo primário de Be com 4g/cm^2. Através de fragmentação nuclear foi produzido um feixe secundário contendo um "cocktail" de isótopos. Seguidamente os isótopos emergentes foram seleccionados através da sua rigidez magnética no "Fragment Separator" e guiados com aproximadamente 420 MeV/u para a "cave C" onde se encontra o setup experimental da colaboração R^{3}B. Este setup experimental onde se realizaram os primeiros testes de electónica, aquisição de dados e sistemas de detecção para o futuro FAIR, é baseado num sistema evento-por-evento que permite a detecção e medição de todas as partículas iniciais e finais envolvidas no processo, permitindo deste modo cobrir toda a cinemática da reacção. O feixe secundário, proveniente do "Fragment Separator" é caracterizado pela medição do tempo de voo e pela energia depositada em detectores antes do alvo. A área do alvo é coberta por uma "caixa" de oito detectores de silício para detecção de partículas carregadas e por um sistema de detecção em forma de esfera composto por 168 cristais de NaI, denominado "Crystal Ball". Este sistema é utilizado para a medição do espectro gamma assim como para a detecção de protões e neutrões (embora com baixa eficiência) na parte posterior do detector. Depois do alvo os produtos da reacção são separados pelo ALADIN, um dipolo magnético, em três ramos: os neutrões que seguem rectilineamente sem serem deflectidos pelo dipolo magnético são detectados no detector de neutrões LAND; No seguinte ramo os fragmentos pesados são por sua vez detectados através de dois detectores de fibra (GFIs) para reconstrução da sua trajectória. Os tempos de voo e energia depositada são medidos através de um sistema com vários cintiladores de plástico (TFW); Finalmente no ramo dos protões existem dois sistemas de detecção (PDCs) que são responsáveis pela medição da trajectória dos protões e o sistema (DTF) uma parede de cintiladores responsável pela medição de tempos de voo e energia depositada.
Esta tese apresenta a calibração de alguns dos sistemas de detecção utilizados focando-se na análise de dados experimentais obtidos e os seus resultados. A análise dos dados experimentais foi interpretada de acordo com dois processos distintos. Por um lado o denominado "Particle exclusive Neutron Knockout", onde os fragmentos pesados são detectados na "TFW" e as partículas emergentes da reacção (protão e neutrão) são detectados na "Crystal Ball". Por outro o denominado "Particle inclusive Neutron Knockout", onde apenas os fragmentos pesados foram detectados

utilizando-se o sistema "TFW". Neste caso o processo foi estudado através de dois métodos diferentes. Primeiro os dados experimentais foram analisados sem que se tenha requerido qualquer sinal no detector "Crystal Ball". Posteriormente através da análise dos dados experimentais foi requerido um sinal na "Crystal Ball" embora não se tenha requerido qualquer condição relativa a protões ou neutrões neste mesmo detector.

Através da análise dos dados experimentais foram determinadas as distribuições de momentum transverso e a sua largura (FWHM) para a reacção ^{15}C(p,pn)^{14}C realizada com um alvo de CH_2, de Carbono e fazendo a subtração da contribuição do Carbono no alvo de CH_2, determinaram-se os valores para a reação com protões. Obtiveram-se as larguras de (43±10) MeV/c para o alvo de CH_2 e de (35±10) MeV/c para o alvo de Carbono. Da mesma maneira foi calculada a secção eficaz para a reacção com os diferentes alvos tendo em conta se era "Particle exclusive Neutron Knockout" ou "Particle inclusive Neutron Knockout". No primeiro caso obteve-se uma secção eficaz de (35±4) mb para protões, de (101±3) mb para o alvo de Carbono e de (172±3) mbarn para CH_2. Estudou-se também a distribuição angular para os protões e neutrões emergentes da reacção tendo-se identificado a assinatura do regime "quasi-free". No caso de "Particle inclusive Neutron Knockout" obteve-se uma secção eficaz de (72±19) mb para protões, de (225±14) mb para o alvo de Carbono e de (369±12) mbarn para o alvo de CH_2. Analisou-se o espectro de energia Gamma proveniente da exitação dos fragmentos de ^{14}C após a reacção. O espectro obtido experimentalmente foi comparado com o espectro simulado para os Gammas de interesse. Calculou-se a distribuição de momento em coicidência com os eventos relacionados com o pico Gamma de 6.09 MeV, obtendo-se uma largura FWHM de 97.61 MeV/c. Conclui-se deste modo que uma grande parte dos Gammas emitidos provêm da remoção e exitação de um neutrão interior do core. Os resultados experimentais das secções eficazes foram comparados com cálculos teóricos utilizando o formalismo Faddeev/AGS para uma onda s e uma onda p, obtendo-se os factores

de normalizaçao de 0.56 para a onda s e de 1.31 para a onda p.

Palavras Chave

Núcleos halo, estrutura nuclear, dispersão quase-livre, reacções knockout do neutrão.

Contents

List of Figures

List of Tables

Acronyms

ADC Analog to Digital Converter

ALADIN A Large DIpole magNet

DAQ Data AcQuisition

FRS FRagment Separator

FWHM Full Width at Half Maximum

GFI Groess FIiber Detektor

LAND Large Area Neutron Detector

PDCs Proton Drift Chambers

PSP Position Sensitive Pin diode

QDC Charge to Digital Converter

QFS Quasi Free Scattering

RIBs Radioactive Ion Beams

SST Silicon Strip Tracker

TDC Time to Digital Converter

TFW Time of Flight Wall

1

Introduction

Contents

In 1896 Henri Becquerel discovered the radioactivity. However, the concept of an atomic nucleus was suggested by Ernest Rutherford [1] in 1911 and then it was proved that the nucleus is build of neutrons and protons by Chadwick in 1932 [2]. These discoveries contributed for the beginning of a new research field, Nuclear Physics. In sequence, some theoretical nuclear models as the "liquid-drop model" and the "shell model" were developed to explain the properties of nuclei in terms of the arrangement of their intrinsic constituents, the protons and neutrons and to describe the structure of nuclei.

Nowadays it is known that the nucleus is characterized by its number of protons (Z) which defines each element and can have many isotopes according to its number of neutrons (N). Many isotopes have been predicted and identified. In figure 1.1 it is shown the chart of observed nuclides, where the horizontal axe represents the number neutrons and the vertical axe the number of protons. The black cells represent the stable nuclei while the colourful cells represent the radioactive isotopes according with their half-life.

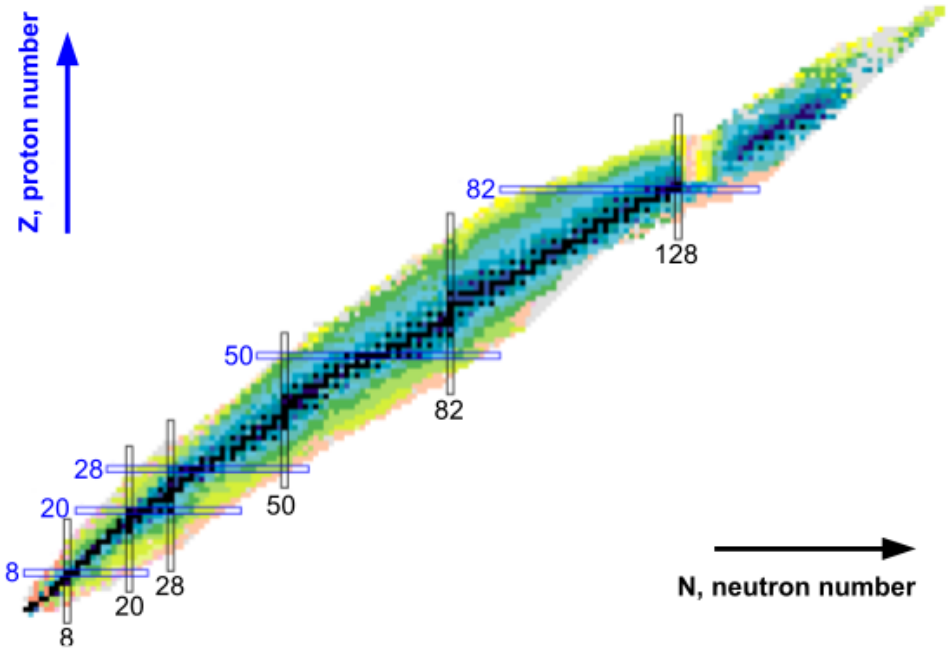

Figure 1.1: Chart of nuclides. On the horizontal axe is represented the number neutrons (N) and in the vertical axe the number of protons (Z). Image from National Nuclear Data Center, information extracted from the Chart of Nuclides database [3].

In the last decades the knowledge of atomic nuclei has benefited from new technological advances and experimental methods. With the advent of Radioactive Ion Beams (RIBs) it became possible to explore nuclei far away from the stability line where the exotic nuclei were discovered. These have allowed a deeper understanding of the nucleus and their nuclear interactions allowing a better understanding of the nuclear structure. However there are still many questions waiting for an answer. A particularly interesting phenomenon that is attracting the interest of nuclear physicists worldwide is the so called halo nuclei. These are novel quantum systems appearing close to the limits of nuclear existence, the so-called drip-lines. One neutron-halo nucleus of particularly high interest for this work is ^{15}C which, due to its simplicity can provide a very suitable case to test the Faddeev/AGS reaction formalism. This will be detailed in section 1.5 .

The presented thesis on the field of nuclear-structure physics has a special focus on the study of ^{15}C halo nuclei through nuclear knockout reactions at relativistic energies. The main part of the work consists in the analysis of experimental data obtained for the (p,pn) reaction of the one neutron halo nucleus ^{15}C on a proton target. The measurement, performed at the GSI laboratory, was part of S393 experimental campaign of R^{3}B collaboration.

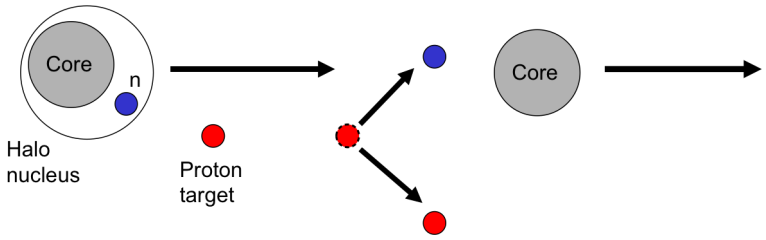

Figure 1.2: Schematic representation of ^{15}C(p,pn)^{14}C QFS reaction.

The next sections of this chapter are dedicated to the presentation of theoretical and experimental arguments that introduce to the relevant ideas addressed into this work. In the first section it will be done a small introduction to the nuclear structure, followed to the halo nuclei. Than nuclear breakup reactions will be introduced. The sections 1.4 and 1.5 are dedicated to the quasi free scattering and to the Faddeev/AGS formalism. Finally the last section of this chapter is dedicated to the explanation of the aim of this work, as to review the experimental information obtained in previous experiments concerning ^{15}C.

1.1 Nuclear structure

For the understanding of the nuclear structure many theoretical models have been proposed. The two most popular theoretical models are the liquid-drop model proposed by Bethe and Bacher in 1936 and the nuclear shell model developed by Goeppert-Mayer [4] and Jensen [5] in the 1940s.

The first considers the nucleus as a drop of charged incompressible fluid made by protons an neutrons which are held together by the nuclear force. This model could predict atomic masses and binding energies and explain the spherical shapes of many nuclei however it is not able to reproduce the properties of the lighter nuclei and also mismatch the combination of protons and neutrons numbers 2, 8, 20, 28, 50, 82 and 126 known as magic numbers, which was empirically observed that are responsible for a tightly bound nuclei with very high stability. In order to explain this, it was suggested the concept of nucleons following the atomic energy levels that had already been observed for electrons and a shell structure similar to the atoms.

The nuclear shell model is an example of an independent single particle model that assumes that each nucleon moves independently in a mean field potential, which is created by all other nucleons and obeying the Pauli's exclusion principle. Each nuclear level is described by a single configuration of quantum numbers.

By using the spherically symmetric Woods-Saxon potential where V_0 is the central depth of the potential and the two parameters R and a are the radius at which it has half the value of its central depth and its diffuseness, only some magic numbers are reproduced.

$$V(r) = -\frac{V_0}{1 + e^{(r-R)/a}} \tag{1.1}$$

The explanation to all of these magic numbers appeared with the inclusion of a spin-orbit coupling term [6]. A nucleon with angular momentum l and spin s will experience an additional potential.

$$V(r) = -\frac{V_0}{1 + e^{(r-R)/a}} + V_{ls}(r)LS \tag{1.2}$$

$$V_{LS} = C_{LS}(r) l.s \tag{1.3}$$

which will lead to an energy splitting (eq. 1.4).

$$\Delta E_{LS} = (l + \frac{1}{2})\hbar^2 C_{LS}(r) \tag{1.4}$$

Figure 1.3 shows the scheme of energy levels.

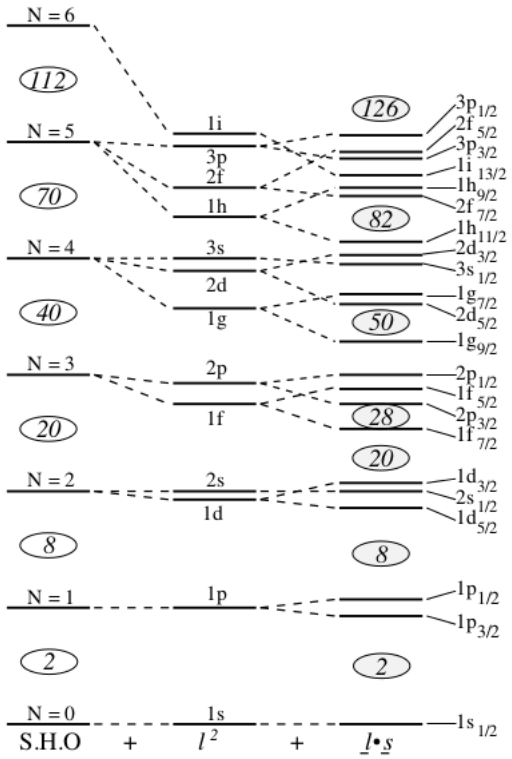

Figure 1.3: Scheme of low energy levels. In the left the energy levels in a Spherical Harmonic Oscillator. In the center the inclusion of orbital angular Momentum and in the right a better reproduction of the energy levels with the introduction of spin-orbit coupling. Image adopted from [7].

This was the first theory to successfully describe the properties of a large number of atomic nuclei, but only close to magic numbers, and not very far from the line of stability. When approaching exotic nuclei, which are nuclei close to the drip-lines signs of different magic numbers have been seen.

1.2 Halo nuclei

Halo nuclei are novel quantum systems appearing close to the limits of nuclear existence, the so-called drip-lines. Furthermore, these are characterized by low separation energies as they consist of bound nuclei with one or more valence nucleons orbiting at considerable large average distances from a compact core [8–15].

The first halo nuclei produced in laboratory was the ^{6}He, in 1936, using a beam of neutrons on a ^{9}Be target [16] just a few years after the discovery of the neutron. Nevertheless the concept of halo nuclei just appeared in 1987 with Hansen and Jonson paper [17] where the key ingredient of halo nuclei structure was identified. However the work of Tanihata [18] and their co-workers done 2 years before on the measurement of the very large interaction cross sections of certain neutron-rich isotopes of helium and lithium had a big importance for the subject. Since this period until nowadays the halo nuclei is a timely topic in nuclear physics motivating a big excitement of experimentalists and theorists and many papers.

A more refined concept is that the total many-body wave function must have at least 50% of its probability density outside the range of the core potential i.e. the probability to be found in a cluster structure and the outer part of the system in a classical forbidden region due to a quantum mechanical tunnelling [16, 19].

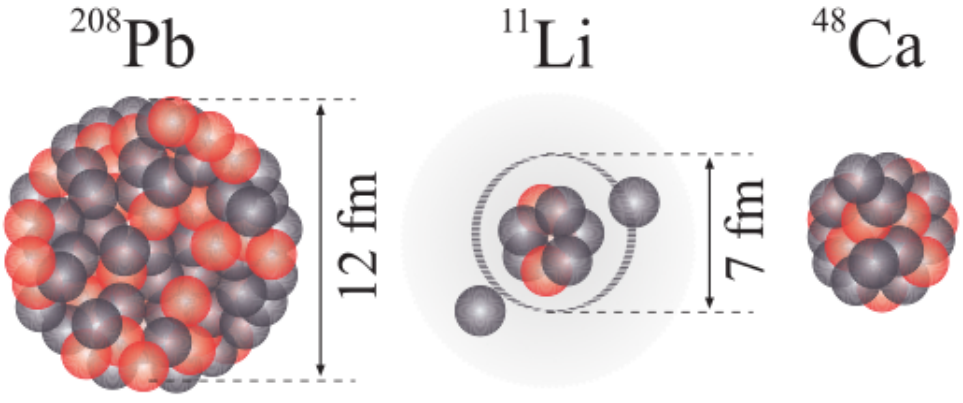

Figure 1.4: Comparison of nuclei sizes of ^{208}Pb, ^{11}Li and ^{48}Ca. Image adopted from [8].

Consequently these systems are loosely bound, so the halo structure in some sense can be understood as a threshold effect, and the separation energy Sn to

remove the halo particle(s) from the core, is an important parameter. In such structures the mean field approaches and the the shell model breaks down. The most useful theoretical approach is to use few-body structure models of a core plus valence particles which can better describe the most general properties of these nuclei, such as their separation energies, large size and breakup cross sections [19].

One neutron-halo nucleus of particularly interest for this work is ^{15}C. The particular focus of this thesis is set on this isotope and more detailed information about it will be described on section 1.5.

1.3 Direct nuclear reactions

In some reactions a incident particle interacts successively with a number of nucleons until most of its energy has been shared among many nucleons, initiating a cascade of collisions. In this extreme, the randomness is introduced by many collisions involving many nucleons. At the opposite side the so-called direct nuclear reactions are reactions in which the incident particle interacts with few nucleons or just a single nucleon producing a very little change between initial and final states of the nucleus [20]. These reactions, localized predominantly in the nuclear surface, have been used since 1940's to probe the single particle components of the nuclear wave function [21,22]. Firstly were used to probe stable nuclei in normal kinematics, more recently however they were applied to radioactive beams in inverse kinematics where the heavy particle is the projectile [23].

Several types of direct nuclear reactions which have been used with success in the past like elastic, inelastic, transfer and knockout reactions [22] offer different sort of sensitivity, however this work will focus on One Nucleon Knockout reactions and Quasi-Free Scattering reactions which are the ones more relevant for this work.

1.3.1 One nucleon knockout reactions

These reactions, often termed as one nucleon removal reactions, have been used to study shell structure information of exotic nuclei from reactions with light tar-

gets [8, 21]. In this kind of mechanism the projectile transfers a large momentum to a fragment nucleon, knocking out the nucleon while the fragment remains as an unaffected spectator. In the rest frame of the projectile, the recoil momentum of the nucleon is similar to the fragment momentum, however in opposite direction [24].

$$\vec{p}_{nucleon} = -\vec{p}_{fragment} \tag{1.5}$$

The fragment momentum distribution and its reaction channel cross-section reflects the knocked out nucleon wave function. The shape of the momentum distribution depends on its orbital as well as its separation energy. The width is narrower when the separation energy is smaller [20].

Information obtained experimentally together with theoretical reaction mechanism provides shell structure information. Glauber reaction framework that relies upon the eikonal and the adiabatic approximation. [21], has been often applied. However in this work, the used one is the Faddeev/AGS formalism [25–27] which will be described in section 1.4.

1.3.2 Quasi-free scattering

This section describes the quasi-free scattering reaction mechanism, which was introduced by O. Chamberlain and E. Segrè [28] and J. B. Cladis, W. N. Hess, and B . J. Moyer in 1952 at the Berkeley laboratory [29]. In these first experiments a proton beam with an energy of 340 MeV impinged in a lithium target. In the reaction process, proton pairs with approximately 90° of opening angle were detected.

Quasi Free Scattering (QFS) characterizes a scattering process where a bound nucleon or a cluster (^{2}H, ^{4}He, ^{8}Be) is knocked out from a nucleus, by a high energy particle as a proton or electron of several hundred MeV, and the remaining nucleus maintains unaffected as if both particles were free [30]. This can be explained due to the fact that the projectile de-Broglie wavelength at these energies is smaller than the average distance between two nucleons inside the nucleus. At these conditions,

by approximation it can be said that the quasi-free scattering corresponds to the case in which one nucleon-nucleon collision occurs instead of nucleon-nucleus. Moreover, in opposition to the one nucleon knockout, this mechanism allows the investigation of deeper regions inside the nucleus [31, 32].

Figure 1.5 represents the quasi-free process in inverse kinematics in the lab frame. In this work specific case, the projectile is the ^{15}C nucleus which is painted in pink with the halo neutron in green and the target is the nucleon (proton) in blue. Inside in red it is represented the ^{14}C core which is the remaining nucleus after the reaction. The vectors, $\vec{p}_1$ and $\vec{p}_2$ represents the momentum of the two nucleons (proton and neutron) after the reaction, and $\vec{p}_3$ represents the remaining nucleus after the reaction (^{14}C core).

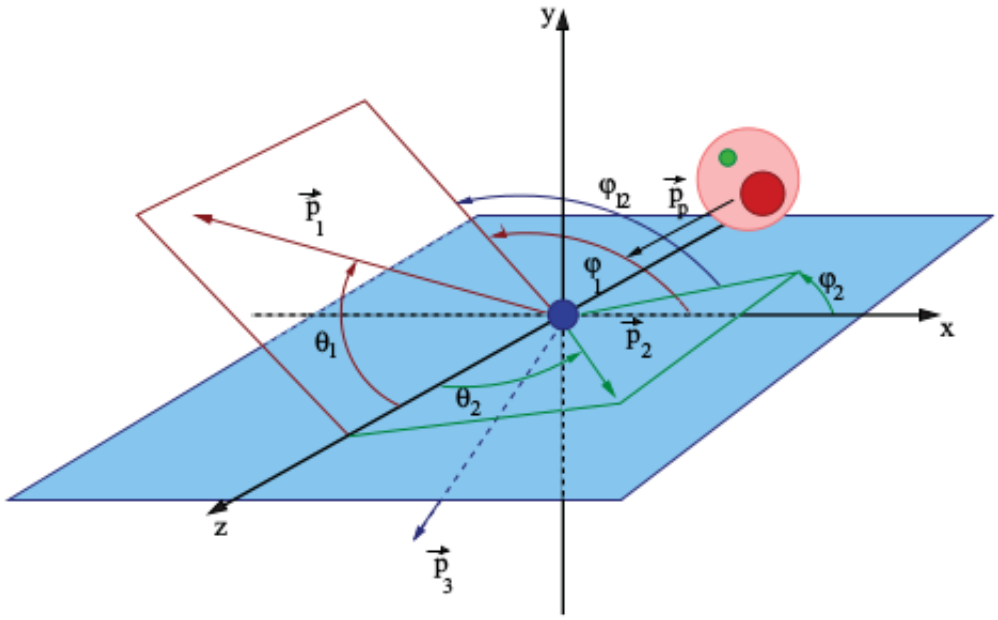

Figure 1.5: Representation of QFS mechanism in inverse kinematics in the lab frame. The figure was extracted from [33].

The vector direction for each nucleon is given in spherical coordinates by polar angles, θ and azimuthal anles, φ. The angular correlation between the two nucleons in this mechanism is characterized by opening angles $(\theta_1 + \theta_2)$ of approximately 90° [32], (however not exactly 90° as the proton in the target is not at rest [28]) and the azimuthal difference ($\varphi_1 - \varphi_2$) of approximately 180° (coplanarity).

1.4 The Faddeev/AGS formalism

Reaction theory is an important tool to interpret experimental data. Several standard approaches have been used in order to extract reliable structure information [34]. However some traditional reaction approaches may not be adequate to study the nuclei under consideration [35].

The few-body Faddeev/Alt-Grassberg-Sandhas (Faddeev/AGS) reaction formalism [25–27] is a non-relativistic three-body multiple scattering framework which can be viewed as a multiple scattering expansion in terms of the off-energy-shell transition amplitudes for each interacting pair, thereby including all higher order rescattering terms [36]. This approach which allows the calculations of inclusive, semi-inclusive, and fully exclusive cross sections treats equally all opening channels, elastic, breakup and transfer [36]. More recent developments permitted the incorporation of the Coulomb interaction in two of the interacting pairs [37, 38].

Faddeev/AGS reaction framework was successfully applied to the study of neutron/proton knockout reactions of light particles including halo nuclei, with a proton target at different energies [33, 36, 37, 39–42].

1.5 Nuclear reactions on the ^{15}C halo nucleus

The present PhD Thesis work focuses on the one neutron halo nucleus ^{15}C, which was studied through the ^{15}C(p,pn)^{14}C breakup reaction at relativistic ($\approx$400 MeV/u) energies.

The nucleus ^{15}C contains 6 protons and 9 neutrons and it's half life is 2.449 s. Its ground state is $J^{\pi} = 1/2^{+}$, (due to an inversion of the $1d_{5/2}$ and $2s_{1/2}$ shells) and presents a consistent picture with a dominant (^{14}C(0^{+}) x $2s_{1/2}$) configuration. The valence neutron extends far from the ^{14}C core, presenting a separation energy of $S_n = 1.218$ MeV. Figure 1.6 shows the schematic neutron levels configuration for the ground state of ^{15}C.

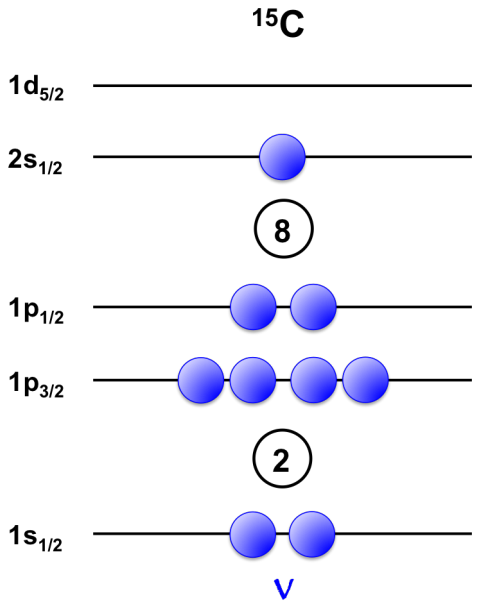

Figure 1.6: Schematic neutron levels configuration for the ground state of ^{15}C.

Momentum distributions widths and spectroscopic factors of the weakly-bound ^{15}C ground state are important references which were experimentally extracted in different works [35, 43–48] by means of different reaction mechanisms. A selection of relevant works that studied the halo nucleus by means of nuclear reactions is presented:

- The experiment performed by J. D. Goss [44] at University of Notre Dame used 14 MeV deuteron beam on a ^{14}C target to study the angular distributions for the ^{14}C(d,p)^{15}C transfer reaction, leading to the two bound states and eight of the unbound states of ^{15}C. A spectroscopic factor of 0.99 for the $1/2^+$ ground state was obtained.

- In other measurements carried out at the Notre Dame tandem accelerator, G. Murillo [43] studied^{14}C (d, p)^{15}C reaction at 16.0 MeV. The inelastic-scattering data have been analyzed using the DWBA and the $1/2^+$ g.s. and the $5/2^+$ state, extracted spectroscopic factors of 0.99 and 0.90 respectively.

- J. A. Tostevin [35] studied at the National Superconducting Cyclotron Laboratory at MSU [49] the neutron removal reaction of ^{15}C on a ^{9}Be target at 54

MeV/nucleon. Cross sections and momentum distributions were obtained, as well as spectroscopic factors of 0.99 and 1.03.

- U. Datta Pramanik [45] performed the Coulomb breakup of ^{15}C on a beryllium target at energies around 600 MeV/nucleon at GSI [50], Darmstadt. A narrow momentum distribution (67 $\pm$ 3) MeV/c of the fragment ^{14}C and a spectroscopic factor of 0.92 was reported.

- The neutron capture reaction on ^{14}C leading to the ground state in ^{15}C, has been studied by T. Nakamura [46] at the RIPS facility [51] at RIKEN [52]. The Coulomb breakup reaction of ^{15}C on a Pb target at 68 MeV/u leaded to a ^{14}C g.s. spectroscopic factor of 0.91.

- The halo nucleus ^{15}C was investigated by D. Bazin [47] at MSU [49]. In this experiment the halo structure was probed using a beam of ^{15}C on Be and Ta targets at 85 MeV/u. Momentum distributions of the core extracted from single neutron knockout reactions exhibited a broader width of 67 MeV/c, consistent with larger separation energy and the same dominant configuration. However, calculations failed to reproduce the tail of the measured momentum distributions.

- A systematic investigation of one neutron removal reactions was carried out by E. Sauvan [53] at GANIL [54]. Longitudinal momentum distributions and corresponding single-neutron removal cross sections were measured. A FWHM of (63.5$\pm$0.7) MeV/c was measured for the ^{15}C neutron removal at 62 MeV/u on a Carbon target.

The ^{15}C case is therefore a very useful test case with a relatively pure single-particle ground state [35], dominated by a (^{14}C(0^+) x $2s_{1/2}$) configuration, providing a very suitable case to test the Fadeev/AGS formalism considered for this study.

Aiming to shed light on the reaction mechanism, this work investigates the knockout of inner and valence shells neutrons on a proton target at relativistic

energies with a dominant quasi-free scattering behavior.The experimental study of the ^{15}C (p,pn) ^{14}C reaction was performed at the GSI [50] facility, in the LAND-R^{3}B setup [55] during the so-called S393 experimental campaign [56] which took place during 21 days at the summer of 2010.

1.6 Thesis outline

This thesis is structured in 8 chapters, which will be briefly described below. In Chapter 1, it is presented a theoretical introduction of some important concepts and background, to better understand this work. In Chapter 2, is given a detailed description of the experimental setup and campaign, including a brief description of each detector system. Chapter 3 contains the descriptions of the calibration and data reconstructions. The methodology is explained in Chapter 4. In Chapter 5, it is present the results, and its discussion is performed. The comparison of experimental and theoretical results is given in Chapter 6. In Chapter 7, it is presented the conclusions of this work and an outlook. Finally, in chapter 9, we present a synopsis.

2

S393 Experiment at LAND-R^{3}B Setup

Contents

In this chapter, the GSI (Helmholtzcenter for Heavy Ion Research) [50] facility, the LAND-R^{3}B setup [55] and the so-called S393 experimental campaign [56] which took place during 21 days at the summer of 2010 will be introduced. Furthermore the detector systems of LAND-R^{3}B setup will be described in detail.

2.1 The S393 experimental campaign and the GSI Heavy-Ion accelerator facility

The S393 experimental campaign entitled "Neutron-rich nuclei at and beyond the dripline in the range Z=4 to Z=10, studied in kinematically complete measurements of direct reactions at relativistic energies" [57] proposed by the R^{3}B (Reactions with Relativistic Radioactive Beams) collaboration was performed in the summer of 2010 during 21 days of beam time at the GSI facility. The campaign aimed to investigate light neutron-rich nuclei using inverse and complete kinematic measurements at relativistic energies.

During the beam time several exotic nuclei, covering ($4 < Z < 10$) and ($1.5 < A/Z < 3$) were produced simultaneously in a cocktail beam and investigated by means of different reactions mechanisms using the same experimental setup. First results have been published [31, 58–75]. Figure 2.1 shows the approximated region of produced isotopes. One important topic was the study of knockout reactions to investigate the evolution of shell structure near the dripline.

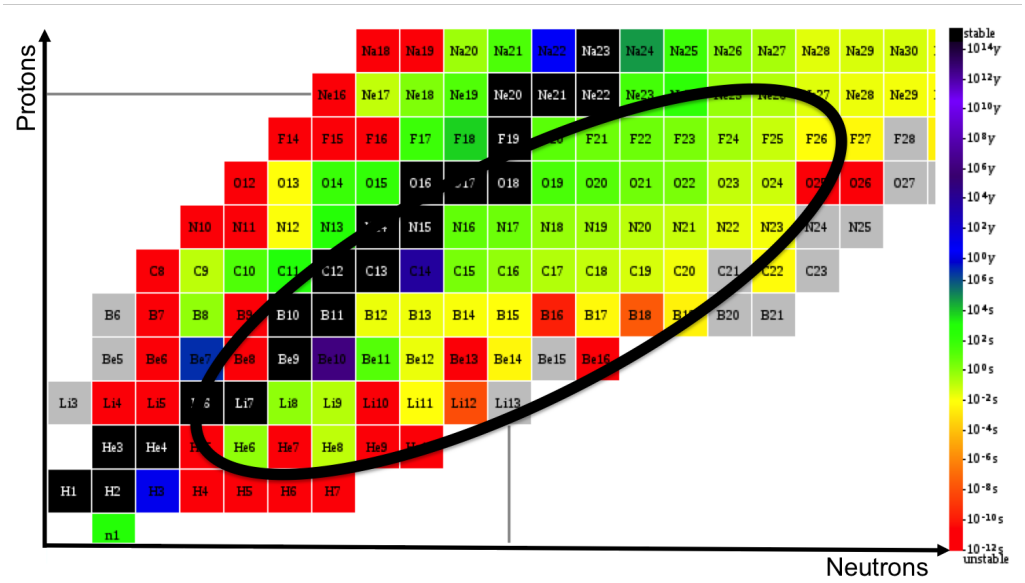

Figure 2.1: Aproximated region of produced isotopes to be study by different reaction channels during the S393 experimental campaign.

As mentioned the S393 campaign was carried out at GSI, a heavy ion accelerator facility located in Darmstadt, Germany. Represented in figure 2.2, this facility allows the production of all sort of stable and radioactive ion beams and can accelerate them at low or as well at relativistic energies. These isotope beams may be used to the research in several fields as nuclear and atomic physics, plasma, materials research, biophysics or even for medical purposes of cancer treatment.

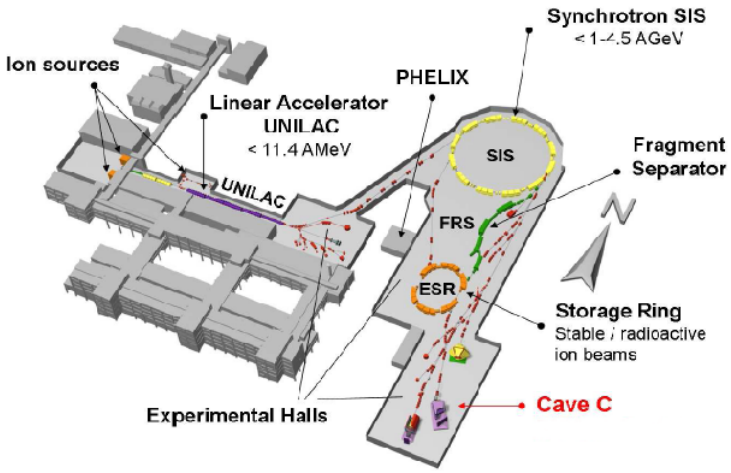

Figure 2.2: Overview of the GSI facility complex. The experimental hall marked as "cave C" indicates the location of the R^{3}B experiment, where S393 took place.

The low-energy primary ion beam can be produced in one of the three ions sources and accelerated by the UNILAC "Universal Linear Accelerator" [76] up to a maximum energy of 11.4 AMeV. At this stage the beam can be used for low-energy experiments or delivered to SIS-18 (Schwer-Ionen-Synchrotron) a Heavy-Ion-Synchrotron [77] which can accelerate the beam to energies of 4.5 AGeV for hydrogen, or 1 AGeV for uranium. This high-energy primary beam may be directly transported to an experimental hall and be used for various purposes, or ir can be injected into the FRS [76], a high resolution forward spectrometer [78] where the secondary beams of radioactive isotopes are produced by the In-Flight Separation method.

At the FRS entrance it is positioned a production target where the primary beam impinges and by nuclear fragmentation, several fragments result. The separation of the isotopes of interest is made according to their mass-to-charge ratio (A/Q) i.e. their magnetic rigidity, and they are then guided to the desired experimental setup. Figure 2.3 shows a schematic view of the FRS area.

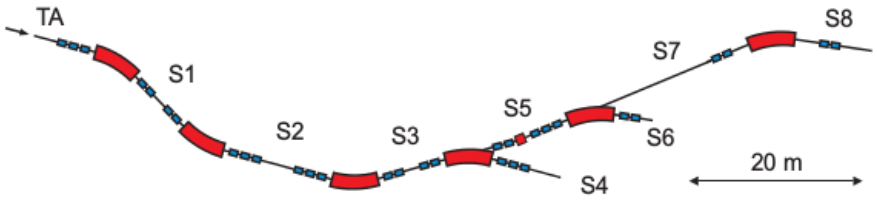

Figure 2.3: Schematic draw of FRS. In red are represented the magnetic dipoles. The beam coming from the SIS impinges in a primary target and the fragments are selected according to their magnetic rigidity.

In the work discussed in this thesis, a primary beam of ^{40}Ar was created and delivered to SIS-18 [77] where it was accelerated up to 490 MeV/u and guided towards a 4.011 g/cm^2 Be production target at FRS. In this area the fragments resulting from the nuclear fragmentation were selected according to a A/Z ratio of 1.5 (setting 3 of FRS). The secondary beam with a "cocktail" of stable and exotic nuclei at approximately 420 MeV/u was guided to the experimental setup used by the R^{3}B collaboration at the cave C of GSI, the so-called LAND-R^{3}B setup in which first tests (electronic, data acquisition and detection devices) for the future FAIR [79] were performed while still doing frontier research studying the properties of exotic nuclei.

2.2 LAND-R^{3}B experimental setup at cave C

In this section details concerning the detector systems involved in the S393 experiment and the LAND-R^{3}B experimental apparatus at the cave C will be addressed. This experimental setup, shown in the schematic figure 2.4 is based on event-by-event and exclusive measurement of all initial and final particle states covering the complete reaction kinematics.

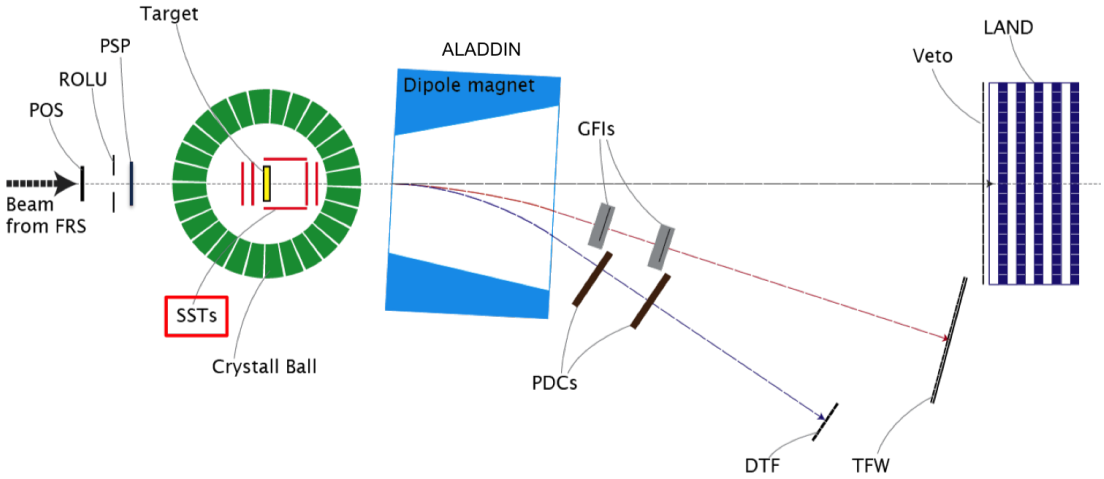

Figure 2.4: Schematic view of the LAND-R^{3}B setup in the cave C of GSI.

The secondary beam at relativistic energies which is coming from the FRS is characterized by measuring its time-of-flight and energy loss before reaching the secondary target at cave C. The detectors at the entrance of the hall (POS,ROLU and PSP) together with the S8 scintillator positioned in the FRS area (Figure 2.3) are responsible for the characterisation of the beam. These measure its position, time-of-flight and energy loss, which allows to distinguish the different isotopes coming into the "cocktail" beam.

The target area is covered by a box of eight silicon-strip detectors (SSTs), devoted to detect charged fragments, and a 4π-NaI detector for gammas and protons (the Crystal Ball). After the target the reaction products are separated by the dipole magnet - A Large DIpole magNet (ALADIN) - into three branches: neutrons measured by the Large Area Neutron Detector (LAND), heavy ions measured by the Time of Flight Wall (TFW) and GFI detector systems, and protons measured with DTF and Proton Drift Chambers (PDCs) detectors.

Details about the detection systems will be shown in the next subsections which will be divided in three parts according to their location at the experimental setup (either before, surrounding or after the target). The description of the detection systems after the target will be divided subsequently in three branches. The branch of heavy fragments, being more relevant for this work will be explained in more detail.

2.2.1 Detector systems before the target

In this subsection the detector systems POS, ROLU and PSP positioned before the target area will be described. These systems are used to identify and characterize the incoming isotopes in the beam.

2.2.1.A POS

The POS detector [80] is a square scintillator with (5.5 x 5.5) cm^2 (Figure 2.5). It is used for the time-of-flight measurements. The scintillation light produced in the detector is read-out by four photomultipliers, which deliver time and energy signals. Together with the S8 plastic scintillator placed in FRS, it gives time-of-flight measurements which are used for the identification of the incoming isotopes.

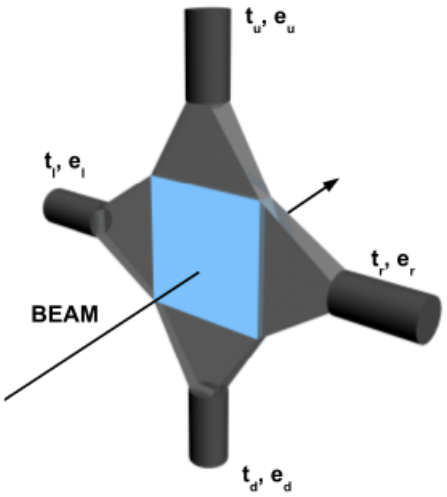

Figure 2.5: Schematic view of POS detector. The four photomultiplier outputs provide time and energy information. This detector is used to calculate time-of-flight, position and energy loss.

2.2.1.B ROLU

The ROLU detector [80] is a combination of four plastic scintillator slits placed after the POS detector. ROLU is an acronym in German for “R” (Rechts), “O”

(Oben), “L” (Links) and “U” (Unten) which means correspondingly to Right, Up, Left and Down referring to the position of the slit with respect to the the beam position. Each scintillator has (20 × 20 × 5) mm ^{3} and is read out by a photomultiplier from one side (figure 2.6).

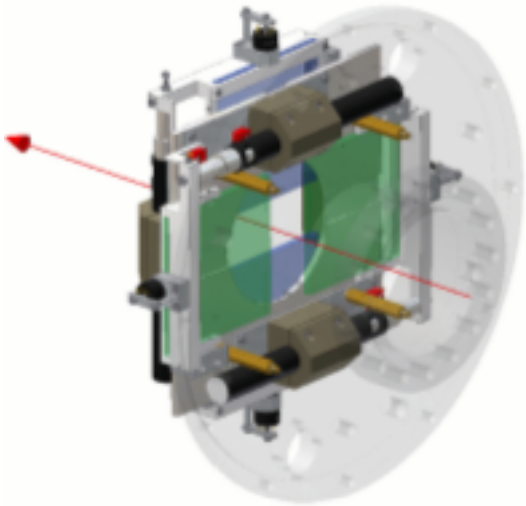

Figure 2.6: Schematic view of ROLU, the system based on four plastic scintillator slits which are working as a veto.

This system works as a veto detector since its signals enter in the trigger matrix in a way that events which fired ROLU will be rejected. By moving the slits of ROLU it is possible to control the beam size.

2.2.1.C PSP

The next in-beam detector is the Position Sensitive Pin diode (PSP) [80] placed just before the scattering chamber. This detector is an n-type silicon diode, with dimensions 45 × 45 × 0.3 mm^3 and has four anodes (Q1, Q2, Q3 and Q4) in the front side, to reconstruct the position of the ions, and one cathode (Q) which is used to identify the ions in charge. A schematic drawing of the PSP detector is shown in figure 2.7.

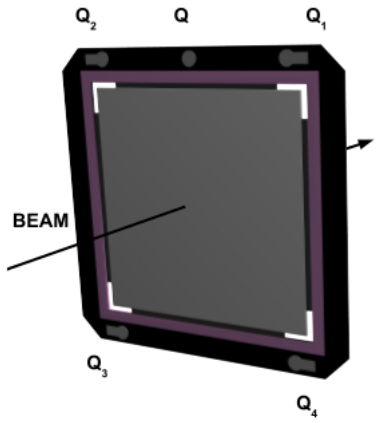

Figure 2.7: Schematic drawing of the PSP detector.

2.2.2 Detector systems around the target

Surrounding the target there are two detector systems: the Crystal Ball, a 4π-NaI detector; eight Double Side Silicon strip Detectors (SSTs). The first one is used to the detection of gamma-rays, protons, light charged particles and neutrons. The second system, the SSTs, measures the angular trajectories and charge of the charged fragments.

2.2.2.A SSTs (Silicon Strip Detectors)

Surrounding the target (figure 2.8) eight double-sided Silicon Strip Detectors (SSTs) [76] were positioned to measure the trajectories and energy loss of the charged particles impinging on and emerging from the target. Two of them denoted as (SST1 and SST2) are positioned before the target in the beam line. Other two denoted as (SST3 and SST4) are positioned after the target also in the beam line. The other four SSTs detectors were placed around the beam line, forming the four parallel sides of a rectangular Box, to detect knocked out and scattered protons and light hadrons. In this experiment these detectors were not working properly. As a consequence, the silicon detectors placed at the Box were not considered for the analysis of the data presented in this thesis.

The two SSTs before the target were used to measure the trajectory of the incom-

ing beam and consequently the entrance angle of the beam, as well as to characterize the atomic charge of the nuclei. The two SSTs after the target were used to measure the trajectory and angle of the particles emerging from the target and also for charge identification of the reaction fragments.

Each of the detectors is a double sided silicon strip detectors with 72 mm x 40 mm in size and 0.3 mm thickness. One of the sides (S Side) has 640 strips with a readout pitch of 110 μm and measures in the horizontal direction. The other side (K Side) has 384 strips with a pitch of 105 μm and measures in the vertical direction. Figure 2.9 shows a image of one Silicon Strip Detector with its front end readout card.

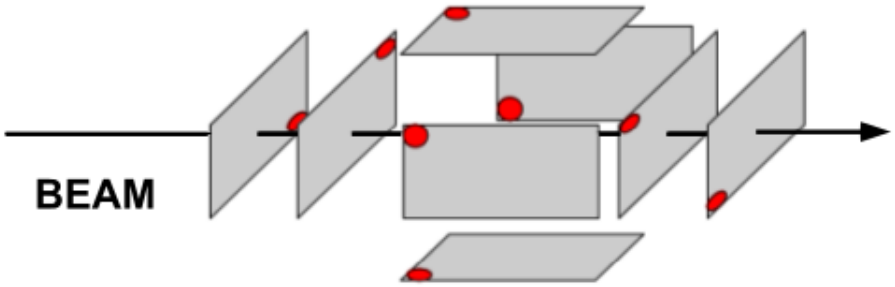

Figure 2.8: Silicon Strip Detectors configuration.

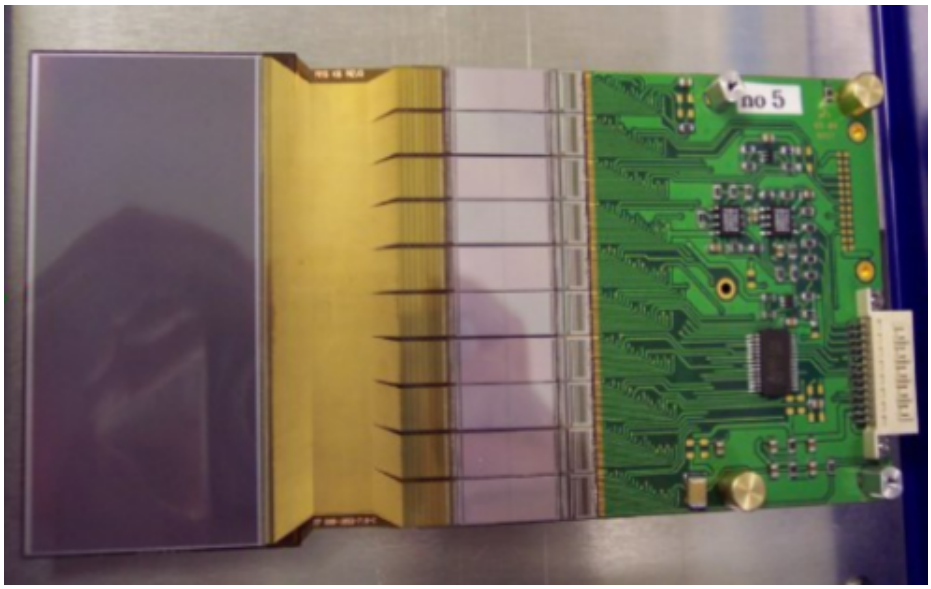

Figure 2.9: Picture of one Silicon Strip Detector with their front end readout card.

2.2.2.B Crystal Ball

The Crystal Ball [81,82] is a 4π calorimeter used to measure the de-excitation of the nuclei by γ rays and to detect the protons and neutrons in the exit channel of the reactions. The detector system is composed by 159 NaI(Tl) crystals where each one covers a approximated solid angle of 77 msr. The two open hemispheres of the Crystal Ball with the scattering chamber in the center are shown figure 2.10.

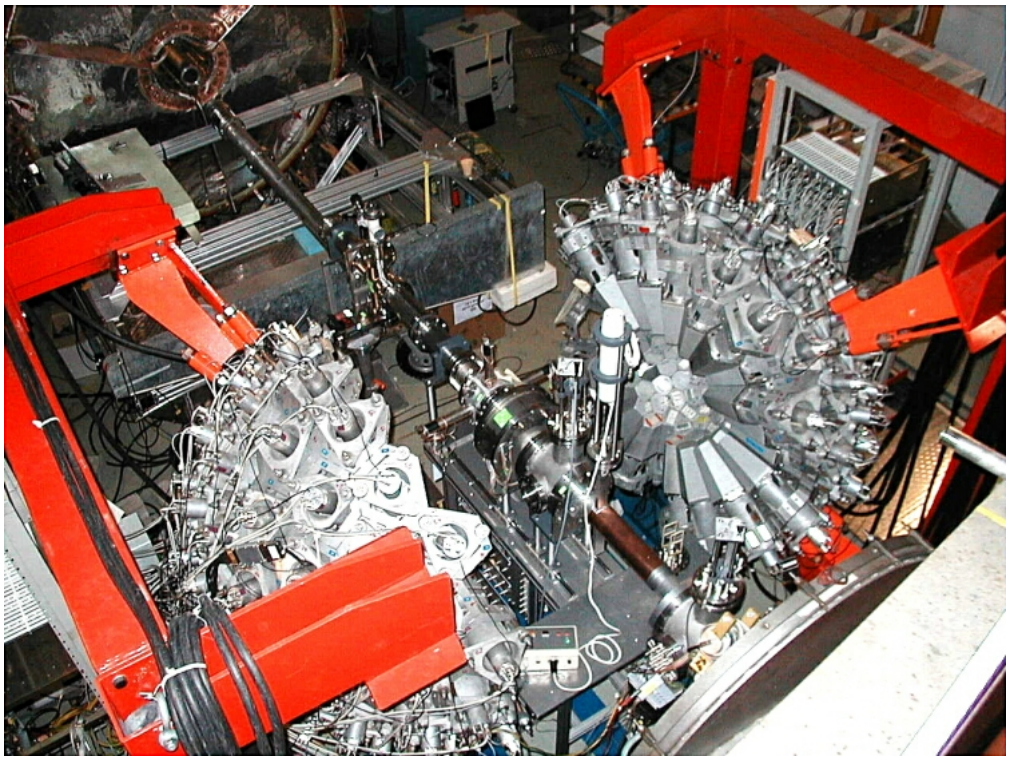

Figure 2.10: Picture of open two hemispheres of Crystal Ball array.

The energy deposited by the protons and neutrons in the crystals is about two orders of magnitude higher than that of the photons. In order to allow the measurement of all particles, the signal of half of all photomultipliers (forward direction) was divided into two electronic chains characterized by different gains.

2.2.3 Detector systems after the target

Because of the relativistic energies the fragments have in this experiment, all particles are emitted in the forward direction. The magnet dipole ALADIN, with an angular acceptance of ±60 mrad, is positioned after the target area. As a result of the Lorentz force, it deflects the trajectory of charged particles travelling with velocity (β) inside magnetic field (B). This results in the separation of the reaction products in three branches (figure 2.4) according with their magnetic rigidity.

- Neutron Branch: As neutrons do not feel the magnetic field of ALADIN, they are not deflected by the magnetic dipole and follow a straight line in the forward direction. The LAND measures the Time-of-flight and the position of

forward direction neutrons for their momentum characterization.

- Heavy Ion Branch: Heavy ions always have A/Z > 1, following a different trajectory path than protons. The trajectories of the reaction fragments are detected by two fiber detectors (GFIs) and their position and energy loss is measured by a plastic scintillator detection system.

- Proton Branch: Protons, with a particular magnetic A/Z ratio of 1, follow distinct trajectories compared to the heavy ions. Forward direction protons trajectories are detected by two drift chambers (PDCs) and at the end of the line there is a plastic scintillator system detector, the so-called DTF used for position and energy loss measurements.

For the analysis of the neutron knock-out reaction ^{15}C(p,pn)^{14}C we only concentrated on the Heavy Ion Branch, that will be described in more detail below. A detailed description of the detection systems LAND, PDCs and DTF can be found in references [60, 80, 83–85].

2.2.3.A GFIs

The GFIs [86] are two large area scintillating fibre detectors used for the measurement of trajectories of charged reaction fragments with $A/Z > 1$ after their deflection by the ALADIN dipole magnet. A schematic view of the detector is shown on the left side of figure 2.11.

Each detector contains approximately 480 parallel scintillating fibres with a cross-section of 1mm^2 and an active area of 50x50 cm^2. It measures the horizontal position of the ions hitting the detector. Each fibre is connected on one side to a regular photomultiplier (PM) for time measurements and trigger purposes and on the other side to a Position Sensitive Photomultiplier (PSPM) with 64x59 mm^2 [86] used for position measurements, shown on the right side of figure 2.11. At the PSPM side the fibers are placed into a mask ordered in a 25 x 20 matrix, which is coupled onto the PSPM.

The PSPM anode consists of a rectangular grid of 18 wires in one direction (u) and 16 wires in the orthogonal direction (v) with a distance of approximately 3.7 mm between the anode wires [86]. With this configuration it is possible to reconstruct the signal for all individual fibres with a smaller number of electronic channels.

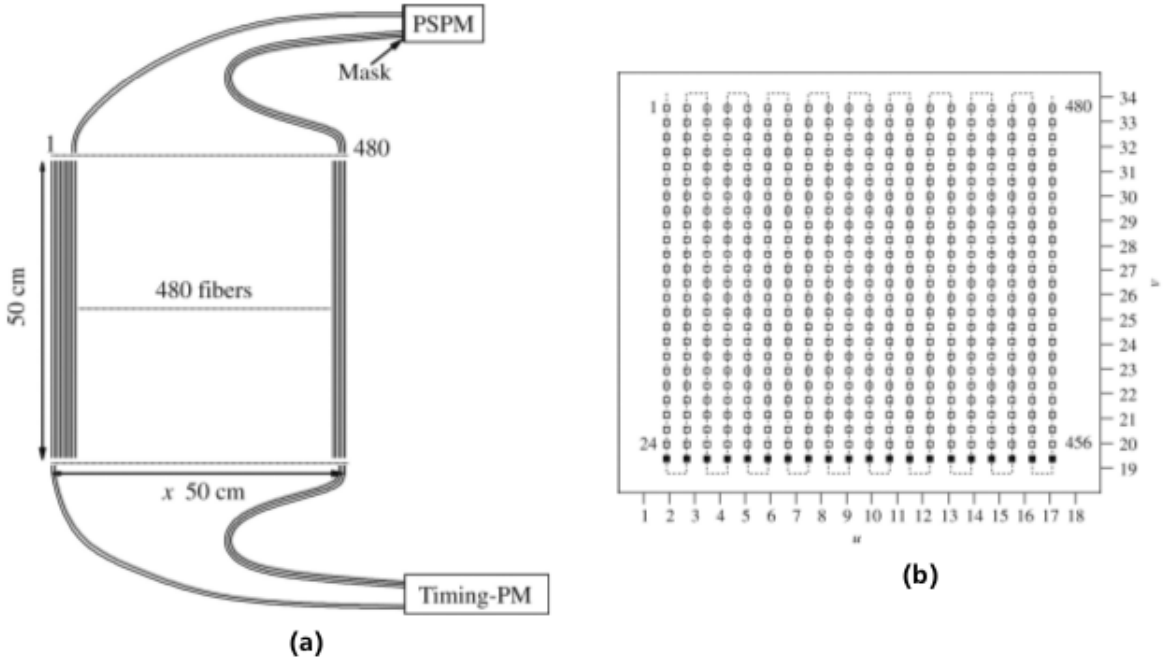

Figure 2.11: Schematic view of one GFI detector (a) and the mask (b) used to connect the fibers to its position-sensitive photomultiplier.

2.2.3.B TFW

The Time-of-Flight Wall (TFW) [80] is a 1.8 × 1.4 m^2 detection system used to measure the position, energy-loss and time signals of heavy ions emerging from the ALADIN magnet. It consists of two planes of 18 vertical and 14 horizontal plastic scintillator paddles, each 5 mm thick and 10 cm wide with two photomultipliers (PM) at the two short ends (figure 2.12). Based on the assumption of uniform light propagation in the paddle and given the times and amplitudes of the light measured at both ends, we can reconstruct the time, the energy loss and the position calculated from the time difference or from the energy logarithm of the difference.

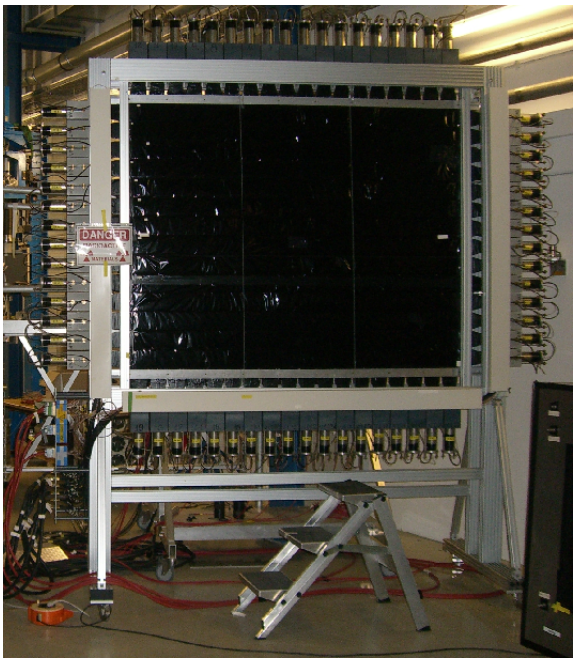

Figure 2.12: It is shown the picture of TFW in cave C during the S393 experiment.

2.3 Data acquisition system

During the S393 experiment data was collected by several detectors systems and stored on an event-by-event basis using the Multi-Branch System (MBS) [87] developed at GSI. The Data AcQuisition (DAQ) converts the time and energy electrical analogue signals coming from the detectors systems into digital values which are clustered in events and stored in list-mode data files (LMDs) by the Event Builder. More information on the DAQ can be obtained on [80, 87].

2.3.1 Triggers and DownScale factors

As the experimental setup has several detector systems, the overall dead time of the data acquisition system is an important issue [87]. In order to reduce this to the minimum it is necessary to apply a reduction factor to the number of accepted triggers by the DAQ. More detail on this can be found on [62].

By selecting and combining signals from different detectors it is possible to create a Trigger Pattern (TPAT) associated with a certain kind of reaction. Depending on its frequency, some of the trigger patterns are scaled down in order to reduce the

dead time and enable the data-acquisition system to process the events more effectively. Table 2.1 shows the trigger combinations forming different trigger patterns (first column). The second column of the table gives a short description about the physical meaning of each trigger. The next eight columns are showing, whether a detector was required (1) or used as a veto (0) for a certain trigger pattern. The final column provides the downscale factor for setting 3 of the FRS, where the ^{15}C was produced.

Table 2.1: TPATs table including the DownScale (DS) factors for setting 3 used on the present work. The TPAT of interest (2) and (8) considered in this analysis, marked with bold characters have a DS factor of 64 and 1 respectively.

TPAT	Name	POS	ROLU	S8	TFW	XB	DTF	PIXEL	LAND	DS factor
1	Good Beam	1	0							128
2	**Fragment**	**1**	**0**		**1**					**64**
4	S8			1						2048
8	**XB Sum**	**1**	**0**		**1**	**1**				**1**
16	Proton	1	0		1		1			1
32	Pilup	1	0							128
64	Pixel		0					1		1
128	Neutron	1	0		1				1	1

For the calculation of the ^{15}C(p,X)^{14}C inclusive cross section (explained on section5.2) without requiring any signal at Crystal Ball, the used trigger was TPAT=2, the so-called “Fragment” trigger pattern. With this trigger pattern, a absent signal in ROLU detector, a signal in the POS detector to guarantee a ”Good Beam” event, and a signal in the TFW were requested. As the Downscale factor for this TPAT is 64, only 1 event in 64 is stored. This fact will have a strong impact when analysing one of the reaction channels of interest for this work.

3

Detector Calibrations and Data Reconstruction

Contents

This chapter contains a brief description of the employed procedures to calibrate some detector systems and to obtain meaningful observables from the S393 experimental campaign. The analysis framework *land02* [87] used for calibrations and reconstruction processes will be also introduced. A special focus will be given to the TFW, GFIs, Silicon Strip Tracker (SST) and Crystal Ball detector systems. Finally the methods and procedures that have been used to identify the incoming beam particles and the tracker system used to deduce the mass of the particles travelling through the ALADIN magnet based on their trajectories will be explained.

3.1 Calibration and data reconstruction using the *land02* package

In order to obtain physical quantities like time in ns, energy in MeV and positions in cm, the collected data by the several detectors of the setup and stored by the DAQ in the *lmd* format files should be converted to a more friendly analysis format and data must be calibrated. These procedures were done using the software package *land02* originally written by H. Johansson [87, 88] for the R^{3}B-Land collaboration at GSI. This package consists of several individual script routines, which allows the extraction of some calibration parameters and other script routines that convert the lmd files into root [89] files and allows different levels of calibration.

3.1.1 Calibration *land02* routines

The *land02* package includes several script routines which are used in some parts of the calibration process.

- clock: is used to determine the pedestal values (section 3.1.3). These parameters are used later in the lmd conversion process.
- tcal: is use to determine the offset and slope parameters of time calibration.
- phase1: is used to match the gain of all photomultipliers of a time-of-flight wall.

- lt-range: This script function allows the introduction of different calibration parameters for different ranges of the data set when the detectors information suffers variations along the time.

3.1.2 Data analysis levels

In the process of converting lmd files into root files several calibration steps are associated to different data analysis levels.

- RAW: In this level the binary format (lmd files) is converted to a friendly analysis format (ROOT files) without additional data treatment. The information given in Time to Digital Converter (TDC), Charge to Digital Converter (QDC) or Analog to Digital Converter (ADC) channels is organized by detector.
- TCAL: In this level TDC channels are converted to time units (ns) and the QDC pedestal is subtracted.
- SYNC: Many detector systems are composed by several individual detectors. This level allows the reconstruction and synchronization of the data for the whole detector system as one.
- DHIT: The interaction of the particle with the detector (hit) is characterized in this level by the energy loss, time information and position in the detector specific coordinates.
- HIT: The hit information is now in laboratory coordinates. Positions are given in cm, times in ns and energies in MeV.
- TRACK: This level allows the identification of the different isotopes by the reconstruction of their mass, atomic number and velocity.

The following two sections introduce the general ideas and concepts of time calibration *i.e.* the conversion of TDC channels to ns and the identification and removal of QDCs pedestal. These calibrations allow to obtain parameters which are applied to the TCAL level in *land02*.

3.1.3 Pedestal subtraction

The QDCs converts charge into digital values, by measuring the voltage into an internal capacitor. All detector channels read out by a QDC contain a small charge in the QDC capacitor even when no event has occurred, resulting in a non zero conversion value. This is known as the pedestal and has to be determined and subtracted from the measured values in order to obtain the correct energy data. The pedestal can be obtained by digitizing the noise with a trigger generated during the experiment by a clock signal that works in the absence of any external signal. Using the *Clock* routine, that selects data from those clock triggers, we can determine the pedestal and apply the obtained parameters on the TCAL calibration level [87].

As an example figure 3.1 shows the effect of pedestal subtraction. On the left the raw energy read out signal by a TFW photomultiplier. On the right is shown the same read out signal after the pedestal determination and subtraction.

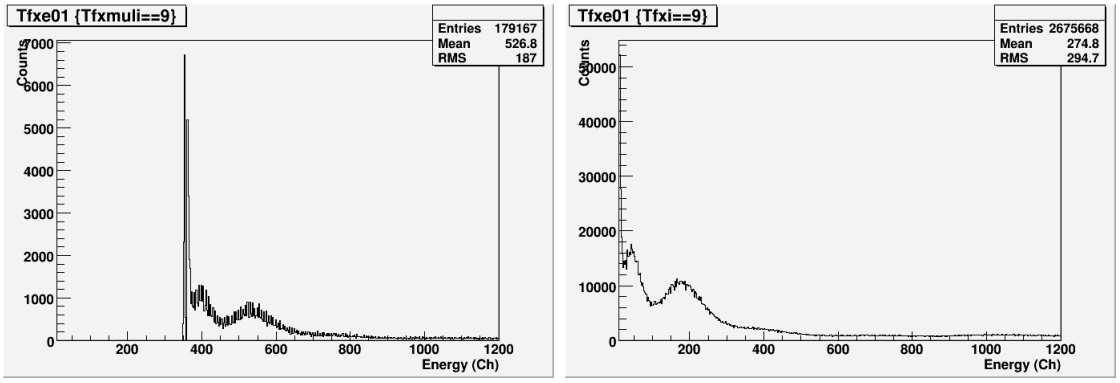

Figure 3.1: The energy spectra for TFW, PM1 of paddle 9 on the RAW level (left). The pedestal was determined by fitting a Gaussian and obtaining its mean values which are subtracted from the energy spectra on the TCAL calibration level (right).

In order to determine the pedestal calibration parameters, the pedestal variation and stability along the whole experiment was studied.

3.1.4 Time calibration

During the experiment the time information from several detectors relatively to the time of a reference detector was used. For an accurate time measurement in

nanoseconds and a good time resolution the time calibration is essential.

The time branch detector channels were read out by TDCs for which the nominal gain value may have slightly fluctuations during the experiment. These can be caused by several factors as changes in the temperature of the module or power fluctuations. In order to transform the time signals in time units (ns) and correct this effect, a "time calibrator" (TCAL) which creates signals with discrete known times at regular frequency was running during the whole experiment. By comparing the measured signals in channels with this clock signals, we can obtain an accurate conversion of the measured channel signals in ns [85,90]. This procedure is necessary to all detectors which are collecting time information and in addition synchronization between detectors should be performed.

The calibration parameters (gain and offset), determined considering a linear correlation of TCAL signals and the obtained channel values of the TDC readout were extracted using the *tcal* routine. The stability of these parameters was studied throughout the whole experiment in order to use correct calibration parameters in *land02*.

3.2 Detectors system calibration

In this section the detection systems calibrations performed by the author will be explained. The goal of this process is to ensure that each measured event can be translated in one hit with the right energy value, time and position relatively to detectors structure and lab coordinates. Special focus will be given to the TFW, GFI, SSTs, Crystal Ball detectors, as well as to the *tracker* algorithm.

3.2.1 TFW calibration

The TFW detector system (subsection 2.2.3.B) is made of several plastic scintillating paddles with two PM-tubes at the extremities. When a charged particle crosses a paddle it will deposit some of its energy which is dependent on its charge and consequently generates a scintillating light which will travel along the paddle

to the photomultipliers. Based on the assumption of uniform light propagation in the paddle and given the times and amplitudes of the light measured at both ends by the two PM-tubes, it is possible to reconstruct the time (T), the energy loss (E) and the position (P) of the hit [87].

Figure 3.2 shows the schematic view of a hit in the paddle. The light created by the hit scintillation reaches the two PM-tubes at the edges of the paddle. In each photomultiplier it is measured an energy and a time.

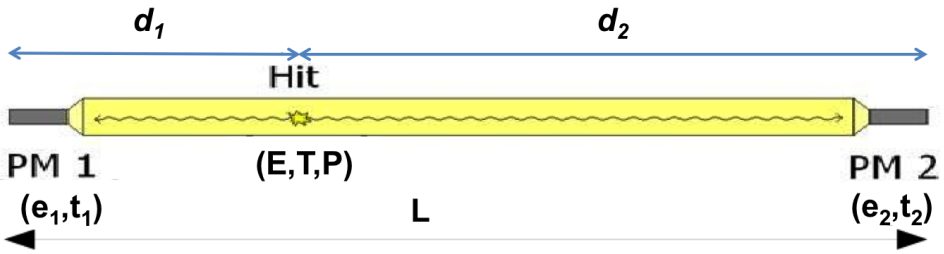

Figure 3.2: Schematic view of one TFW Paddle. The energy E, the time T and the position of the hit in the paddle P can be reconstructed by the time and energy signals measured by each photomultipliers *PM1* and *PM2*, where L is the length of the paddle.

3.2.1.A Reconstructing the time, position and energy loss

With the effective speed of light in the scintillator, ν (usually about 0.5c – 0.6c), the two times measured at the ends of the paddle will be:

$$t_1 = T + \frac{1}{\nu} d_1 \tag{3.1}$$

$$t_2 = T + \frac{1}{\nu} d_2 \tag{3.2}$$

Where d_1 is the distance from $PM1$ until the hit and d_2 the distance from the hit until $PM2$. From this, we solve for the time (T) of the hit as an average

$$T = \frac{t_1 + t_2}{2} - \frac{d_1 + d_2}{2\nu} = \frac{t_1 + t_2}{2} - \frac{L}{2\nu} \tag{3.3}$$

The constant length of the paddle, $L = d_1 + d_2$, divided by the effective speed of

light, may be fused into the overall time calibration parameters, i.e. just a shift of the time offset for the paddle, leaving us with the more convenient:

$$T = \frac{t_1 + t_2}{2} \tag{3.4}$$

The position (P) is calculated as the difference of the two times, and the paddle length disappears also here from the final formula

$$P = \frac{(d_2 - L/2) + (L/2 - d_1)}{2} = \frac{d_2 - d_1}{2} = \frac{\nu(t_1 - T) - \nu(t_2 - T)}{2} = \nu\frac{t_1 - t_2}{2} \tag{3.5}$$

With the light attenuation length in a paddle λ (for TFW about 1.6 m), the two energies are:

$$e_1 = Eexp(\frac{-d_1}{\lambda}) \tag{3.6}$$

$$e_2 = Eexp(\frac{-d_2}{\lambda}) \tag{3.7}$$

solving, the energy is given by:

$$E = \sqrt{e_1 e_2 exp(\frac{d_1}{\lambda} + \frac{d_2}{\lambda})} = exp\frac{L}{2\lambda}.\sqrt{e_1 e_2} \tag{3.8}$$

and the position achieved by the energy signal is:

$$P = \frac{d_2 - d_1}{2} = \frac{\lambda.ln\frac{E}{e_2} - \lambda.ln\frac{E}{e_1}}{2} = \lambda\frac{lne_1 - lne_2}{2} \tag{3.9}$$

Once again, a constant factor,$e^{\frac{L}{2\lambda}}$, may be omitted and this time considered part of the energy gain calibration parameters, giving [87]:

$$E = \sqrt{e_1 e_2} \tag{3.10}$$

In order to extract these physical quantities (E,P,T) the whole detector needs to be calibrated, matched and synchronized. This process consists of several steps.

The output of each photomultiplier feeds a TDC and QDC which are responsible respectively for the time and energy measurements. First of all, in the calibration

process, the pedestal of the QDCs should be removed (section 3.1.3) and the TDCs signals should be converted from channels to *ns* (section 3.1.4). Following, the gain of the two photomultipliers in one paddle should be matched and their times should be synchronized. As this detector system has crossed paddles, we can consider, the hits in the center of the paddle gives a time difference of zero in the two photomultipliers of the paddle and the same for the energy signals. Finally, by using a big amount of data to assure that every crossed pair of paddles is hit at least once it is possible to correct the time shifts and the difference of energy gains for each paddle with respect to the others [7,85]. These gain match and synchronization parameters were obtained by the *phase1* routine and this procedure is much similar to the used for the calibration of the LAND detector and partially for the DTF detector [60].

Figure 3.3 shows the energy loss versus the paddle for the first plane of TFW, before and after the gain match. As the reconstructed energy in the TFW is used to charge determination of the reaction fragments, a good resolution which is directly dependent of the synchronization is important.

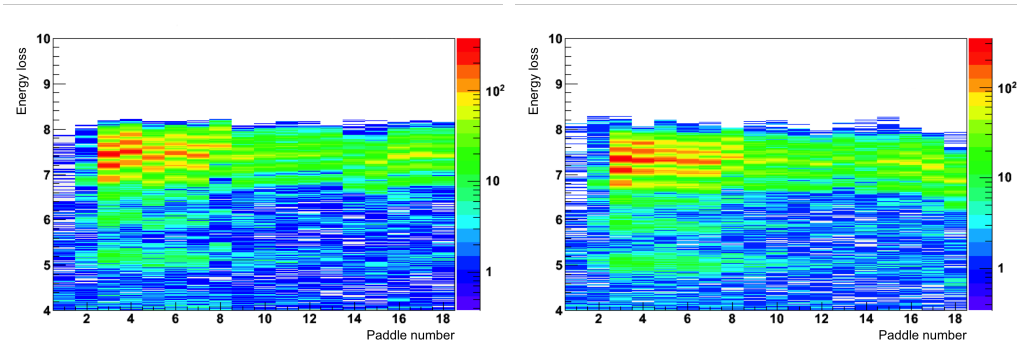

Figure 3.3: Energy loss versus paddle number in the first plane of TFW. In the left before calibration and in the right after the calibration. After matching the energy gain for all paddles the energy resolution is improved.

The dependence of the time on the position before and after time calibration is shown in figure 3.4. In the right, after calibration there is a significant improvement of time resolution.

The energy loss as a function of x position for the first plane of TFW is shown in figure 3.5. In the left panel the complete calibration is not applied yet. After the calibration a large improvement in the resolution of the extracted energy and posi-

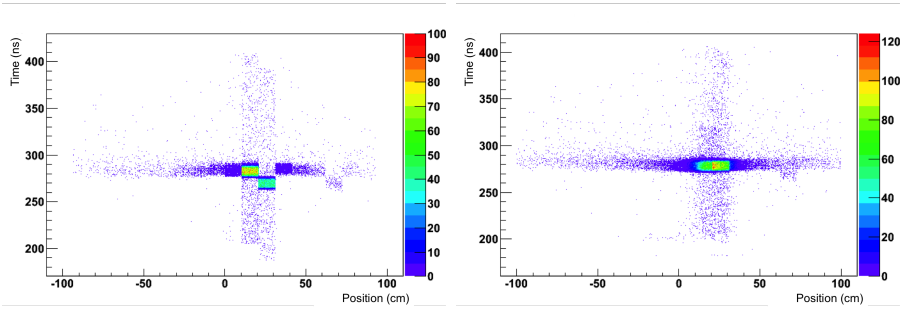

Figure 3.4: Time versus x position in the TFW. The left panel presents the results obtained before performing the calibration of the detector and the right panel presents a much improved result after calibration has been performed.

tion is observed. The different clusters shown in the figure represent the different charges (Z) of the isotopes reaching the TFW.

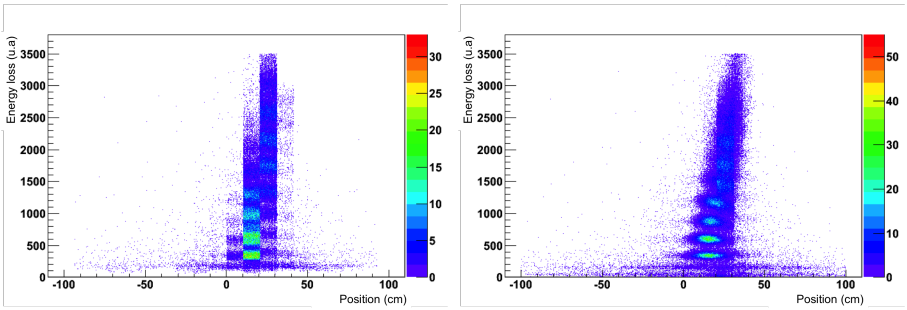

Figure 3.5: Energy loss in the first plane of TFW versus the position. On the left panel before the calibration and after the calibration on the right.

More information on the TFW calibration can be in [7, 61, 85].

3.2.2 GFI calibration

The GFI's (section 2.2.3.A) are two large area scintillating fibre detectors used for the measurement of trajectories of charged reaction fragments after their deflection by the ALADIN dipole magnet. A schematic view of the detector is shown on the left side of figure 3.6. Each detector contains approximately 480 parallel scintillating fibres with a cross-section of 1mm^2 and an active area of 50x50 cm^2 and it measures the horizontal position of the ions hitting the detector.

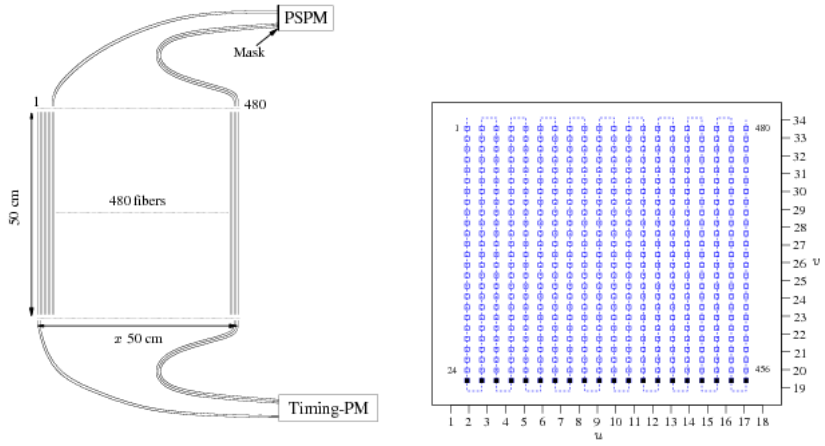

Figure 3.6: Schematic view of the scintillating fibre detector is shown on the left. On the right the mask where the fibres are coupled is shown.

Each fibre is connected on one side to a regular photomultiplier for time measurements and trigger purposes and on the other side to a Position Sensitive Photomultiplier (PSPM) with 64x59 mm^2 [86] used for position measurements. At this side the fibers are placed into a mask ordered in a 25 x 20 matrix, which is coupled onto the PSPM, shown on figure 3.6.

The PSPM anode consists of a rectangular grid of 18 wires in one direction (u) and 16 wires in the orthogonal direction (v) with a distance of approximately 3.7 mm between the anode wires [86]. With this configuration it is possible to reconstruct the signal for all individual fibres with a smaller number of electronic channels.

The calibration procedure consists of several steps. First, the QDC pedestal must be removed. After this, the gain of the PSPM wires must be matched and finally a correlation between the position of the fibres and the signals in the PSPM is performed.

A hit on scintillating fibre creates a signal in several neighboring wires of the PSPM in the two orthogonal directions. The hit position is given by the centroid of the signals in the wires. As the gain of the PSPM is position dependent the gain of all PSPM channels should be matched.

In figure 3.7 the energy in the anode wires with direction (u) versus the or-

thogonal direction (v) is shown for both GFI's. After applying the gain matching procedure three times, the distribution of clusters in the PSPM is closer to the distribution of fibres in the mask, representing a better calibration.

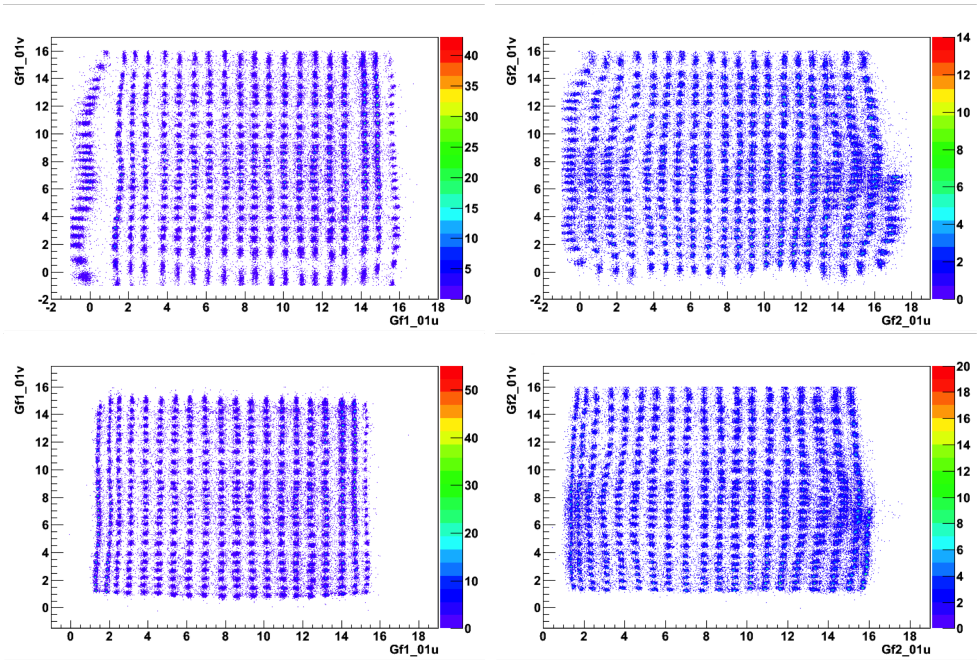

Figure 3.7: Signal in the PSPM of GFI 1 on the left column and in GFI 2 on the right column. Top row before the gain match and bottom after gain match.

After matching the gain, the position of the clusters, the widths and the relative position to the neighbors is determined by the so-called "indexing" aiming at reconstructing the x position of the hit in the detector.

$$x = \frac{\sum w_{kl} x_{kl}}{\sum w_{kl}}$$

Where x_{kl} is the position of the corresponding fibre in the detector and w_{kl} is the probability of the hit to belong to the (k,l) grid point, obtained by:

$$w_{kl} = \frac{1}{\sqrt{\sigma_{ukl}\sigma_{vkl}}} exp[-\frac{(u_0 - \bar{u}_{kl})^2}{\sigma_{ukl}^2} - \frac{(v_0 - \bar{v}_{kl})^2}{\sigma_{vkl}^2}] + \frac{g}{\sigma_0} exp[-\frac{(u_0 - \bar{u}_{kl})^2}{\sigma_0^2} - \frac{(v_0 - \bar{v}_{kl})^2}{\sigma_0^2}]$$

Where $(\bar{u}_{kl}, \bar{v}_{kl})$ and σ_{ukl} and σ_{vkl} are the position and standard deviations of the cluster corresponding to the grid point (k,l). Some hits are reconstructed somewhere in-between two grid points, however individual clusters cannot be seen using such events. In order to correct this effect, the parameter σ_0 is introduced as the width of the meanders visible in the mask structure [86].

To verify the quality of the calibration, the position in GFI 1 versus the position in GFI 2 is shown in figure 3.8. The right image corresponds to a better calibration.

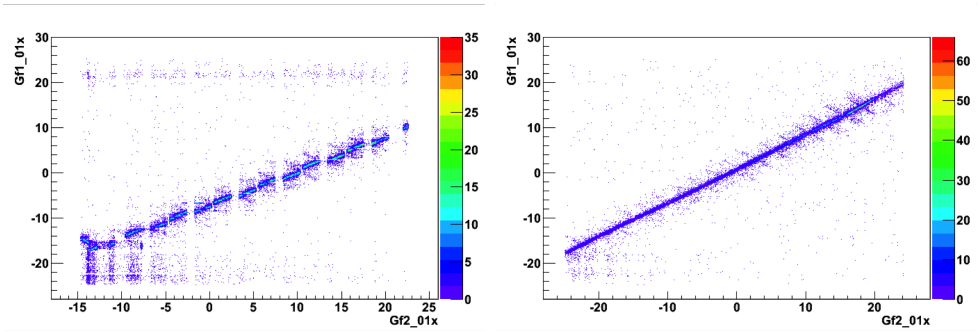

Figure 3.8: GFI 1 versus GFI 2 for two different calibrations. The plot on the right represents a better calibration.

More detailed information on the GFIs calibration procedure can be found in [7, 61, 91].

3.2.3 SSTs calibration

The reaction target is surrounded by eight SSTs (section 2.2.2.A) which measures the position (trajectory) and energy loss of the particles impinging and emerging from the target. Four of them are placed around the beam line (referred as Box) and the other four are placed in the beam line, two before the target and two after the target. As the four Box detectors positioned around the beam line were not working properly they were not used for the analysis of the data presented on this thesis and the described calibration was applied just for the in line SSTs.

When a charged particle (proton or fragment) crosses the detector, generates a signal in several neighbouring strips (cluster) with a Gaussian distribution of charge signals. The position of the hit is determined by the charge weighted center of grav-

ity and the energy deposited by the charged particle is proportional to the cluster charge integral. The calibration of this system consists of several steps. First the pedestals were measured and subtracted (section 3.1.3).Than, the strips which were not working properly and were not collecting data should be identified and marked as "dead strips". In general their signal value can be estimated using the values of two neighbouring strips. This is important in order to determinate a good center of gravity and consequently a good hit position. As the total charge of the hit depends on the position where the charged particle hits the strip, the energy signals and reconstructed positions sharing two strips should be corrected. In addition, in order to increase the position and energy lost resolution of the detectors the gain for the different channels should be matched.

The two SSTs before the target were used to measure the trajectory of the incoming beam and consequently the entrance angle of the beam. The two SSTs after the target were used to measure the trajectory and angle of the particles emerging from the target and also for charge identification of the reaction fragments.

In order to take the correct angles the four SSTs should be aligned. Using a script the position of the two entrance SSTs and of the two exit SSTs was estimated. The difference from the real positions to the estimated positions (residuals) were used to align the SSTs. To improve the alignment the same process was repeated, fixing three SSTs. In the Figure 3.9 is shown the angle distribution in the horizontal direction for the incoming (left) and outgoing (right). After the alignment both are centred on zero presenting a mean value of 0.026 mrad and 0.125 mrad with a sigma of 2.03 mrad and 2.08 mrad respectively. For the vertical direction the same behaviour was observed.

More detailed information on the SSTs calibration procedure can be found in [62, 76, 92, 93].

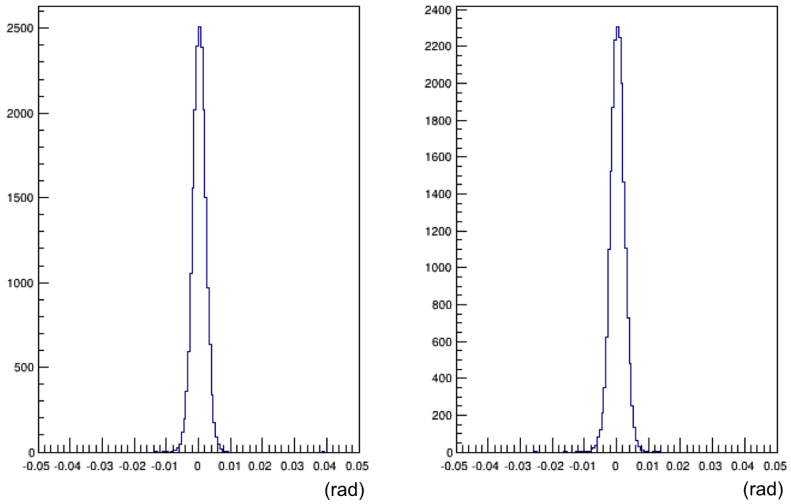

Figure 3.9: Distribution of angles for the X direction. On the left for the entrance angle and on the left for the emerging angles.

3.2.4 Crystal Ball calibration

The Crystal Ball (section 2.2.2.B) is a 4π calorimeter used to measure γ-rays emitted from fragments de-excitation with expected energies from near 0 MeV untill 2 MeV and to detect in the forward hemisphere of the detector high-energy protons and neutrons, which the energies can reach few hundreds of MeV.

In the energy branch calibration, the QDC offsets (pedestals) and gains (slopes) of each individual crystal had to be determined in order to convert QDC channels into MeV, however different procedures have been employed to γ-rays readout and high energy readout (protons and neutrons branch).

The radioactive calibration sources, ^{22}Na with the 511 keV and 1274.54 keV energy peaks [3], and ^{60}Co with 1173.23 keV and 1332.49 keV energy peaks were used to the γ-rays readout calibration. Those fitted peaks in channels were plotted against the known energy values in MeV and by a linear fit through these points, the offset and (slope)gain were determined for each individual crystal and applied as a calibration parameter.

Using the positions of those four photo peaks, a linear-regression fit was per-

formed in order to determine the calibration parameters of the linear energy-versus-channel relation.

$$E(MeV) = gainX(E(channels) - offset) \tag{3.11}$$

Figure 3.10 shows the energy spectrum in the crystal 51 for a ^{22}Na in a background run after the calibration of the gamma readout. The two energy peaks of 511 keV and 1274.54 keV are already adjusted.

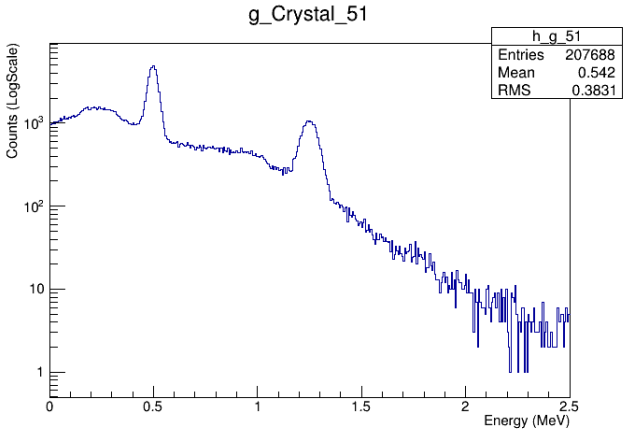

Figure 3.10: The γ-rays spectra for ^{22}Na calibration run, measured by crystal number 51. It is observable the 511 keV and 1274.54 keV energy peaks.

As the proton and neutron energies measured are much larger than the measured for photons, the obtained γ-rays readout calibration works as a starting point however it is not reliable for energies beyond a few tens of MeV since small deviations can lead to big fluctuations at those energies.

Ideally, this branch calibration should be done with proton beams with different known energies in the range from tens to hundreds MeV and different angles covering the whole forward hemisphere of the Crystal Ball however, this it was not possible in the experimental campaign. Alternatively, cosmic ray muons were used for this purpose.

Those are minimum ionizing particles and their different paths through the detector lead to a continuous energy loss spectrum.

We considered only single cosmic muons which crossed two opposite crystals with respect to the centre of Crystal Ball and the ones which crossing through several crystals do not enter into the scattering chamber at the center of Crystal Ball. Their travelled trajectories through the detector can be assumed and based on the Geant3 simulations the deposited energy (loss) in the crystals was estimated and consequently used to synchronise the crystals [24, 94].

More detailed information on the Crystal Ball calibration, on the used algorithms to the selection of cosmic muons and simulations can be found in reference [24, 61, 67, 94].

3.2.4.A Addback

When a γ or particle impinges into a detector crystal, regularly the hit energy is distributed over an area of neighbours crystals (cluster). In order to reconstruct the (entire) energy of each (hit) γ or particle, an addback algorithm is used. For each event the algorithm sorts each crystal energy signal into a list. It starts with the highest deposited energy and determines whether the corresponding particle (hit) was a photon or a proton/neutron. If the crystal has a finite energy in the γ-branch, the cluster will be assigned to a photon, otherwise, if the γ-energy is a overflow, and the proton-branch energy is finite, it will be assigned to a proton. Then the energy of each crystal neighbouring is added.

At this analysis it is not possible to distinguish between protons and neutrons, furthermore the detection efficiency for neutrons is low.

3.3 Identification of incoming beam particles

In order to identify the incoming ions arriving to cave C from the FRS, the ratio between the mass number and the charge number (A/Z) was determined by means of the time-of-flight between two detectors in the experimental setup. The charge number was inferred by the energy loss in a third detector, so-called (PSP) (section 2.2.1.C).

Measurements of the time-of-flight required the use of two plastic scintillators: the so-called (S8), placed at the FRS and the (POS) detector (section 2.2.1.A), placed at the entrance of cave C. The distance between them was about 55 m, allowing for accurate time measurements. By determining the velocity of the ions β=v/c and knowing the magnetic rigidity (Bρ) from the FRS setting it is possible to infer the A/Z ratio, considering:

$$B\rho \propto \frac{A}{Z}\beta\gamma \tag{3.12}$$

Where γ is the Lorentz factor and (ρ) is the curvature radius of the trajectory.

For the charge measurement a position-sensitive pin diode (PSP) with (4.5 x 4.5) cm^2 active area and a thickness of 300 μm was used. By using the Bethe-Bloch formula [95], it is possible to understand the dependence of the deposited energy per unit length in the detector by a ion with charge number (Z):

$$-\frac{dE}{dx} = \frac{4\pi Z^2}{m_e c^2 \beta^2}\frac{N_a z \rho}{M_u}\left(\frac{e^2}{4\pi\epsilon_0}\right)^2\left[ln\frac{2m_e c^2\beta^2}{I} - ln(1-\beta^2) - \beta^2\right] \tag{3.13}$$

Where m_e the electron rest mass, e the electron charge, c the speed of light, N_a the Avogadro's number, ϵ_0 the vacuum permitivity and I, z, A, M_u and ρ are mean excitation potential, the atomic number, the mass number, the molar mass and the density of the target respectively.

By combining the charge number and the mass over charge ratio we can have a unambiguous identification of the incoming isotopes to the cave C. Figure 3.11 shows the identification plot for the incident ions coming from setting 3 of FRS, centered in A/Z=2.5. Isotope of interest ^{15}C, with Z=6 and A/Z=2.5, is identified inside the ellipse.

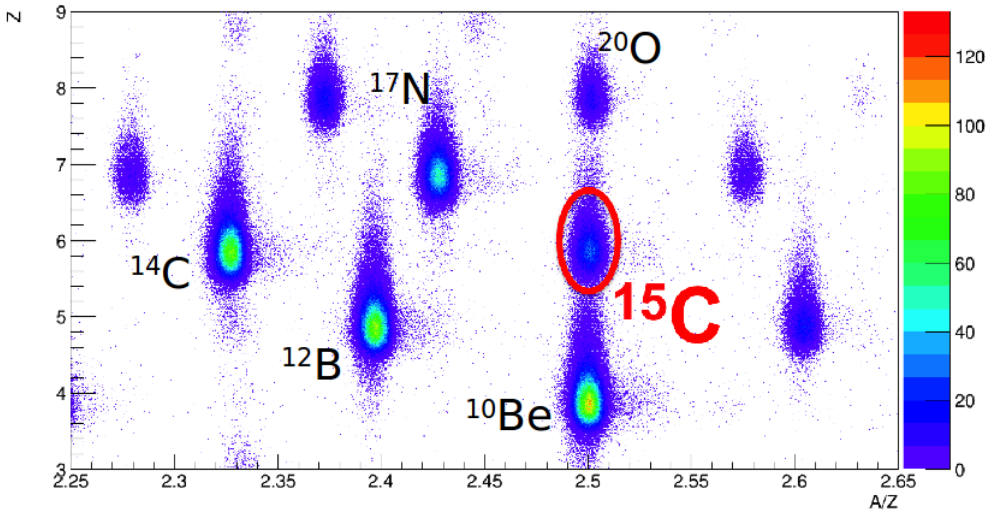

Figure 3.11: Incoming beam identification plot for the the experimental setting 3 of FRS considered in the present analysis. The atomic number of the nuclei is plotted against their mass over charge ratio.

3.4 Fragment charge identification

At this energies all arrived ions in cave C are completely stripped which means that their charge is the nuclear charge Z and their energy loss when crossing a material is given by the Bethe-Bloch (equation 3.13). In this work, fragments were identified by energy loss measurements in SST3, SST4 and TFW.

3.5 Fragment mass identification

An unambiguous determination of the reaction channel implies an accurate identification of incoming particles along with the reaction fragments. In addition, reconstructed masses of fragments and their time-of-flight measurements are mandatory for (reaction fragments) momentum distributions determination.

In order to reconstruct those masses, velocities and the momentum of fragments, the so-called *tracker* program [96] developed within the R^{3}B collaboration by Ralf Plag has been used. This program relies on the reconstruction of the trajectories of fragments from the reaction target, through the dipole magnet ALADIN until the

end of fragments branch.

Fragments will have different trajectories through the magnet depending on their mass, charge, beta, and on the ALADIN magnetic field. The programme uses the input of the charge of the fragment being tracked defined by means of the energy loss of the fragments in SST3 and SST4 and TFW, the positions of the ions measured with the SST3, SST4, the GFIs and the TFW. The evaluation of the magnetic field at ALADIN is performed using a set of field maps that have been measured for few electric currents running through the magnet. For different values, an interpolation in between the measured ones was done.

Based on these elements the masses of the fragments are calculated according to:

$$B\rho = \frac{A}{Z}\frac{m_u c}{e}\beta\gamma \tag{3.14}$$

Where m_u is the unit mass, c is the speed of light, e is the charge unit, Z and A are the charge and mass numbers of the particle, β and γ are the velocity and the Lorentz factor and (ρ) is the curvature radius of the trajectory.

Those inputs allows *tracker* to predict trajectories through the magnet, fragment masses and position residuals, which are defined as the reconstructed positions (in the detectors) minus the measured ones. In the calibration process the mass, the beta and positions in the detectors are slightly varied in order to reduce those residuals. The process is repeated iteratively. After the calibration these residuals should be near zero. Figure 3.12 shows the residual for the X position of GFI1. The mean value of the fit is 0.017 and the sigma 0.07. The same behaviour was observed for other residuals.

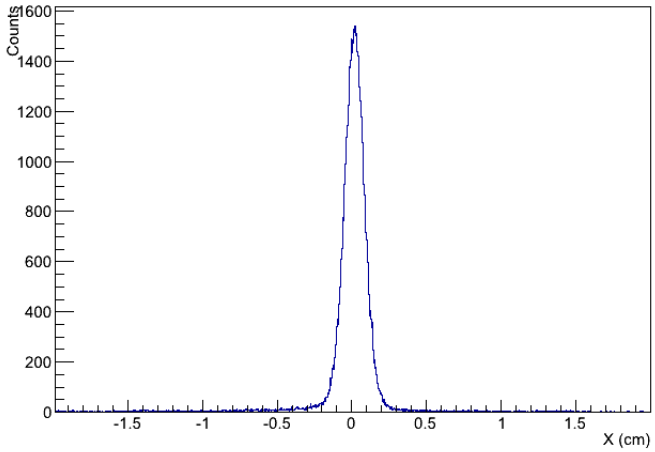

Figure 3.12: The residual for the X direction of GFI 2 is centered at 0.017.

The reconstructed positions are obtained from the fitted track. The programme optimises every track so that these residuals are minimum. Final adjustments and improvements to the mass resolution can be made by making small adjustments to the positions of detectors, or by varying the field slightly.

The Tracker programme allows to reconstruct various masses at once, however should be optimised for one specific mass. The peaks far from the optimised one tend do be not centred on the correct value. In the figure 3.13 is shown the reconstructed masses from A=9 until A=20. The tracker was optimized for A=15. Fitting the peaks for the masses 14 and 15 we obtained a centroid on 14.03 and 15.01 respectively and a resolution 1.42% and 1.37%.

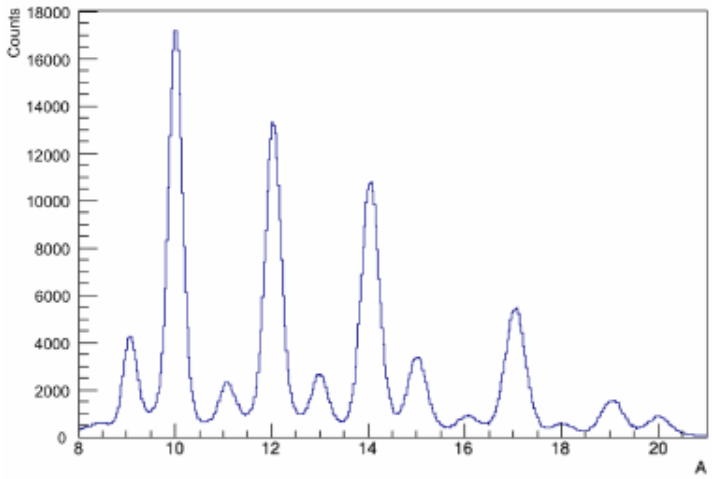

Figure 3.13: Fragment Masses identification from A=9 till A=20. Tracker allowed to separate the masses and centred near their unitary value.

4

Data Analysis

Contents

This chapter provides an overview of the most important methods and techniques employed for the data analysis. The first section explains the used procedures to an unambiguous identification of our reaction channel. Starting from the identification of the incoming projectiles and the outgoing fragments, the applied selection conditions are shown. In the following sections it will be introduced and explained how the physics observables, as momentum distributions, differential cross sections and the crucial background subtraction were obtained. The last part of the chapter is dedicated to proton-neutron correlations, to the explanation of the addback algorithm used with Crystal Ball and to the simulations performed in order to obtain the necessary Crystal Ball detection efficiencies.

4.1 Reaction channel selection

In this work the reaction of interest is the ^{15}C(p,pn)^{14}C at quasi-free scattering conditions. To an accurate selection of a reaction channel, incoming projectiles and outgoing fragments should be unambiguously identified. Furthermore light particles (protons an neutrons) and γ emerging from the reaction should be detected. Figure 4.1 shows on the top the characterization of incoming projectiles. In red it is shown the elliptical cut applied which allow the selections of isotope (^{15}C). On the bottom it is plotted the fragment mass after the target versus the energy loss. It is possible to identify various isotopes with different masses and atomic numbers.

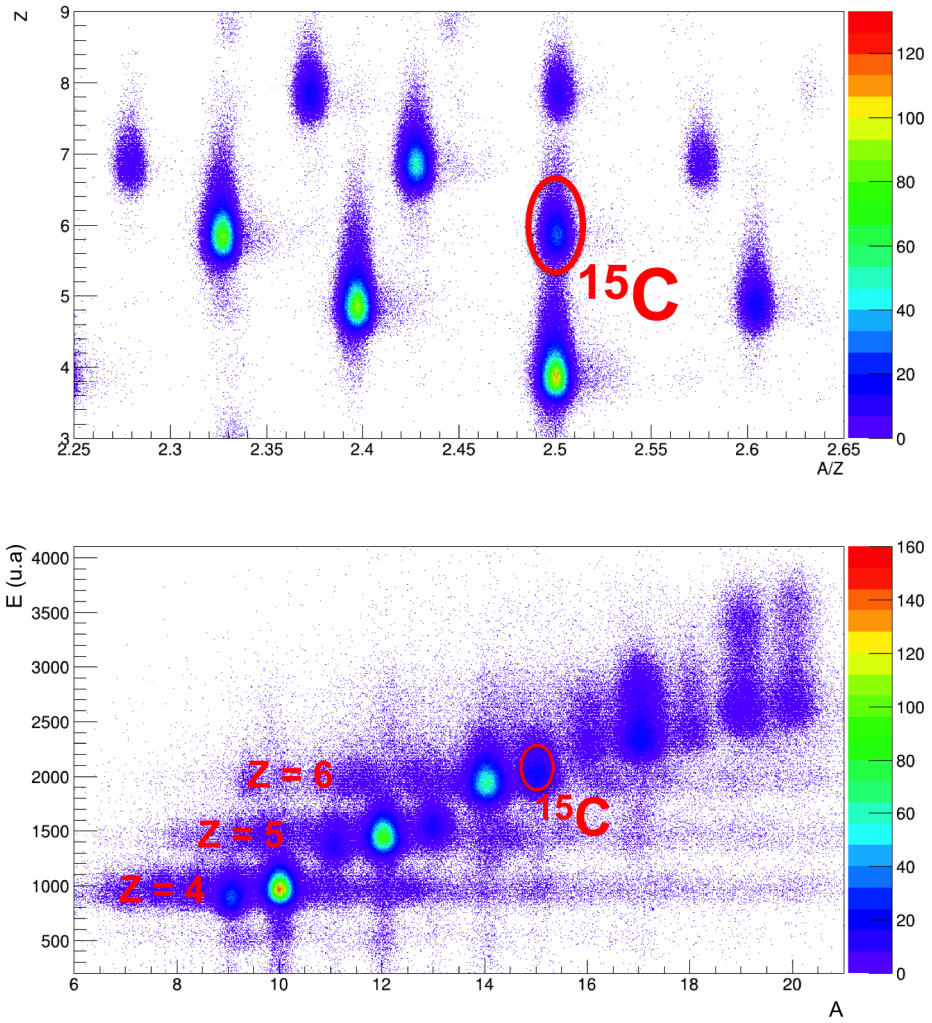

Figure 4.1: On the top the incoming beam identification plot for the the experimental setting 3 of FRS considered in the present analysis. The atomic number of the nuclei is plotted against their mass over charge ratio. On the bottom the reconstructed masses are plotted against the energy lost in the SST3.

The incoming projectiles are identified before the target by means of their time-of-flight and energy loss (section 3.3). By applying a bi-dimensional graphical cut with an elliptical shape, we gate the events of our isotope (^{15}C) characterized by an atomic charge of 6 and a mass-to-charge ratio of 2.5.

Moreover regarding to guarantee the atomic charge Z=6 before and after the target, elliptical gates were applied to the energy loss on the SSTs and simultaneously in TFW. Figure 4.2 shows the energy loss on the k side of SST1 versus SST2

and SST3 versus SST4. This gate assures that only carbon isotopes were considered before and after the reaction.

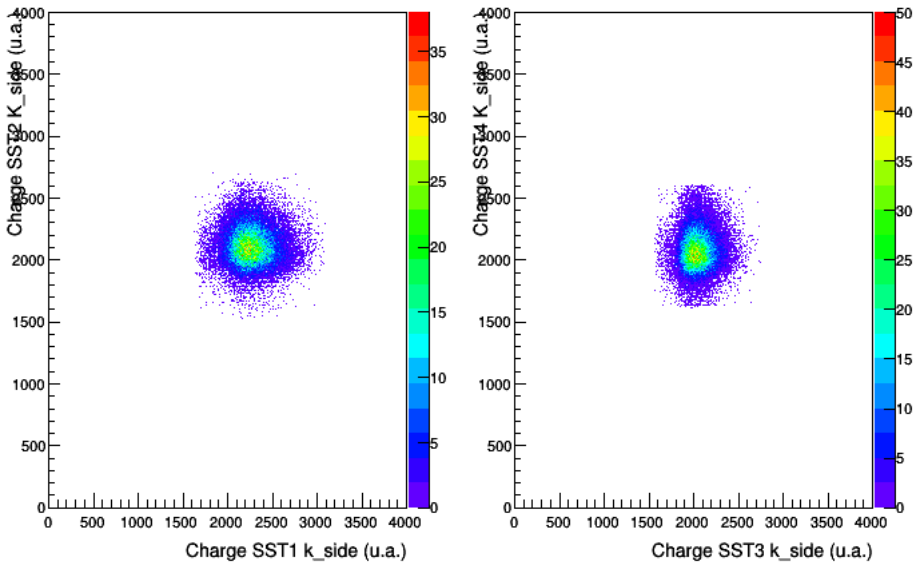

Figure 4.2: Energy loss in the K side of the SSTs 1 versus 2 on the left and 3 versus 4 on the right after the energy cuts applied.

After the target by using the *tracker* routine (section 3.5) which calculates the trajectories of the fragments through the ALADIN magnetic field, their masses, velocities and total momenta vectors were obtained. Figure 4.3 shows the fragment mass with the Y axis in logarithm scale. In order to calculate the reaction cross section and moment distributions, the masses A=14 and A=15 should be clearly separated.

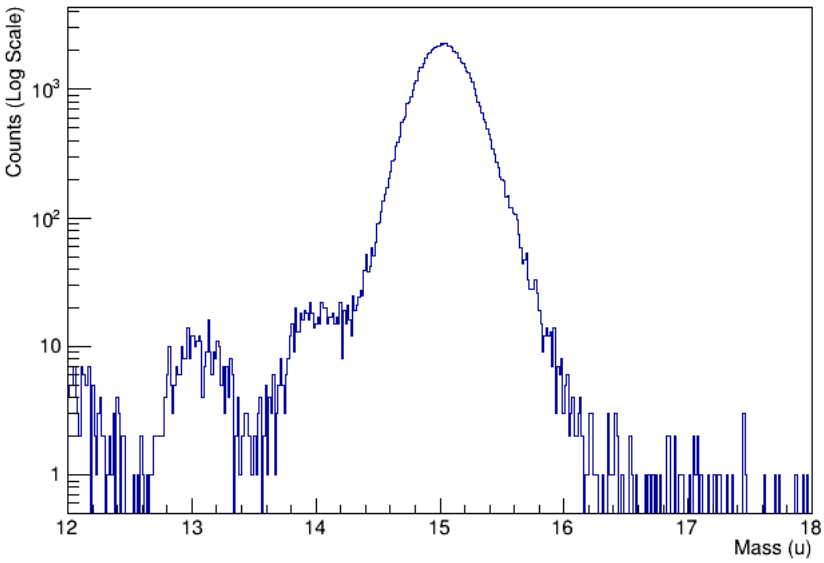

Figure 4.3: Reconstructed fragment mass with Y axis in logarithm scale. It was selected only ^{15}C Ions and SSTs energy cuts for Z=6 were applied.

However, the incoming selection of ^{15}C isotopes and the gates on energy loss corresponding to atomic charge (Z=6) did not allow a clear separation of mass A=15 and A=14. Complementary bi-dimensional cuts should be applied in order to better separate these masses.

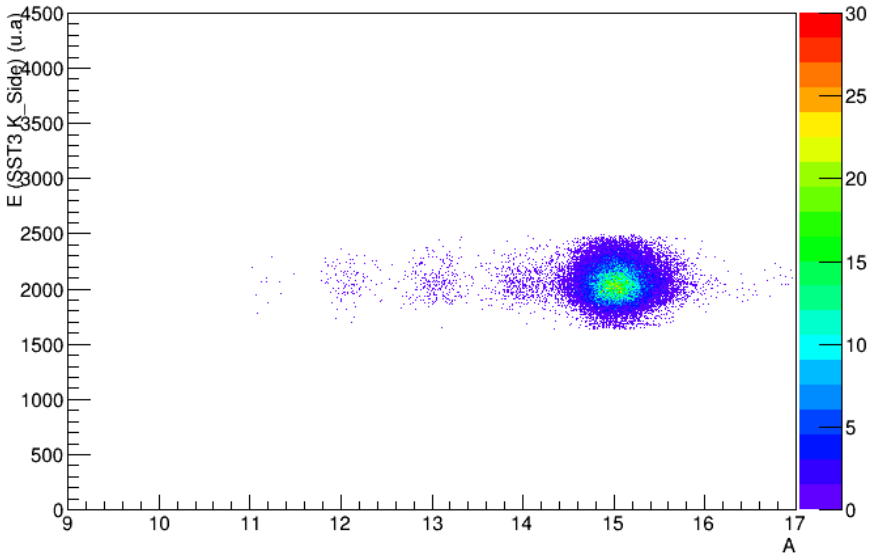

Figure 4.4: Energy loss on the K-Side of SST3 versus the fragment mass.

Combining the reconstructed mass with the energy loss in a SST and with the horizontal position on a GFI we can achieve a redundant but efficient mass separation. Figure 4.4 shows the energy loss on the K-Side of SST3 versus the fragment mass.

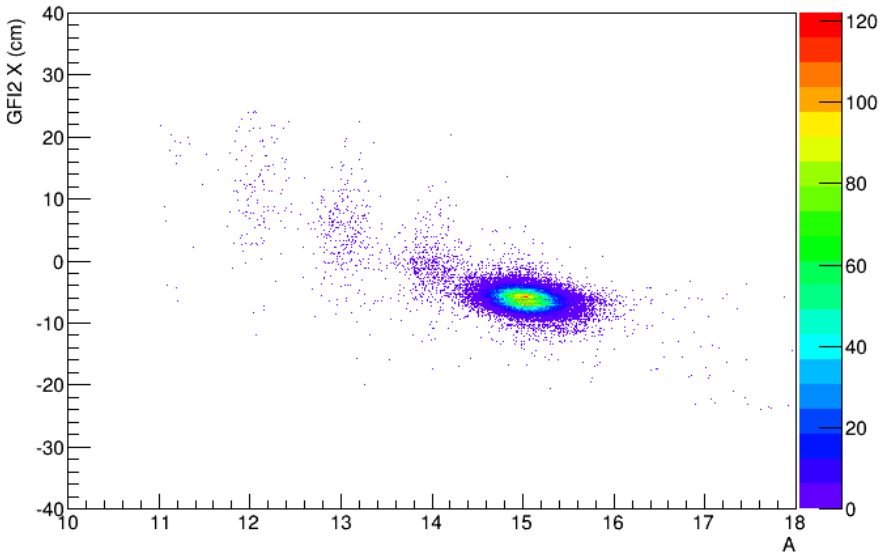

Figure 4.5: Horizontal position on the GFI2 versus the fragment mass.

Figure 4.5 shows the horizontal position from the GFI2 versus the reconstructed fragment mass. The inclusion of this cut in additions to previous ones allows a better control of the events selection. Later on the analysis, the selection cuts can be relaxed in order to the increase the statistics without loosing physical quantities control.

4.2 Momentum distributions

Momentum distributions are important physical observables which contain information about the orbital angular momentum of the removed nucleon along a reaction. After selection of the reaction of interest, the mass and velocity of each reaction fragment obtained from the heavy ion *tracker* introduced previously in section 3.5 are used to calculate its momentum $\vec{p}$,

$$\vec{p} = \beta\gamma m \tag{4.1}$$

which can be decomposed into a longitudinal $\vec{p_L}$ and a transverse $\vec{p_T}$ components.

$$\vec{p} = \vec{p_T} + \vec{p_L} \tag{4.2}$$

By using the angular information obtained from the Silicon Strip Detectors, it is possible to determine the transverse momentum components, p_x and p_y,

$$p_x = p_T.sin(\alpha_{X,out} - \alpha_{X,in}) \tag{4.3}$$

$$p_y = p_T.sin(\alpha_{Y,out} - \alpha_{Y,in}) \tag{4.4}$$

where $\alpha_{x,out}$ ($\alpha_{y,out}$) stands for the angle of the particles measured from the z axis in the xOz (yOz) plane for the fragments leaving the reaction target, and $\alpha_{x,in}$ ($\alpha_{y,in}$) stands for the angles measured from the z axis in the xOz (yOz) plane for the incoming beam nuclei before arriving to the reaction target.

Figure 4.6 shows the transverse momentum distributions calculated for x (p_x) and y (p_y) directions for the reaction ^{15}C -> ^{14}C on a CH_2 target. The result is consistent for the two distributions as expected. From now on it will be shown only the y component of the transverse momentum.

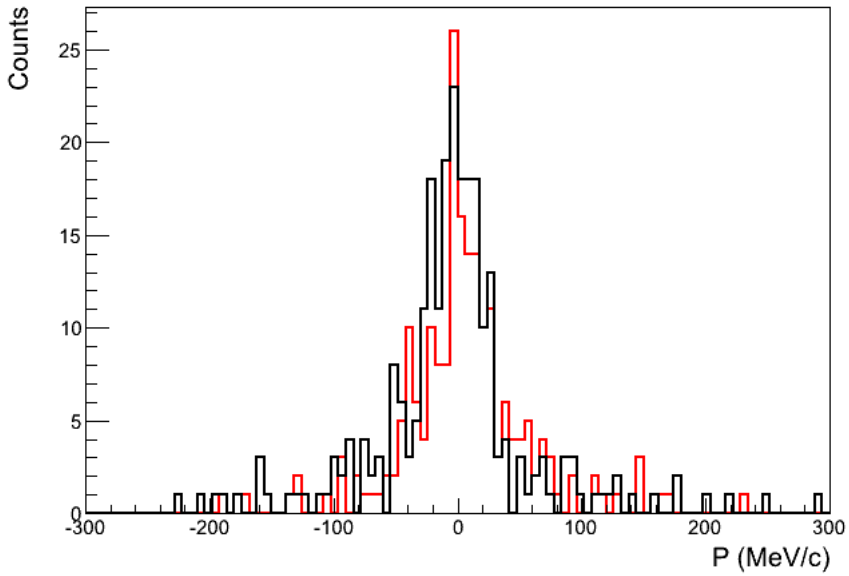

Figure 4.6: ^{14}C transverse momentum distributions from reactions on a CH_2 target for x component in black and for y component in red.

4.3 Differential cross section calculation

The cross section is a physical observable that reflects the probability that a nuclear reaction will occur. It is defined by:

$$\sigma = \frac{1}{\tau} P \tag{4.5}$$

Where P indicates the reaction probability within the target, and τ the target parameter which stands for the number of scattering centres per unit area.

$$\tau = \frac{\rho d}{M} \tag{4.6}$$

The quantities ρ, d and M correspond respectively to the target's mass density, thickness and the mass of the considered scattering centres.

The reaction probability P,

$$P(A \rightarrow B) = \frac{B}{A} \approx \frac{b}{a} \tag{4.7}$$

is defined as the number of reactions B divided by the number of repetitions of the reaction attempt A in the target. As B is much smaller than A, both numbers are further approximated by the number of reacted fragments b, and the number of unreacted fragments a. For the analysis considered in this work, b represents the number of detected ^{14}C, and a corresponds to the number of unreacted ^{15}C nuclei, both measured in the TFW detector. Furthermore the detection efficiency for each involved quantity should be included. However as these two fragments are measured in the same detector systems and had the same charge, the detection efficiencies are the same for both.

In order to obtain these quantities it will be used the transverse momentum distribution.

4.3.1 Background subtraction

In order to determine the contribution of other elements in the setup that could cause additional reactions, a so-called Empty Target (ET) run was performed using a secondary ^{15}C beam without any target at its nominal position. The contributions from the normalised ET run have to be subtracted to the measurements performed with the reaction target considered (T):

$$\sigma_T = \frac{1}{\tau_T} \times (P_T - P_{ET}) \tag{4.8}$$

During the experiment a Polyethylene (CH_2) reaction target was used. Of particular interest for us is the contribution of projectiles interacting only with the protons in the CH_2 target. By this, the carbon background has to be subtracted from the CH_2 target measurement via a normalised run with a graphite (C) target also measured during the beam time.

$$\sigma_{H_2} = \frac{1}{\tau_{CH_2}} \times (P_{CH_2} - P_{ET}) - \frac{1}{\tau_C} \times (P_C - P_{ET}) \tag{4.9}$$

developing the above equation we obtain:

$$\sigma_{H_2} = \frac{1}{\tau_{CH_2}} \times P_{CH_2} - \frac{1}{\tau_C} \times P_C - (\frac{1}{\tau_{CH_2}} - \frac{1}{\tau_C}) \times P_{ET} \tag{4.10}$$

from there we obtain the cross section for the reaction on hydrogen.

$$\sigma_{proton} = \frac{1}{2} \times \sigma_{H_2} \tag{4.11}$$

Figure 4.7 shows the normalized transverse momentum distribution for unreacted fragments ^{15}C (left canvas), and for the reacted fragments ^{14}C (right canvas). The black line correspond to the distribution obtained with the CH_2 run while the distributions in red and blue are obtained from Carbon and Empty runs respectively. All the distributions were normalized to the CH_2.

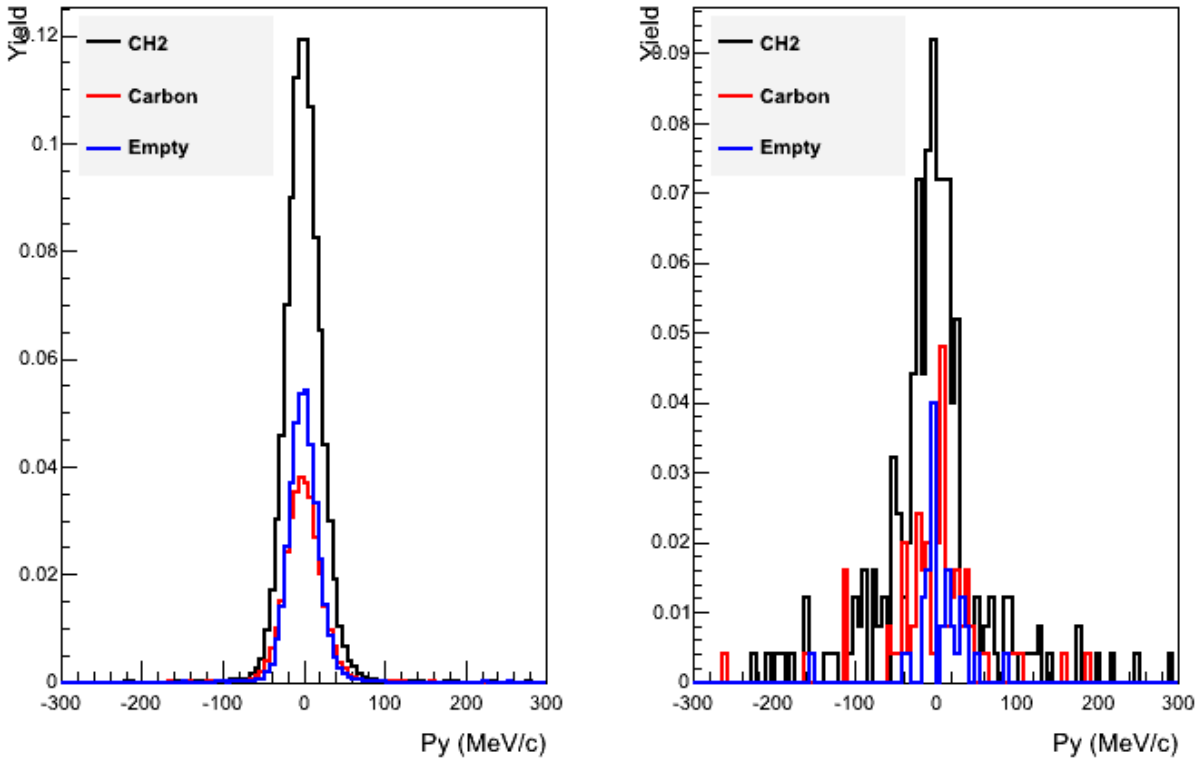

Figure 4.7: Normalized momentum distributions for unreacted events (^{15}C) on the left and reacted events (^{14}C) on the right. The color code represents the data obtained during the CH_2, Carbon and Empty runs.

Regarding the number of active centers present in each target, in the S393 experiment for the setting 3 of FRS, the properties of two targets considered (CH_2 and Carbon) are in Table 4.1.

Target	$\rho_t[g/cm^3]$	$d_t[mm]$	$A_T[g/mol]$
Polyethylene	0.94	9.81	14.027
Carbon	1.84	5.08	12.011

Table 4.1: Target table.

As an example table 4.2 resumes the number of events for each target run, respectively for reacted ^{14}C and unreacted ^{15}C with all the included cuts and the trigger pattern (tpat2), which was used for the calculation of the inclusive momentum distribution shown on figure 5.1, and to the total inclusive cross section (figure 5.2).

	CH_2	**Carbon**	**Empty**
Reacted	250	75	36
Unreacted	42266	13748	16063

Table 4.2: Resume table for the number of unreacted ^{15}C fragments and reacted ^{14}C fragments with CH_2, Carbon and Empty target runs.

4.3.2 Study of aperture cut on the cross section

The cross section calculation strongly relies on the number of detected fragments and projectiles. In the frontiers as the result of possible contaminations, distinguish events of isotopes with neighbours masses or atomic charge can be demanding and affect the extraction of the cross sections. In this work the separation of mass A=15 and A=14 (figure 4.3) is critical. In order to gate the correct fragment mass we selected events from a bi-dimensional elliptical cut on the TFW energy versus the fragment mass. As the accurate distinction between mass 14 and mass 15 was difficult, determined by a Gaussian fit of the centroid and the sigma for each mass, a study of stability for differential momentum distribution was performed. This study was made considering variations of 0.2 sigma in the elliptical cut on the CH_2 and Carbon runs.

By using those events selections the differential momentum distribution and the correspondent cross section was calculated for (tpat2) and (tpat8) shown in figures 4.8 and 4.9.

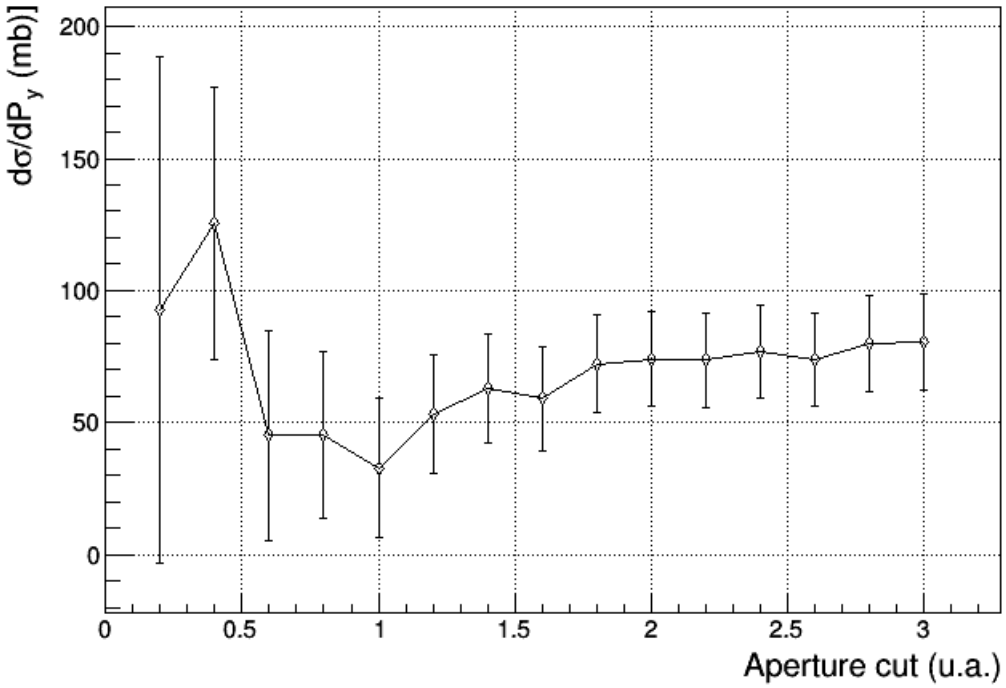

Figure 4.8: Variation of selection cut versus cross section value in the case of inclusive knockout.

The shape of the momentum distributions according the size of the aperture with steps of 0.2 sigma is shown in the appendix.

Making the same study for the case when it was asked 2 particles in the Crystal Ball we obtained the figure 4.9.

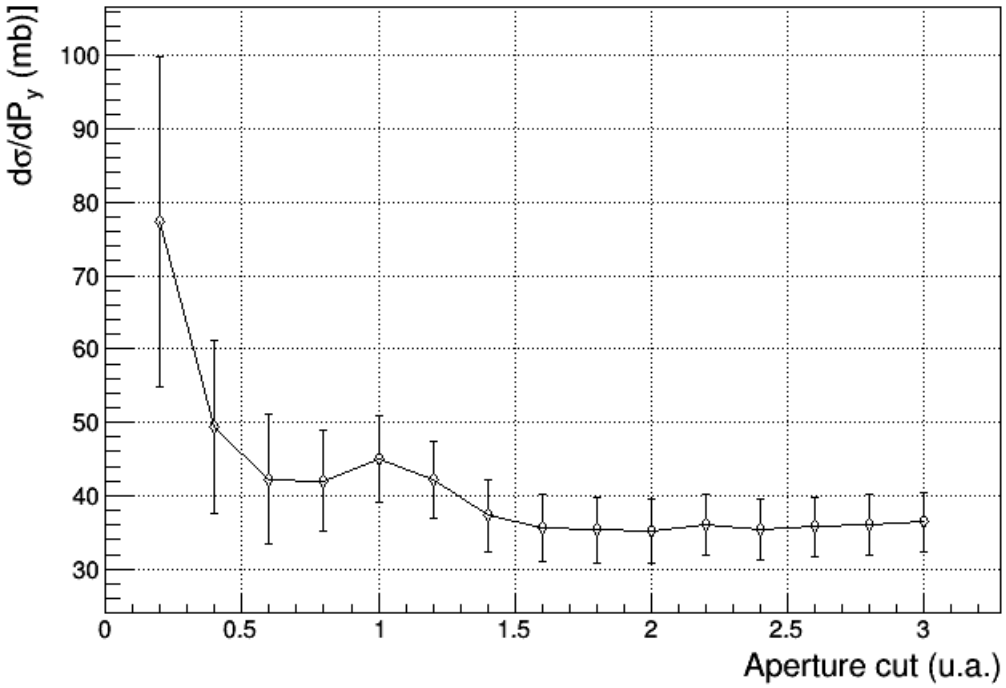

Figure 4.9: Variation of selection cut versus cross section value in the case of exclusive knock-out.

By analysing the previous plots it was decided to use a 1.8 sigma aperture cut (mass versus TFW energy) obtaining a 72 (mbarn) for H (protons) Cross Section with a total uncertainty of 19 (mbarn) for (tpat2) and 35 (mbarn) for H Cross Section with an error of 4 (mbarn) for (tpat8).

4.4 Angular correlations for protons and neutrons

Quasi-free scattering events have a very strong angular correlation which are dominated by the kinematics of free proton-neutron scattering. By selecting the ^{15}C incoming and ^{14}C outgoing ions, we only selected the one neutron removal reactions, although to ensure the selection of quasi-free (p,pn) reactions we need more information. The angular correlation of the proton and neutron measured in Crystal Ball gives a clear signature of the quasi-free scattering reaction.

The measured angular correlations between protons and neutrons in spherical coordinates where θ corresponds to Polar angles and the ϕ to the Azimuthal angles

are shown in the schematic Figure 4.10.

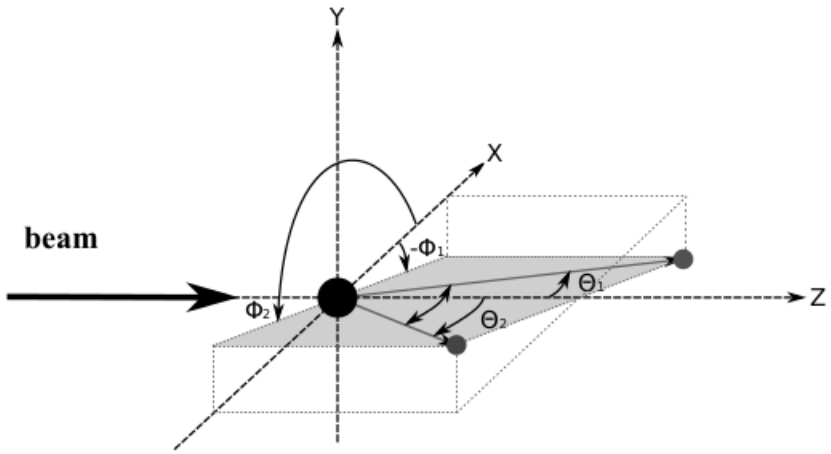

Figure 4.10: Schematic view of proton-neutron angular distribution in spherical coordinates.

Figure 4.11 shows the opening angle of the pair of nucleons, which corresponds to the sum of polar angles θ for each nucleon (left canvas). Typically under QFS conditions this value is around 80°. The right canvas of the figure shows the polar angle of one nucleon versus the angle of the second nucleon.

The angular distribution of scattering nucleons is affected specially by the separation energy of the nucleon and at its kinetic energy. When the two nucleons are unbound at non relativistic energies, they share an average opening angle of 90 degrees. When one nucleon has a large kinetic energy (approximately 0.7 of the speed of light), due to the relativistic mass of the incident nucleon is larger than the mass of the motionless nucleon, the average opening angle between the two scattered nucleons is expected to be smaller, of approximately 80 degrees [94].

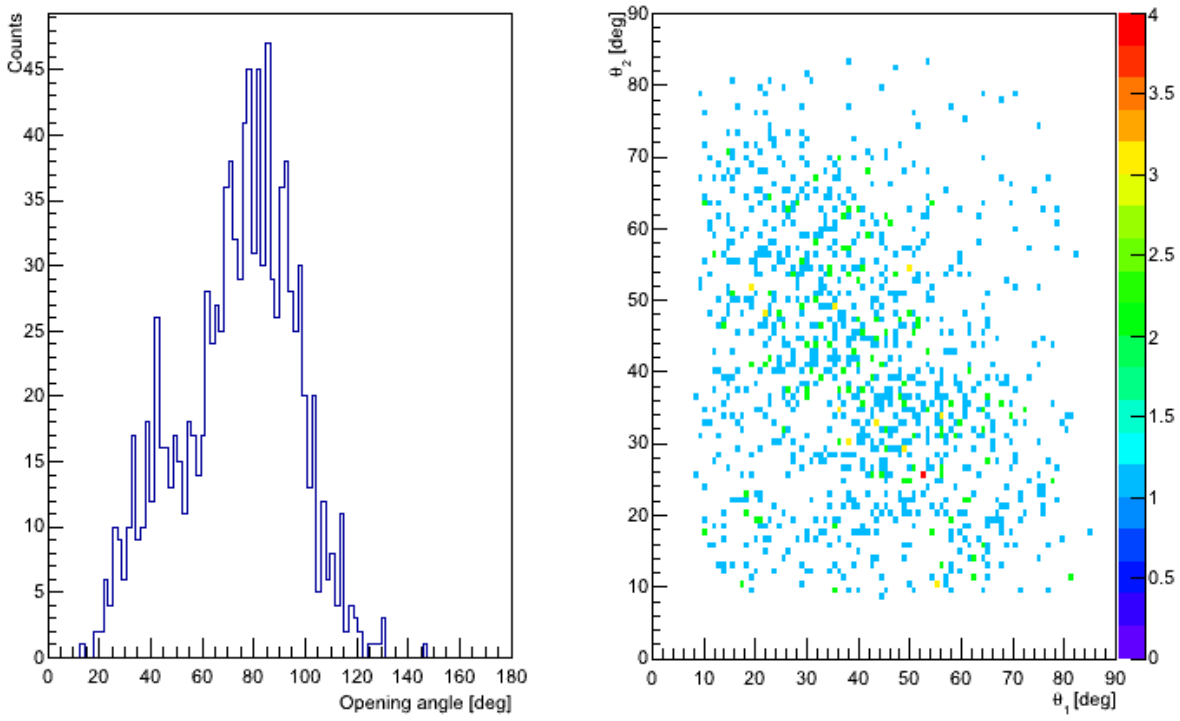

Figure 4.11: Left canvas shows the opening angle for the neutron and the proton. Right canvas shows the polar angle of one of the nucleons versus the polar angle of the other.

Figure 4.12 shows (left canvas) the difference between the azimuthal angles ϕ of the two nucleons. In the QFS limit a typical value of 180° is expected. Right canvas shows the correlation of azimuthal angles of both nucleons.

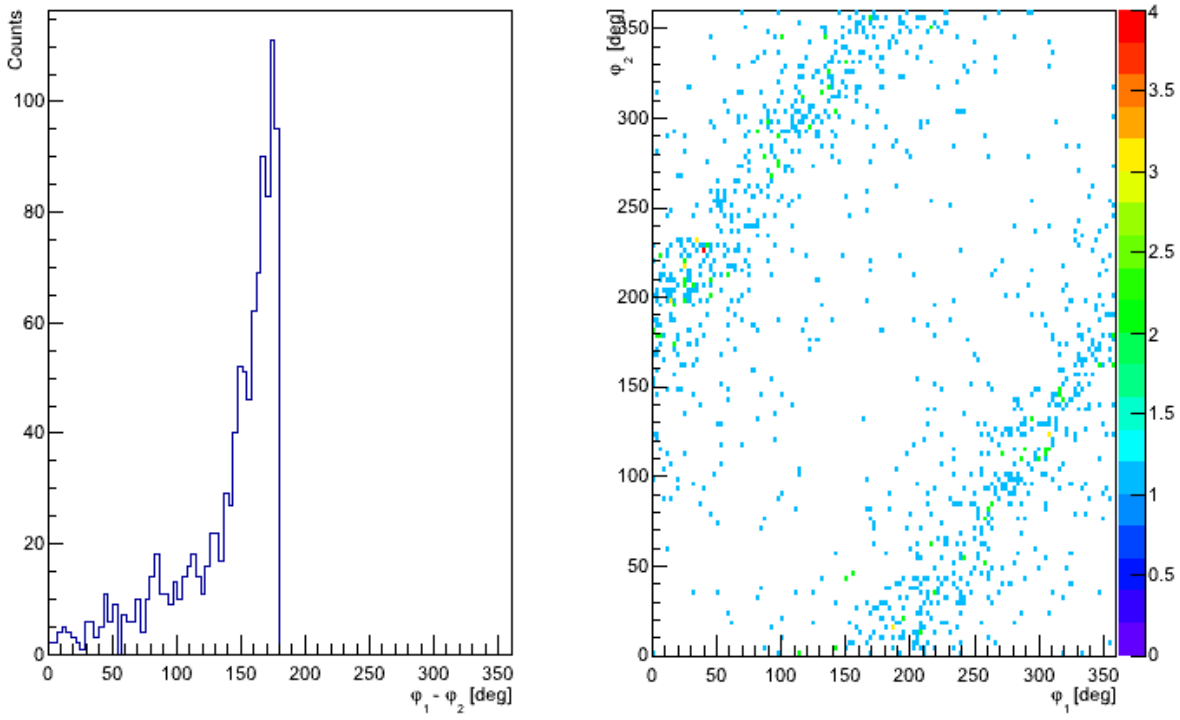

Figure 4.12: Left canvas shows the difference between the azimuthal angles of both nucleons. Right canvas is shown the correlation of azimuthal angles of both nucleons.

The events in this figure are gated on the incoming ions ^{15}C and the outgoing ions ^{14}C with TPAT=8 trigger corresponding to a signal in the POS detector, a VETO in ROLU, one signal in TFW and a signal in Crystal Ball. The low efficiency of neutrons detection is a limitation for the analysis and should be determined by simulations. Combining this data information with the neutrons efficiency detection and the Downscale factor it is possible to extract the ^{15}C(p,pn)^{14}C QFS reaction cross section and inclusive momentum distributions.

4.5 Crystal Ball response simulations

The data analysis of this work requires the use of Montecarlo simulations in order to obtain some physical quantities. The response of the Crystal Ball detector to high energy protons and neutrons emerging from the reaction as well as to γ-rays from core de-excitation must be.

These simulations were performed within the R^{3}BRoot Framework included in the FairRooT [97] software package regarding the determination of Crystal Ball efficiency for particle detection and the study of the γ spectra. The FairRooT software package is based on Root [89] allowing the simulation and data analysis of different FAIR experiments. The R^{3}BRoot is an analysis and simulation Framework which uses Geant3 and Geant4 [98] as particle transport engines and has been developed for the future R^{3}B setup at FAIR [79], furthermore implementing the LAND-R^{3}B detectors and geometry used in the S393 experimental campaign.

Unlike with other detector systems the Crystal Ball efficiency must be considered in order to determine the (exclusive) cross section which relies in the number of events where two nucleons (proton an neutron) emerged from the reaction. As this efficiency can not be determined experimentally, it can only be determined by means of simulations. One of the advantages of the R^{3}BRoot framework is the used of the same analysis tools for simulated data and real experimental data, treating the data on the same footing and thus reducing the systematic uncertainties associated to data analysis .

In the recent years two different approaches have been considered to address the issue of the Crystal Ball efficiency's calculation. A Montecarlo event generator that creates a distribution of particles derived from calculated kinematically fully exclusive cross sections within the Faddeev/AGS reaction framework, was developed by P. Díaz [31]. Prior to this work,the R^{3}B collaboration generally used a kinematical code (which was considered in the present thesis) developed by L. Chulkov and V. Panin [94], that generates events with protons (scattered from the target) and neutrons (ejected from the fragment projectile) following QFS kinematical conditions. The generated particles emerge from the center of the target with the beam spot dimension and anisotropy [99,100] parameterized according to the experimental elastic p-n cross section [100].

Considering the beam energy and the mass of incoming and outgoing nucleus as input, the resulting angular correlations under these conditions are shown in figure 4.13. As expected under the QFS conditions the open angle between the two nucleons was approximately 85° and the difference in azimuthal angle of approximately 180°.

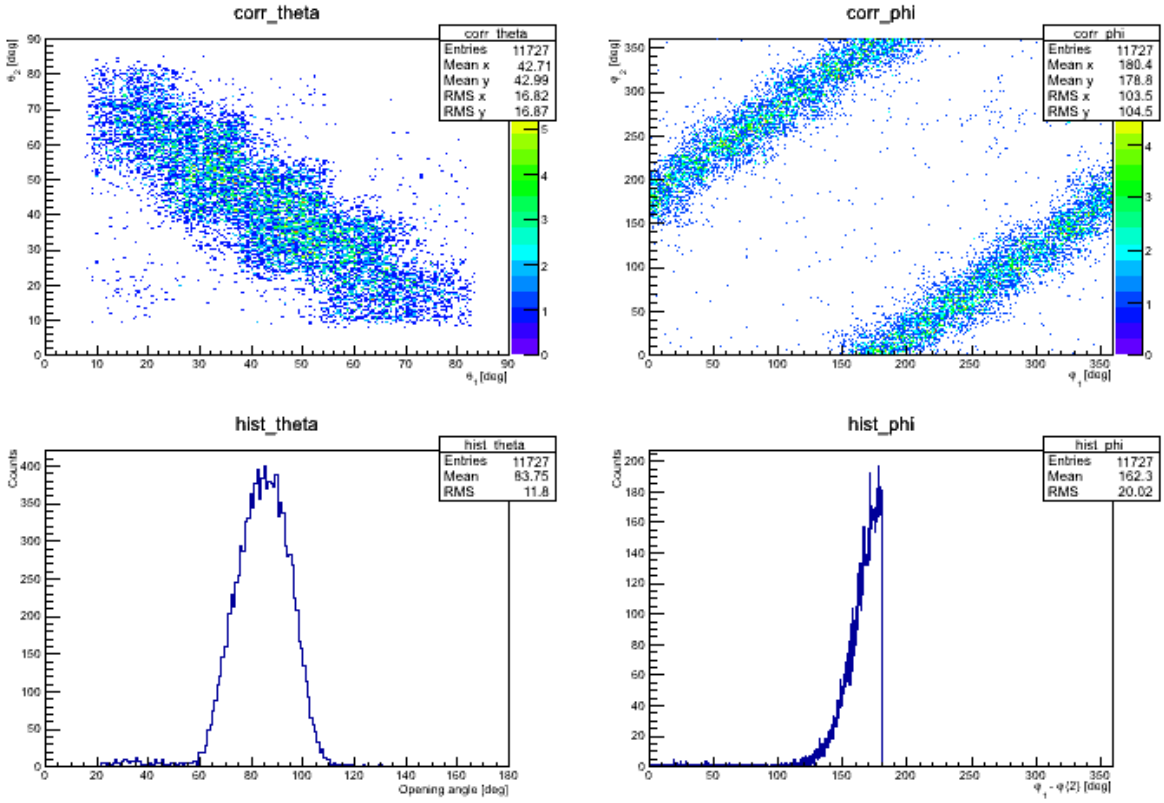

Figure 4.13: Simulated angular correlations of the neutron and proton for the ^{15}C(p,pn)^{14}C.

The detection efficiency of nucleons in Crystal Ball is obtained by the ratio of effectively reconstructed on Crystal Ball and the total number of events. In the analysis performed, we required that Crystal Ball detects simultaneously a pair of a proton and a neutron, therefore the efficiency will be determined by the ratio of simulated events which were reconstructed with a nucleon multiplicity of 2 and the total number of simulated events.

The determination of this value strongly depends on which *physics lists* is used in the simulation. Those *physics lists* refers to classes which provide the physics models, particle types and reaction cross sections [98, 101]. GEANT4 offers several *physics lists* and the selection of the best according each application can be complex. This has been discussed lately by the R^{3}B collaboration community. In this work few of them were used and tested. We can divided those in two groups, the hadronic physics which is dedicated to reactions triggered by long lived hadrons and

extended to γ-rays from 0 to 1 GeV *(binary ion, qgsp bertini and qgsp inclxx)*, and the electromagnetic which is dedicated to the physics processes for photons, electrons and positrons (penelope and standard). A detailed description of each physics list can be obtained in reference [101]. The tested options considered for hadronic and electromagnetic physics list are shown on table 4.3.

	Physics list
pl1	standard + qgsp bert
pl2	standard + qgsp bert + ion inclxx
pl3	penelope + qgsp bert
pl4	penelope + qgsp bert + ion inclxx

Table 4.3: Physics list.

Table 4.4 shows the results of simulated efficiency of detecting a proton and a neutron in Crystal Ball using different physics list.

	pl1	**pl2**	**pl3**	**pl4**
Gauss	16.14%	16.28%	15.47%	15.40%
Elast.(p,n)	15.25%	15.42%	14.38%	14.58%

Table 4.4: Efficiency for different physic lists.

In this work, the adopted efficiency was (15.25$\pm$0.87)% corresponding to pl1, which stands for standard and Bertini physics lists. The uncertainty was determined by the largest difference to the other ones tested. Moreover, a non Gaussian distribution of generated particles was used.

5

Results and Discussion

Contents

In this chapter, the results based on the reconstruction procedure and analysis described in the previous chapter will be presented.

In the first section it will be introduced the used nomenclature which refers to inclusive and exclusive neutron knockout. The following two sections will be focused respectively on the particle inclusive/exclusive neutron knockout study. It will be shown and discussed for each case the differential cross section and their associated uncertainties for the ^{15}C one neutron removal reaction, for the CH_2 and C targets. For the case of exclusive study, it will also be shown the angular distributions and correlations for the emerging proton and the neutron and the comparison with the simulated results. The momentum distributions will be also shown and the width will be discussed. The de-excitation gamma rays measured with the Crystal Ball detector and comparison with the simulated gammas of interest will also be done. Last section of the chapter is dedicated to the study of inclusive neutron knockout by using the Crystal Ball without any particles requirement.

5.1 Inclusive and exclusive analysis approaches

First we shall explain the used terminology in this thesis. In this work two different analysis methods leading to different reaction mechanisms approaches are considered. The first one to be introduced is the *Particle Inclusive Neutron Knockout* (Section 5.2) which stands for the analysis when only the heavy fragment is detected, ^{15}C(p,X)^{14}C, and the final state of the fragment is not distinguished. The second one is the *Particle Exclusive Neutron Knockout* (Section 5.3) which in the analysis, the heavy fragment is detected together with the emerged light particles from the ^{15}C(p,pn)^{14}C reaction and γ-rays from core de-excitations. Based on the previous chapter analysis methods, the physical quantities of interest for each approach will be presented in the following sections.

5.2 Particle inclusive neutron knockout study

This section presents the study of the Inclusive Neutron Knockout of the ^{15}C(p,X)^{14}C breakup reaction which means that the final states of the fragments were not distinguished. The observables of interest, momentum distributions and cross section will be extracted by studying the incoming ^{15}C projectiles and the ^{14}C fragments neglecting the analysis of any signal of protons, neutrons or γ-rays in the Crystal Ball detector. The obtained results with this analysis method for the carbon and CH_2 targets will be shown as well.

5.2.1 Momentum distributions and cross section

By means of the time-of-flight between S8 and POS detectors and the energy loss on the PSP the ^{15}C incoming projectiles were identified within the cocktail beam that reached cave C. Those events were selected (section 4.1) by means of bi-dimensional cut. The used trigger pattern was (TPAT2) which means the selected events in the analysis had obligatory a signal on POS detector and on TFW (subsection 2.3.1). Using the same (TPAT2) trigger pattern, the ^{14}C outgoing fragments, produced by the interaction of ^{15}C incoming projectiles with the CH_2 target were identified by the energy loss in the SSTs and TFW detectors moreover the reconstructed mass by tracker (section 3.5).

After the reaction channel selection, as explained, the masses and velocities of reaction fragments with the angular information from SSTs were used to the calculation of its momentum. In fact in a nucleon removal reaction, the widths and shapes of momentum distribution give important information on the removed nucleon along the reaction. The transverse momentum distribution was investigated for CH_2 and Carbon targets, along the X (horizontal) and Y (vertical) directions. Because of a malfunctioning of the SST1 during the experiment [60–62, 69, 70, 93], the achieved information from the Y component provides higher accuracy, consequently only momentum distributions on Y direction will be considered.

For the considered FRS production setting (setting 3, centred on ^{20}O) the (TPAT2) trigger pattern was downscaled by a factor of 64 which means that, in 64 events only one was recorded by the DAQ. This fact contributed for a lack

of statistics, especially perceived into the estimation of momentum distribution shapes. It was difficult to draw accurate conclusions about the momentum distribution shape for the Carbon target. Figure 5.1 shows the Y projection of the transverse momentum distribution on a CH_2 target. By applying a Gaussian fit it was obtained a Full Width at Half Maximum (FWHM) of (61 ± 29) MeV/c.

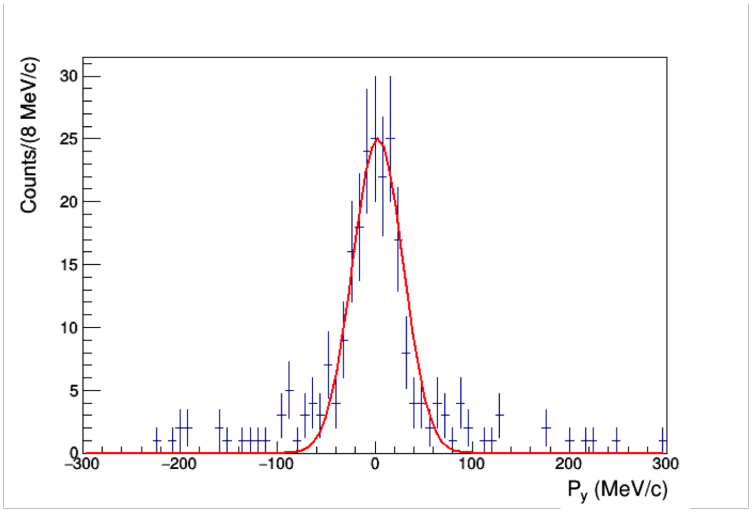

Figure 5.1: Inclusive transverse momentum distribution for the ^{15}C neutron breakup reaction with a CH_2 target. A FWHM of (61 ± 29) MeV/c was measured when fitted by a Gaussian function, without considering the straggling of the beam.

By subtracting the straggling of the beam [93] using equation 5.1:

$$\Gamma^2_{(^{15}C(p,X)^{14}C)} = \Gamma^2(^{14}C) - \left(\frac{m(^{14}C)}{m(^{15}C)}\Gamma(^{15}C)\right)^2 \tag{5.1}$$

where Γ is the momentum width, the (^{14}C) and (^{15}C) are the reacted and the unreacted fragments and respectively, $m(^{14}C)$ and $m(^{15}C)$ the isotopic masses, a width of 43 ± 23 MeV/c for the inclusive neutron breakup reaction was obtained.

The cross section determination (equation 4.11) of the neutron removal reaction depends only on the number of incoming ^{15}C projectiles, the number of reacted ^{14}C fragments and the target characteristics. As the number of detected projectiles and fragments is only a fraction of total projectiles and fragments, the detection effi-

ciency of the various detector systems has to be taken into account as well. However, for the inclusive total cross section calculation the detection system efficiency is the same for both the projectiles and fragments, and can be neglected. By integrate the inclusive momentum distributions, the total inclusive cross sections were obtained. As mentioned before the analysis was performed further using data from runs which the CH_2 target was replaced by a Carbon and a Empty target. This allowed the estimation and consequently the subtraction of the Carbon and the background contributions (subsection 4.3.1) in the cross section calculations. Table 5.1 shows the inclusive cross sections and the respective uncertainties for the neutron breakup reaction on a CH_2, Carbon and as well on the reconstructed protons targets.

Target	**Cross Section(mb)**
CH_2	369 ± 12
Carbon	225 ± 14
Proton	72 ± 19

Table 5.1: Resume table for the inclusive cross sections and the respective uncertainties for CH_2, Carbon targets. Finally the calculated values for the reaction with protons.

Cross section uncertainties were calculated using the propagation uncertainty formula associated to the involved uncertainties which are the statistical uncertainties associated to the reacted and unreacted fragments in the different runs for different targets and the uncertainty associated to the target thickness. The highest contributions for the total uncertainty were the statistical uncertainties associated to the reacted fragments to CH_2 and Carbon runs.

Figure 5.2 shows the differential transverse momentum for the Y direction. The data was normalized and corrected by the subtraction bin-by-bin of carbon and background contributions. The differential cross section of ^{15}C(p,X)^{14}C breakup reaction on a protons target was determined by integration of the distribution. A value of (72 ± 19) mbarn was obtained.

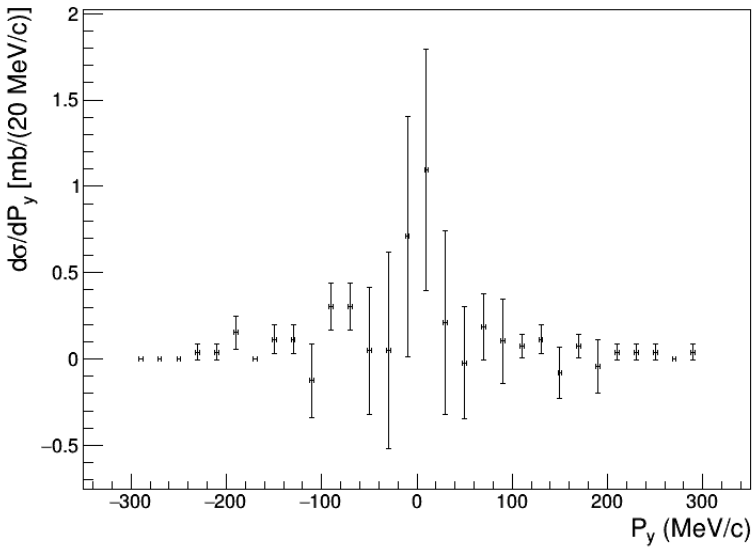

Figure 5.2: Inclusive transverse momentum distribution of ^{15}C(p,X)^{14}C breakup reaction.

The observed fluctuations in the distribution were caused by the moderate rate on the ^{15}C production of the considered reaction setting, combined with a large downscale factor applied via software to the data acquisition system, which were amplified by the subtraction of the Carbon target contribution. Once again, this fact restrained the analysis of the inclusive momentum distribution shape and the total cross section calculation has a considerable associated uncertainty.

5.3 Particle exclusive neutron knockout study

In this section the performed study of the exclusive neutron knockout of the ^{15}C(p,pn)^{14}C breakup reaction will be shown. The observables of interest will be extracted by studying the number of incoming projectiles, the number of reacted fragments, and as well by detecting on Crystal Ball the proton and neutron emerging from the reaction. As a consequence of the malfunction of two SSTs which were surrounding the target (Box) (section2.2.2.A), it is not possible to distinguish between the emerged proton and neutron. Nevertheless, by detecting two nucleons on Crystal Ball it can be assumed that one is the neutron and the other the proton. In addition to the exclusive momentum distributions and to the cross sections it will be shown the proton-neutron correlations and the γ-rays analysis.

5.3.1 Momentum distributions and cross section

The determination of the exclusive momentum distributions for the ^{15}C(p,pn)^{14}C breakup reaction depends on the incoming ^{15}C projectiles selected with the trigger pattern (TPAT2), the number of reacted ^{14}C projectiles measured in coincidence with two nucleons in Crystal Ball.

The reaction channel tagging was performed according to the description in the previous section, with the difference that the reacted ^{14}C fragments were selected considering the trigger pattern (TPAT8) which means a signal in POS, a signal in the TFW and a signal in the Crystal Ball. This trigger pattern had no downscale factor aplied, and as such every event fulfilling these conditions was recorded by the DAQ (subsection 2.3.1). This fact helped to overtake the low statistical issues mentioned in the previous section.

In order to distinguish the two nucleons in the Crystal Ball from the γ spectra an average threshold of 20 MeV for each crystal was pre-determined and applied into the addback algorithm.

Using equation 4.4 the exclusive transverse momentum distributions for the Y direction were determined. Figure 5.3 shows the momentum distributions for the ^{14}C neutron breakup on the CH_2 and carbon targets. By adjusting the experimental distribution to a Gaussian fit and removing the straggling effect of the beam (equation 5.1) of (43 ± 10) MeV/c and (35 ± 10) MeV/c were obtained for the CH_2 and Carbon targets respectively.

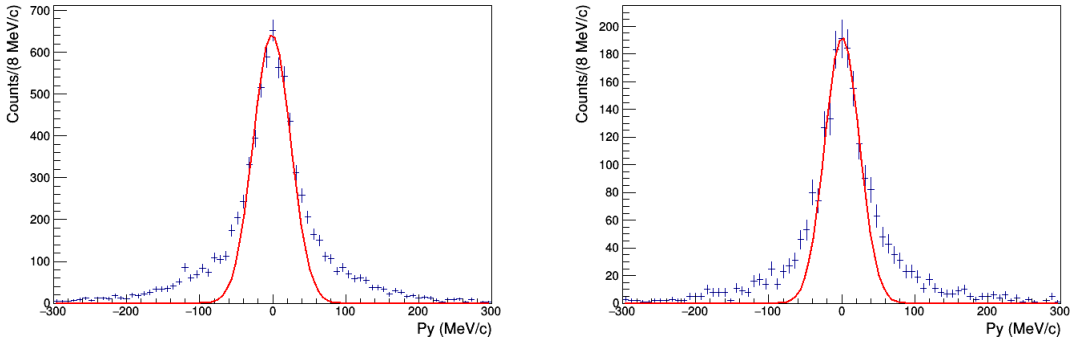

Figure 5.3: Exclusive transverse momentum distributions for a neutron breakup reaction on a CH_2 target on the left and for a Carbon target on the right. In red it is shown the Gaussian fit applied in order to determine the widths of (42.8±9.5) MeV/c and (34.9±9.8) MeV/c respectively.

In order to determine the exclusive cross section the method described in the previous section was used. However in this approach the detection of two emerged nucleons from the reaction is required. For this reason it is necessary to include the efficiency of detecting a neutron and a proton in Crystal Ball. This efficiency was obtained by simulations (section 4.5) and its value of 15.25 % was considered in the calculation. Table 5.2 shows the results for the exclusive cross sections and the respective uncertainties for the ^{15}C neutron breakup on CH_2, Carbon and proton targets.

Target	**Cross Section(mb)**
CH_2	172 ± 3
Carbon	101 ± 3
Proton	35 ± 4

Table 5.2: Resume table for the exclusive cross sections and the respective uncertainties on CH_2, Carbon and reconstructed protons target.

Figure 5.4 shows the exclusive transverse momentum for the Y direction. The data was normalized and corrected by the subtraction of carbon and background contributions. The exclusive differential cross section of ^{15}C(p,pn)^{14}C breakup reaction on a protons target was determined by integration of the distribution. A value of 35 ± 4 mbarn was obtained.

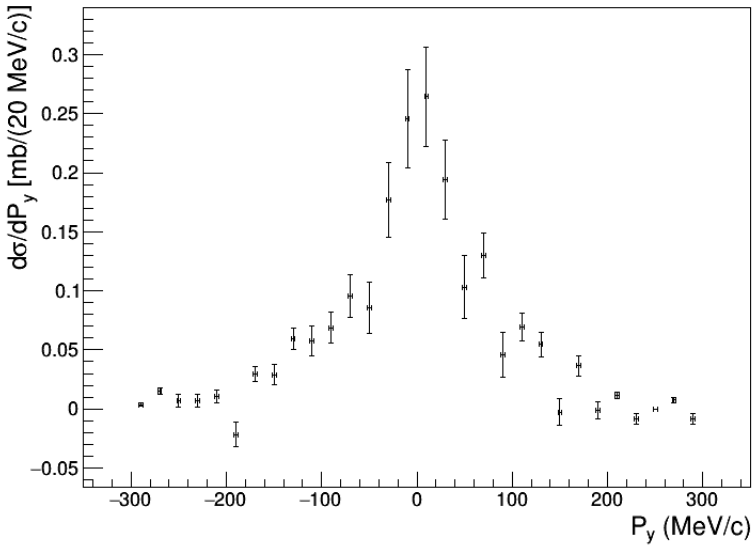

Figure 5.4: Exclusive transverse momentum distribution of core in the ^{15}C(p,pn)^{14}C breakup reaction with the signal requirement of two hadrons in Crystal Ball.

As the trigger pattern used to select the ^{14}C reacted fragment was not affected by any downscaling factor, the statistic of fragments increased if compared to the inclusive approach, with the consequence that the observed fluctuations disappeared. Moreover it is easier to extract conclusions about the shape and width of the momentum distributions. In the next chapter the obtained shapes and cross sections will be discussed and compared to the Faddeev theoretical results.

5.3.2 Proton-neutron correlations

The detection of two nucleons in Crystal Ball in coincidence with the ^{14}C fragment allows the analysis of possible proton-neutron angular correlations. As mention before the malfunction of the (Box) SSTs does not allows to distinguish protons and neutrons, moreover the nucleons angular resolution is lower. In order to reproduce a realistic angular distribution, the measured angles with Crystal Ball were randomised within the solid angle of the corresponding crystal by a randomization algorithm.

The angular distributions are presented for experimental data obtained on CH_2 and Carbon targets and also for comparison it was plotted a correlation from simulated data analysed with an identical routine as the experimental data. Figure 5.5

shows the proton-neutron angular distributions with a CH_2 target for experimental data.

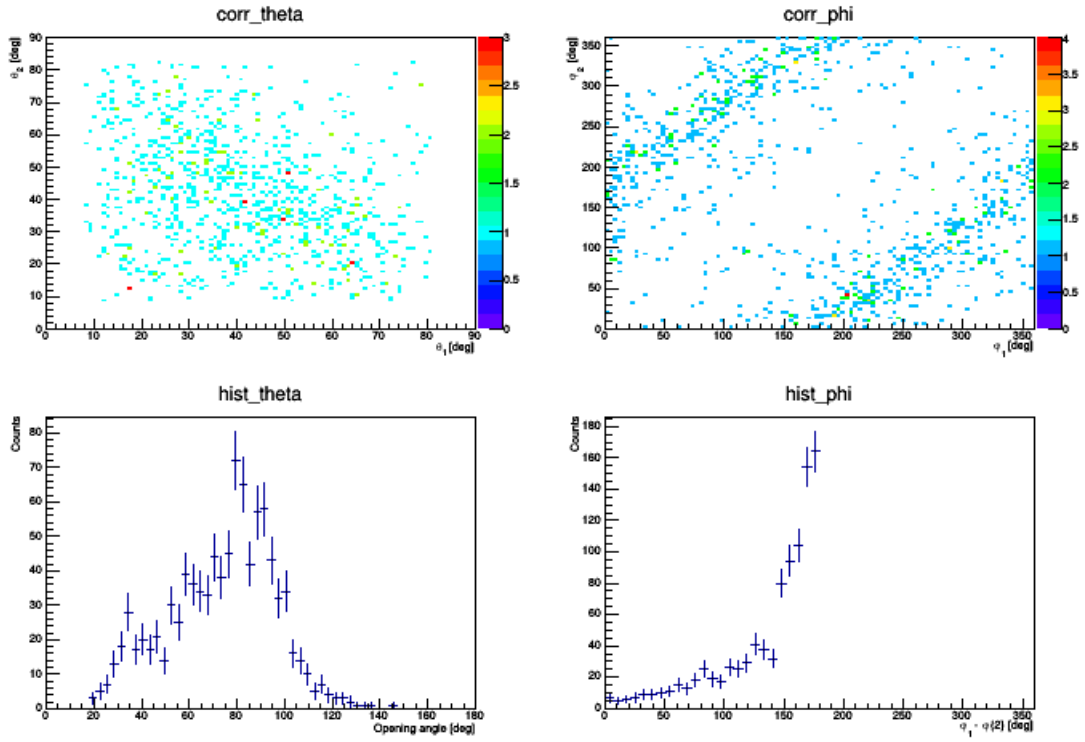

Figure 5.5: Proton-Neutron angular correlations for a breakup reaction with a CH_2 target at at approximately 500 MeV/u.

The obtained correlations for the two nucleons are shown in the upper panels of figure. From the left bottom plot it is possible to identify that the θ angles are distributed majority around 80° of opening angle. In the right side it is observable a maximum peak around 180° for the φ angle.

Figure 5.6 shows the proton-neutron angular distributions with a Carbon target for experimental data.

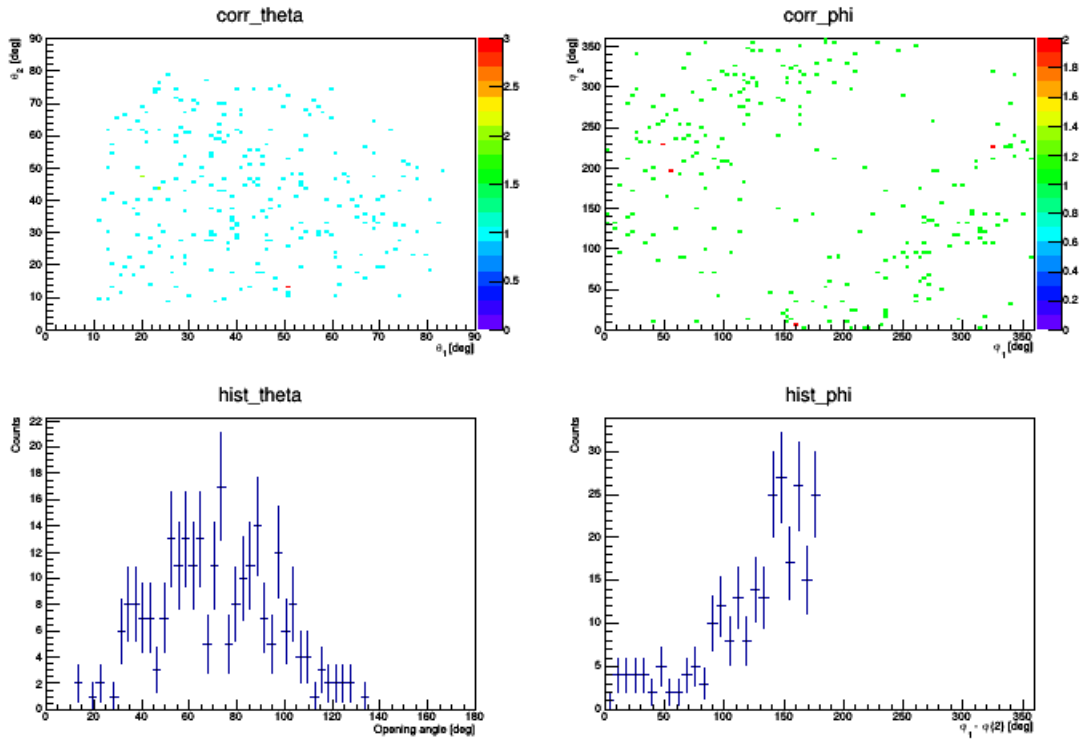

Figure 5.6: Proton-Neutron angular correlations for a breakup reaction with a Carbon target at at approximately 500 MeV/u.

As it is possible to observe the Carbon contribution is responsible to create a broad band which can be interpreted as peripheral reactions between ^{15}C and the Carbon target nuclei.

With the purpose to compare the obtained correlations with simulated data performed as explained in section 4.5, figure 5.7 shows the proton-neutron angular distributions with a proton target for the simulated data.

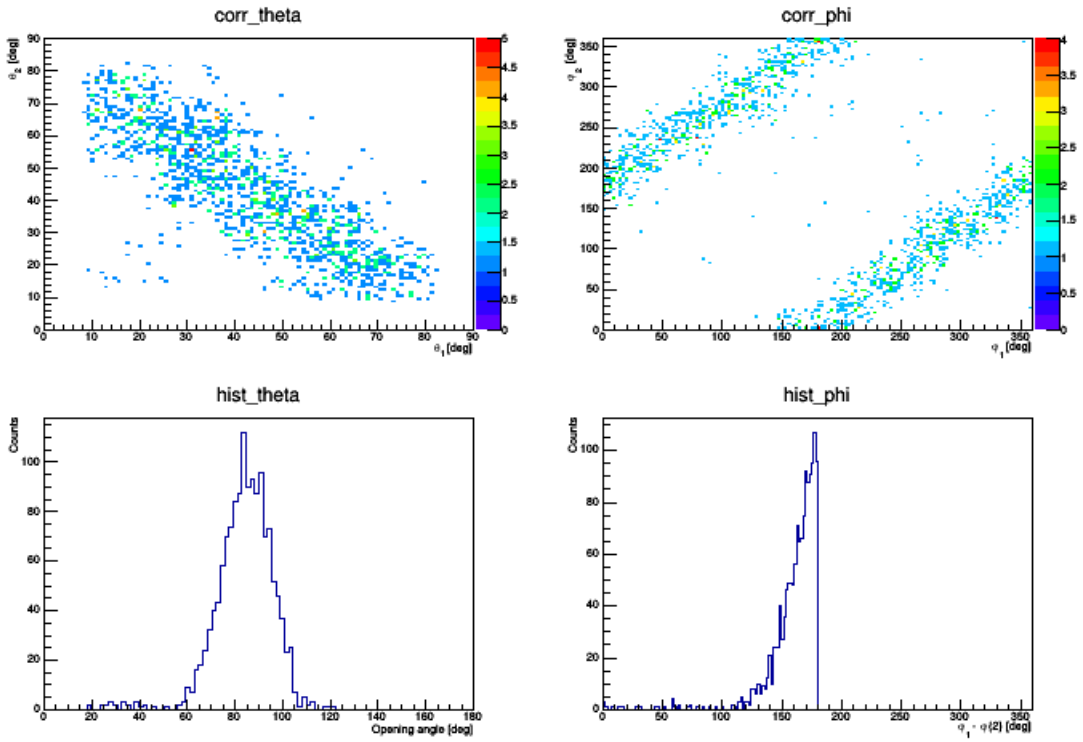

Figure 5.7: Simulated Proton-Neutron correlations for ^{15}C(p,pn) ^{14}C at QFS conditions measured with Crystal Ball. The Polar Correlation and Opening Angle is shown.

This result is interpreted as the expected (p,pn) kinematical correlation in QFS conditions [24, 60–62, 69, 70, 94]. As it is observable, the angular proton-neutron distributions of QFS reactions have a strong signature which consists in an angular difference on the polar coordinate (named "opening angle") peaking around 80° and an angular difference in the azimuthal coordinate peaking at 180°.

The experimental plots are comparable with the simulated ones reinforcing the expected behavior of the QFS kinematical conditions. It is possible to observe that the simulated distribution is still more narrow. This is understandable by the fact that in experimental plots are included the contributions of Carbon in the target. It is observable as well in experimental data, especially for the data obtained with the CH_2 target, a behavior which approximates to the QFS behaviour.

The obtained correlations for the two nucleons are shown in the upper panels of figure 5.7. From the left top plot it is possible to identify that the θ angles are distributed majority around 80° of opening angle. In the right side it is observable

a maximum peak around 180° for the φ angle. This means a co-planarity of the two nucleons. These two observations are seen as the main signatures of QFS regime.

5.4 Particle inclusive neutron knockout with Crystal Ball

In this section it will be presented the study of the inclusive neutron knockout of the ^{15}C(p,pn)^{14}C breakup reaction with a required signal in Crystal Ball but without a requirement of particles in the Crystal Ball. In opposition to the previous case where we had a multiplicity of two hadrons in Crystal Ball, now we can have events with multiplicity 0,1,2,3 and 4. Figure 5.8 shows the multiplicity of hadrons observed in Crystal Ball.

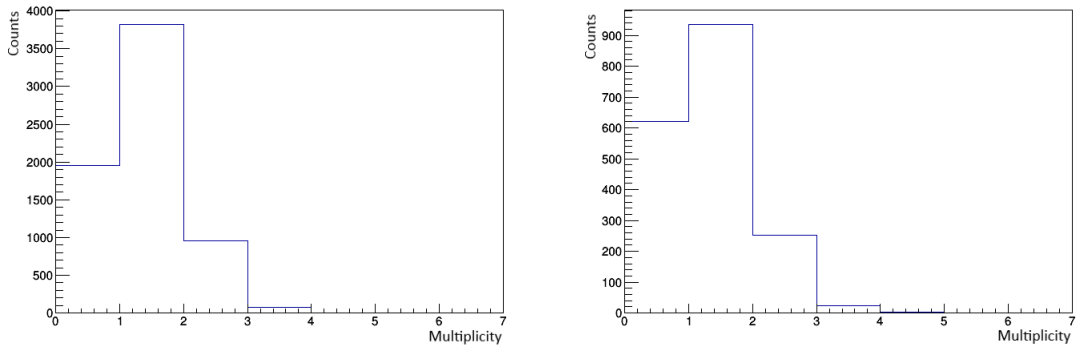

Figure 5.8: Hadrons multiplicity in Crystall Ball. On the the left is shown the multiplicity for the reaction with CH_2 target and on the right for the Carbon target.

No significant differences can be observed in the spectra, apart from a slight higher number of multiplicity 0 events when considering the Carbon target.

As the analysis of the emerging fragments is done using the trigger pattern TPAT8 the number of reacted fragments is not so reduced as in the first case of study (section 5.2) and it is possible to take conclusions which allows the comparison with this case. On the other side it is not possible to take a value for the detection efficiency and consequently it is not possible to extract a cross section.

5.4.1 Momentum distributions

The determination of the inclusive transverse momentum distribution for the ^{15}C(p,X)^{14}C breakup reaction depends on the number of incoming ^{15}C projectiles selected with the trigger pattern TPAT2, the number of reacted ^{14}C projectiles measured with the trigger pattern TPAT8 which means that a signal in Crystal Ball was required but in this case any conditions concerning the hadrons in Crystal Ball were included. The Crystal Ball efficiency to detect a proton and a neutron was not included and for this reason it is not possible to extract the total cross section (anyway we can take observations of the shape of the momentum distribution). The ^{15}C neutron breakup reaction was performed with a CH_2, a Carbon and an Empty target in order to subtract the background and the Carbon contribution in the reaction. The width and the shape of the transverse momentum distribution in the Y direction was calculated. Figure 5.9 shows the differential transverse momentum for the Y direction. The data has been normalized and corrected by the subtraction of the background.

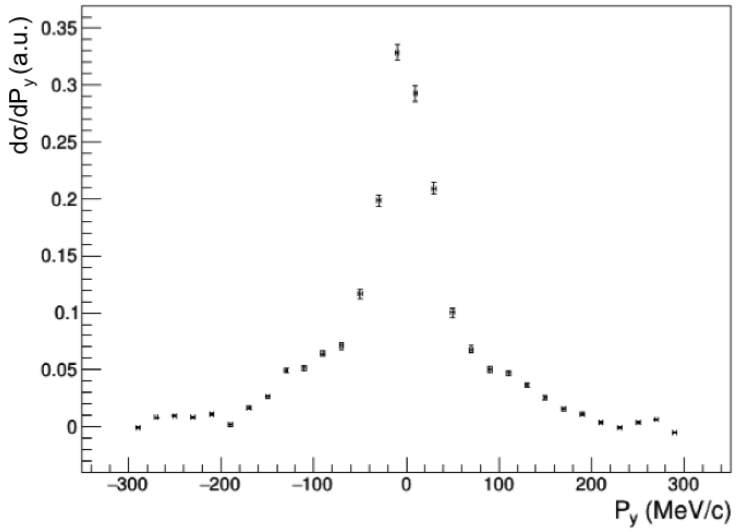

Figure 5.9: Inclusive transverse momentum distribution for the Y direction of ^{15}C neutron breakup reaction measured with TPAT8.

A Gaussian curve was adjusted to the experimental curve of the momentum in order to take the width. The shape and the width of this curve can be compared and transferred for the case of the inclusive knockout reaction without Crystal Ball.

5.5 Gamma analysis

After a nucleon removal, the reaction residues are often in excited states. If the excited state is below the nucleon separation energy, the nucleus is de-excited by emitting gamma radiation.

The gamma energy spectrum measured in coincidence with the fragment, can give information about the excitation of the ^{14}C core after the reaction. The ^{14}C isotope has the expected bound excited states of 6.09 MeV, 6.72 MeV, 6.90 MeV and 7.01 MeV. Figure 5.10 shows the expected excitation levels scheme.

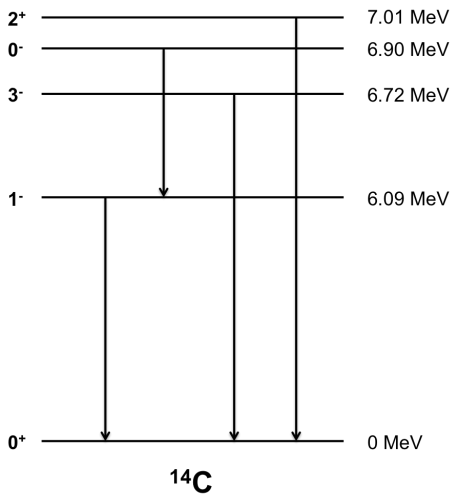

Figure 5.10: Gamma scheme for ^{14}C with the most probable observable levels.

In figure 5.11 is shown the decay gamma energy spectrum measured with Cristal Ball for the ^{15}C(p,pn)^{14}C breakup reaction which has been corrected by subtracting the background due to reaction on carbon. To reproduce the background it was simulated the gamma spectrum obtained for the proton and the neutron in the quasi-free conditions with the Chulkov code without any gamma. In order to obtain the relative population of the excited states to the ground state, simulations of the emission of the photon energies 808.8 keV, 6092.4 keV and 6726.5 keV were done using the R3Broot framework. A weighting analysis procedure was done considering the obtained simulated spectra for the background and emitted photons, and adjusted to the experimental data. The result from this procedure is presented in figure 5.11.

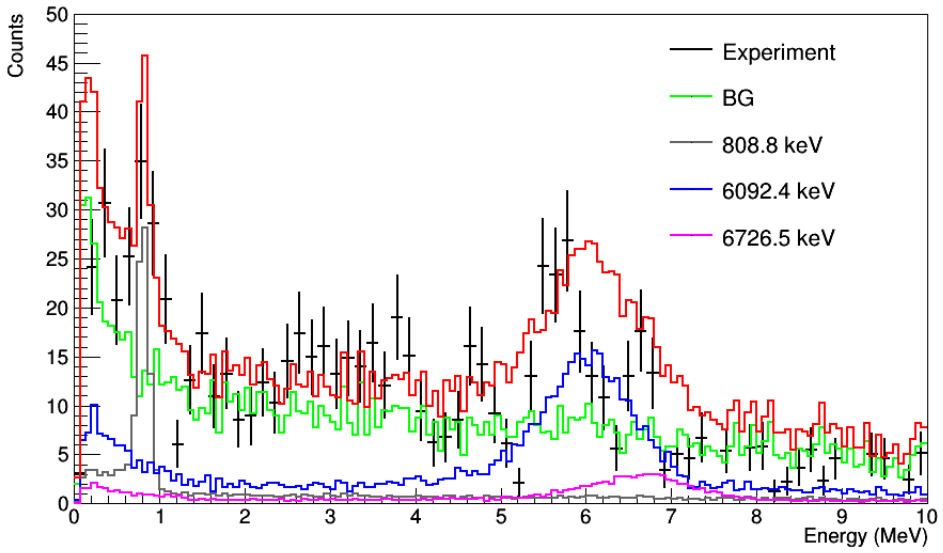

Figure 5.11: Gammas for Protons target.

5.5.1 Knockout of valence neutron or inner core neutron

By plotting the momentum distribution with a gate in the 6.09 MeV gamma (5.2 Mev - 6.5 MeV) in the Crystal Ball a wider distribution is shown in figure 5.12.

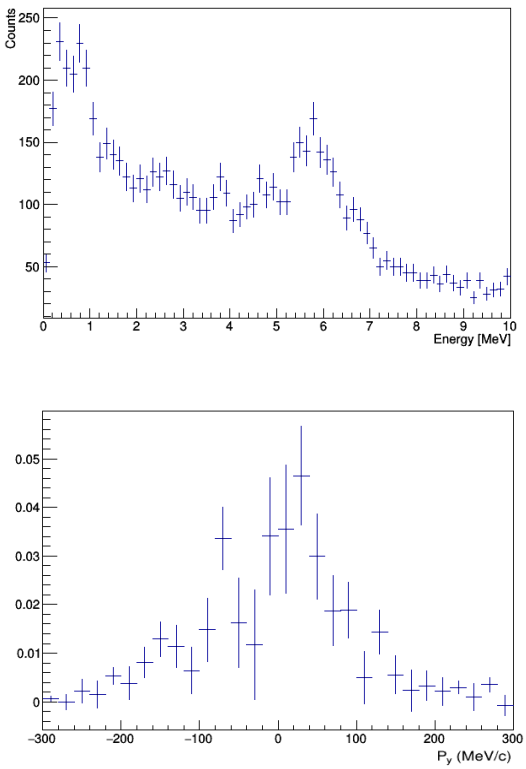

Figure 5.12: Transverse momentum distribution with a gate on the gamma of 6.09 MeV.

By adjusting the momentum with a Gaussian fit, a FWHM of 97.61 MeV/c was obtained, with a larger width than the momentum distribution gated without the gamma. As we will see in Chapter 6, this is compatible with the knockout of a neutron from a p-shell.

6

Theory Comparison

Contents

In this chapter it will be included the comparison of experimental results with the Faddeev/AGS calculations developed by R.Crespo, E.Cravo and A.Deltuva. In the first section the theoretical calculations are presented. Second and third sections are dedicated to the comparison of theoretical calculations for the particle exclusive neutron knockout and finally to the particle inclusive neutron knockout. The extracted normalization factors are presented in this chapter.

6.1 Faddeev/AGS theoretical calculations

Considering the reaction under study, the ^{15}C(p,pn)^{14}C knockout reaction in inverse kinematics and the ^{15}C ground state configuration, it is expected that the knocked out neutron be removed from the valence shell, i.e. the halo neutron, or it will be removed from an inner shell, i.e. from the ^{14}C core. Figure 6.1 shows a schematic representation of these two contributions in the considered reaction mechanism. In the top the valence neutron from the ^{15}C nucleus is removed. After the reaction the fragment (^{14}C core) remains in the ground state. In the bottom a inner neutron is removed and the ^{14}C fragment stays in an excited state.

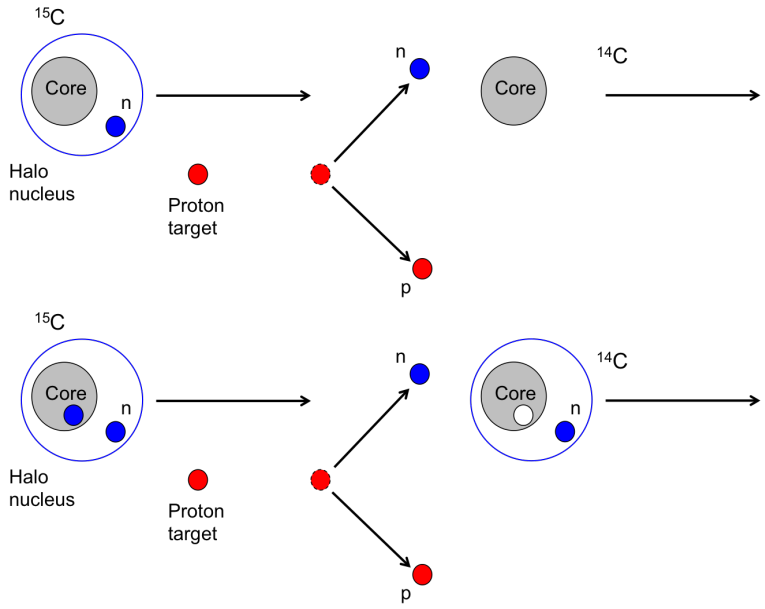

Figure 6.1: Scheme of ^{15}C(p,pn)^{14}C reaction mechanism. In the top the valence neutron is removed from the ^{15}C nucleus. In the bottom an inner neutron is removed.

The experimental data will be compared with observables calculated using the Faddeev/AGS reaction framework [33, 38, 102]. As mentioned (in section 1.4) this formalism is a non-relativistic three-body multiple scattering framework that treats equally all opening channels and can be applied to the study of nuclear reactions allowing the extraction of reliable structure information.

Calculations based on this formalism have been performed for the neutron removal reaction at the same energies as the experimental data, considering the neutron knockout from the inner shell 1p leading in a simplified picture to the excited 1^- and 0^- state of ^{14}C further, the valence neutron knockout from the 2s shell leading to the ^{14}C in the ground state.

As mentioned before, the momentum distribution of the fragment is directly related to the momentum distribution of the knocked out neutron, furthermore the shape of the distribution reflects its orbital momentum. Typically a s-shell presents a narrow momentum distribution and a p-shell a broad shape.

Figure 6.2 shows the Faddeev/AGS theoretical calculations for the core ^{14}C. The transverse momentum distributions regarding the neutron knocked out from the s-shell and removed from a p-shell, are both normalized to the unit.

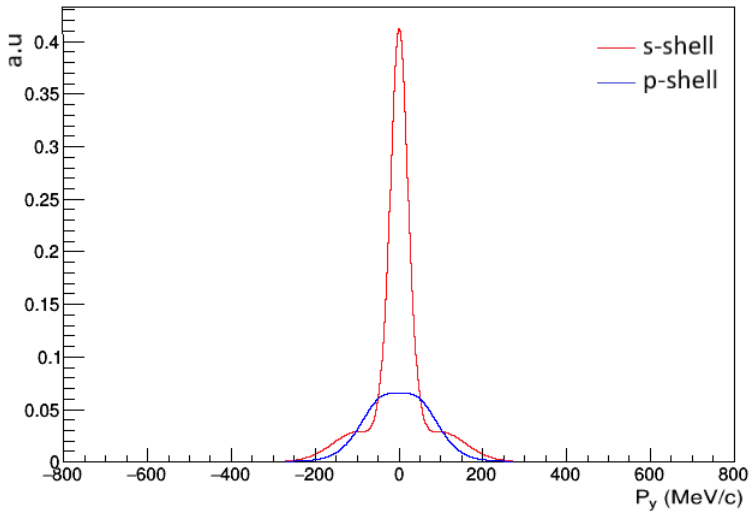

Figure 6.2: Theoretical transverse momentum distribution for the ^{15}C(p,pn)^{14}C reactopn calculated with the Faddeev/AGS formalism. The narrow one stands for a neutron removed from a s-shell and in the broad to the neutron removed form a p-shell.

Integrated cross sections contributions for the s-shell and the p-shell are presented in the table 6.1:

	$\sigma_{Theo.}$**(mb)**
Valence	30.9
Inner	13.7

Table 6.1: Cross sections calculated using the Faddeev/AGS formalism for the single particle cross sections for the different contributions.

In order to reproduce the total momentum distribution obtained from the experimental data, it is necessary to adjust the weights of the theoretical curves of (s and p-shells) valence and inner core contributions according to the equation equation 6.1:

$$\sigma_{total}^{theo} = a.\sigma_{valence} + b.\sigma_{inner} \tag{6.1}$$

where a and b are normalization factors which gives the respective weights of valence and inner contributions in the total cross section.

The next two sections are dedicated to present and discuss the exclusive and inclusive neutron knockout.

6.2 Particle exclusive neutron knockout

In order to compare the theoretical and experimental results, the total theoretical cross section given by the eq. 6.1 was scaled to the total cross section obtained with experimental data (35.3 mbarn). By fitting the theoretical total transverse momentum distribution to the experimental exclusive transverse momentum distribution, the normalization factors a and b (table 6.2) were obtained.

	Normalization factor
***a* (Valence)**	0.56
***b* (Inner)**	1.31

Table 6.2: Normalization factors obtained for the particle exclusive neutron knockout

By applying the a and b normalization factors to the valence and inner contribution in core distributions, the total theoretical momentum differential cross section distribution was obtained, which is shown in figure 6.3.

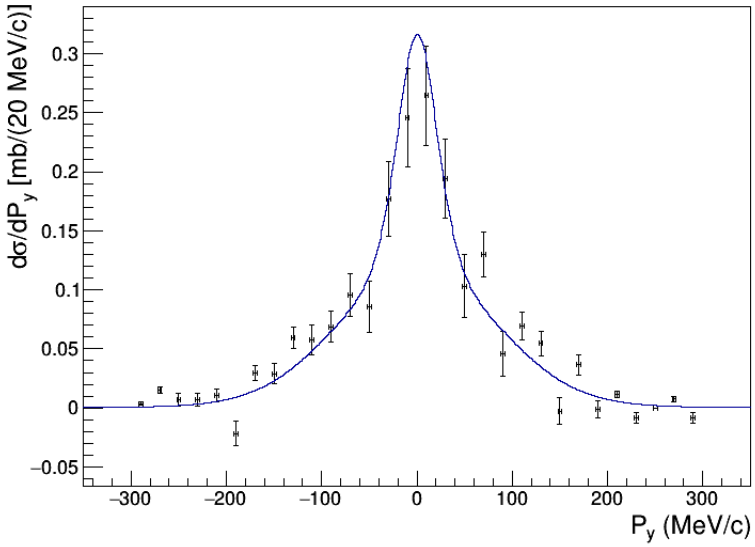

Figure 6.3: Comparison of Faddeev/AGS theoretical curve with the 0.56 and 1.31 reduction factors at blue with the experimental plot for the ^{15}C(p,pn)^{14}C exclusive breakup reaction.

The total theoretical distribution in blue presents a good agreement with experimental data. Considering total cross sections for the s-shell and p-shell moreover the normalization factors we can say that inner neutrons from the p-shell contribute 51 % to the total cross section and valence neutrons from the s-shell orbital 49 %. Summary of these contributions is summarized in Table 6.3.

	$\sigma_{Theo.}$**(mb)**	**Norm. Factor**	**Weight(%)**
s-shell	30.9	0.56	49
p-shell	13.7	1.31	51

Table 6.3: Summary of s and p shells contribution to total cross section.

6.3 Particle inclusive neutron knockout

The comparison of theoretical calculation with inclusive experimental data only is possible considering the approach explained in section 5.4 i.e. with a required signal in Crystal Ball but without any requirement of particles in the Crystal Ball. The transverse momentum distribution presents a well defined shape, however, it is not possible to take a value for the cross section.

The approach where TPAT2 (section 5.2) was used doesn't allowed conclusions on the shape of momentum distribution and consequently it is not possible to adjust the theoretical distribution to the experimental one.

Figure 6.4 shows the theoretical total transverse momentum distribution adjusted to the experimental data with the same normalization factors ***a*** and ***b*** which were used in the previous section.

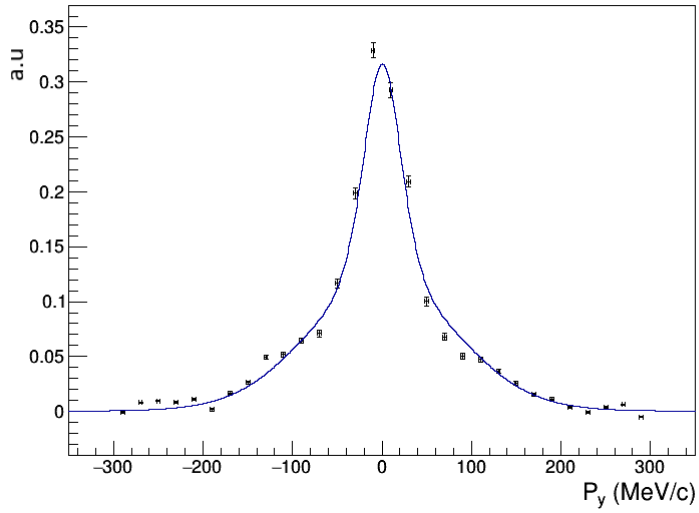

Figure 6.4: Comparison of Faddeev theoretical curve with the 0.56 and 1.31 reduction factors at blue and the experimental plot for the ^{15}C(p,pn)^{14}C inclusive breakup reaction with a signal in Crystal Ball.

The total theoretical transverse moment agrees very well with the experimental data. This indicates that the weight of both contributions (valence and inner core knockout) does not depend on the way the reaction taggins is done. However, it remains unclear if the discrepancy observed in the integrated cross section is related to a different weight in the knockout contributions.

7

Conclusions and Outlook

The studies presented in the current thesis are composed by the investigation of the ^{15}C halo nucleus through neutron knockout reactions at relativistic energies.

The main part of the work consisted in the calibration of some detector systems and in the analysis of experimental data obtained during the S393 experimental campaign, which took place at the R^{3}B setup at the GSI laboratory in Darmstadt. There, a primary beam of ^{40}Ar (490 MeV/u) was guided towards a Be production primary target at the entrance of the FRS. Fragments resulting from the nuclear fragmentation were delivered to the experimental hall according to their magnetic rigidity. Once in the experimental hall, the secondary beam (cocktail of isotopes) was characterized by its time-of-flight and energy loss before the target. Around the target the angles of incoming projectiles and fragments were measured by the SST detectors. Crystal Ball was used in a hybrid mode for the detection of γ-rays and simultaneously the characterization of proton-neutron angular correlations. Reaction products after the target were separated by the ALADIN magnet dipole in three different branches (neutrons, heavy fragments and protons). Heavy fragments were characterized by their trajectory, time-of-flight and energy loss.

Considering the analysis of the data, the incoming beam projectiles and outgoing reactions fragments were unambiguously identified. A tracking mass resolution of 1.42 % and 1.37 % was respectively achieved for fragments with A=14 and A=15. After tagging the reaction channel the analysis was distinguished in two different processes were three different methodologies were used:

- *Particle inclusive neutron knockout*, where the final state of the fragment was not distinguished. Two different methodologies were used in this approach:

  - (i) heavy fragments were detected without the inclusion of Crystal Ball in the analysis.

  - (ii) analysis requiring a signal in Crystal Ball detector. However, no hadronic signals were required in this case.

- (iii) *Particle exclusive neutron knockout*, where the heavy fragments and the emerging nucleons (proton-neutron) were detected by Crystal Ball.

In all three methodologies, the experimental data obtained with a Carbon target was used to eliminate possible reactions leading to the same final state originated by Carbon nuclei or in other parts of the experimental setup (considered as background) from the CH_2 experimental data.

In the first methodology (i) transverse momentum distributions were determined and cross sections calculated for CH_2 and Carbon targets. A width (FWHM) of (43±23) MeV/c was determined for the CH_2 target. A inclusive differential cross section of (72±19) mbarn for the ^{15}C(p,X)^{14}C reaction was extracted. Due to the low statistic obtained in this analysis approach, significantly fluctuations were observed after the Carbon contribution was subtracted, resulting in large uncertainties determined.

For the methodology (ii) a significant increase of data was obtained with the inclusion of a different trigger pattern. Transverse momentum distributions were achieved, however due to the difficulty in determining the detection efficiency for the Crystal Ball system under the considered conditions, the reaction cross section could not be determined.

In the exclusive approach (iii) transverse momentum distribution widths of (43±10) MeV/c and (35±10) MeV/c were obtained respectively for CH_2 and Carbon targets. The extraction of total cross sections implied the determination of Crystal Ball efficiency to detect a proton and a neutron in coincidence. Using Montecarlo simulations an efficiency of (15.25±0.87)% was determined, using the standard and Bertini physics lists. A total exclusive cross section of (35±4) mbarn for the ^{15}C(p,pn)^{14}C knockout reaction was extracted. In this approach the proton and neutron which emerged from the reaction were detected in Crystal Ball. The proton-neutron angular correlations from the ^{15}C(p,pn)^{14}C reaction exhibited opening angles on the polar coordinate θ around 80° and around 180° for the difference in the azimuthal coordinate φ. This indicates the strong QFS behavior in this reaction, in opposition to the correlations obtained with the Carbon target reactions.

A summary of measured FWHM for the transverse momentum distributions obtained in this work is presented in table 7.1, together with the longitudinal momentum distributions obtained in other two reference works.

Momentum distributions

Target	**Energy (MeV/u)**	**Reference**	**FWHM (MeV/c)**	
			Inclusive	Exclusive
CH_2	420	This work	43 ± 23	43 ± 10
C	420	This work	-	35 ± 10
C	62	[53]	63.5 ± 0.7	
Be	85	[47]	67 ± 3	

Table 7.1: Resume table with FWHM for the momentum distributions obtained in this work and the ones referenced in the literature.

Table 7.2 presents a summary of measured cross sections in this work and the ones reported in other works.

Cross Sections

Target	**Energy (MeV/u)**	**Reference**	σ **(mb)**	
			Inclusive	Exclusive
Proton	420	This work	72 ± 19	35 ± 4
C	420	This work	225 ± 14	101 ± 3
C	62	[53]	159 ± 15	
Be	85	[47]	33 ± 3	

Table 7.2: Resume table with total cross sections obtained in this work and the ones referenced in the literature.

Experimental results were compared with the Faddeev/AGS reaction formalism calculations. Normalization factors were determined and theoretical transverse momentum distributions reproduced the experimental ones. By this comparison it was evaluated the contribution of inner neutrons from p-shell in the reaction mechanism. This was expected as at these relativistic energies deeper regions inside the nucleus can be investigated.

The γ-spectrum associated to the considered reaction channel also studied and it was observed that the core fragments presented a larger momentum distribution

when gated in coincidence to events related to γ from bound excited states of negative parity in ^{14}C, reinforcing the idea of two components (s-shell and p-shell) in the determined momentum distributions.

The use of proton targets to characterize the neutron knockout in exotic nuclei like halo systems is an ideal tool to benchmark nuclear reaction models. The results of this work indicate the capabilities to access various shells in the knockout process, and should motivate the execution of additional experiments using the future setup of the R^{3}B collaboration at the FAIR facility.

8

Synopsis

Contents

8.1 Introduction

The ^{15}C is a one neutron-halo nucleus with a separation energy of S_n = 1.218 MeV. Ground state and spectroscopic information have been extracted experimentally from Coulomb dissociation studies [46] resulting in a consistent picture with a dominant (^{14}C(0^+) x $2s_{1/2}$) configuration. Momentum distributions of the core extracted from single neutron knockout reactions [47] exhibited a broader width of 67 MeV/c, consistent with larger separation energy and the same dominant configuration.

The Faddeev/AGS formalism is a non-relativistic three-body multiple scattering framework that treats equally all opening channels (elastic, breakup and transfer) and can be applied to the study of reactions and allows the extraction of reliable structure information.

In this work it is presented the study of the ^{15}C(p,pn)^{14}C knockout reaction at relativistic energies, performed at the R^{3}B setup at the the GSI laboratory. The momentum distributions and the total cross sections for the ^{15}C(p,pn)^{14}C particle inclusive neutron knockout reaction and particle exclusive neutron knockout reaction will be presented. These results are compared with the Faddeev/AGS theoretical calculations.

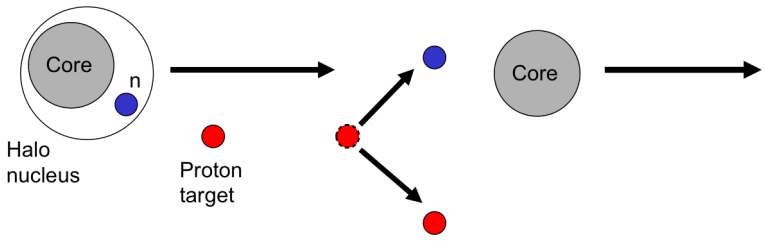

Figure 8.1: Representation of ^{15}C(p,pn)^{14}C QFS reaction.

8.2 Experimental setup

The S393 experiment was performed in August 2010 at the R^{3}B setup at the the GSI laboratory (ref). Several exotic nuclei, covering (4 < Z < 10) and (1, 5 < A/Z < 3) were investigated by means of different reactions on various targets using

the same experimental setup.

The beam of exotic nuclei was produced by the In-Flight Separation method. The ^{40}Ar primary beam was accelerated at 490 MeV/u and guided towards a 4 g/cm^2 Be production target, where secondary beams were produced via nuclear fragmentation. The outgoing nuclei were selected by means of magnetic fields in the FRS and guided to the experimental setup at cave C with approximately 420 MeV/u.

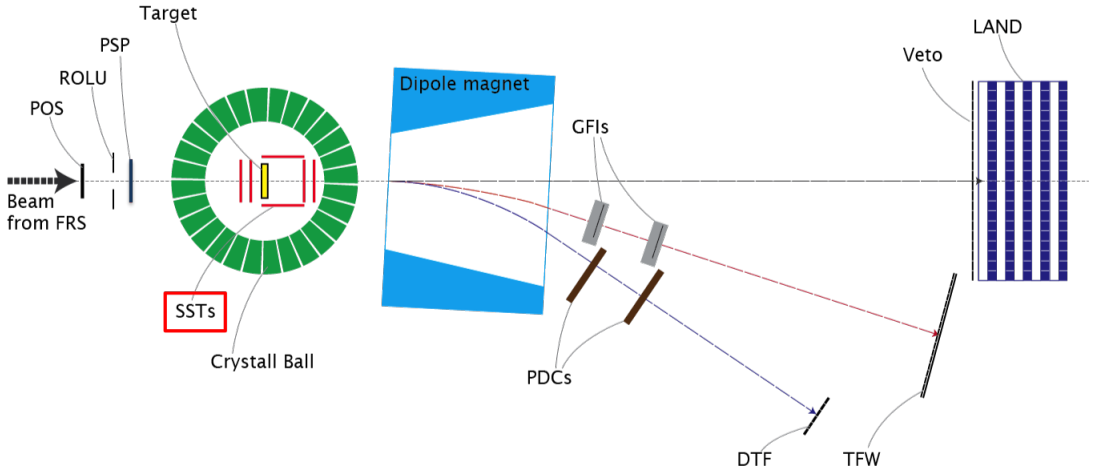

Figure 8.2: Schematic view of the LAND-R^{3}B setup in the cave C of GSI.

This setup, shown in Figure 8.2 is based on the event-by-event and exclusive measurement of all initial and final particle states covering the complete reaction kinematics.

The secondary beam coming from the FRS is characterized by measuring its time-of-flight and energy loss before reaching the target. Figure 8.3 shows the identification plot for the incident ions coming from setting 3 of FRS, centered in A/Z=2.5. The isotope of interest for our reaction ^{15}C with Z=6 and A/Z=2.5 is identified inside the ellipse.

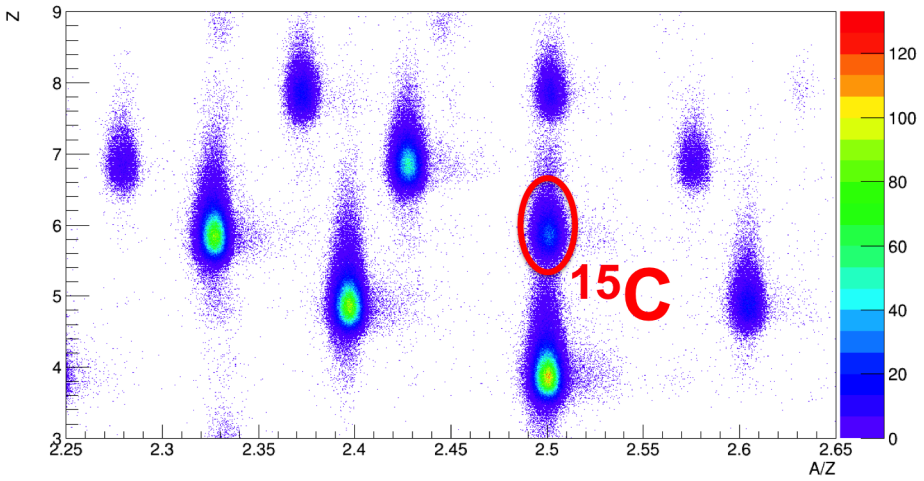

Figure 8.3: Incoming identification plot for the nuclei reaching the target. The charge of the nuclei is plotted against their mass over charge ratio.

The target area is covered by a box of eight silicon-strip detectors for charged fragments detection and a 4π-NaI detector for gammas and protons (the so-called Crystal Ball). After the target the reaction products are separated by the ALADIN magnet into three branches: neutrons measured by the LAND detector, heavy ions measured by the TFW and GFIs detector systems, and protons measured with DFT and PDCs detectors.

8.3 Results

The results are presented for two different processes:

- **Particle inclusive neutron knockout**, where only the heavy fragment is detected. In this case, the process was study with two different methods. First analysing the data without requiring any signal in Crystal Ball and than by analysing the data with a signal in Crystal Ball but without any particle condition in this detector.

- **Particle exclusive neutron knockout**, where the heavy fragments and the emerging nucleons (proton-neutron) are detected by Crystal ball.

8.3.1 Particle inclusive neutron knockout

Transverse momentum distributions were determined and cross sections calculated for CH_2 and Carbon targets. A FWHM of (44±2) MeV/c was determined for the CH_2 target. A inclusive differential cross section of (72±19) mbarn for the $^{15}C(p,X)^{14}C$ reaction was extracted. Due to the low statistic obtained in this analysis approach, significantly fluctuations were observed after the Carbon contribution was subtracted, resulting in large uncertainties determined.

Figure 8.4 shows the differential transverse momentum for the Y direction. The data was normalized and corrected by the subtraction of carbon and background contributions. The differential cross section of $^{15}C(p,X)^{14}C$ breakup reaction on a protons target was determined by integration of the distribution.

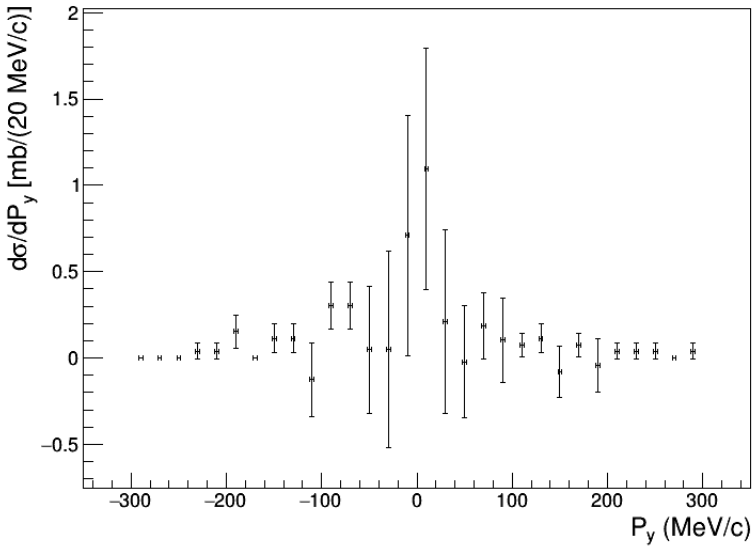

Figure 8.4: Inclusive transverse momentum distribution of $^{15}C(p,X)^{14}C$ breakup reaction.

Table 8.1 shows the inclusive cross sections and the respective uncertainties for the neutron breakup reaction on a CH_2, Carbon and as well on the reconstructed protons targets.

Target	Cross Section(mb)
CH_2	369 ± 12
Carbon	225 ± 14
Proton	72 ± 19

Table 8.1: Resume table for the inclusive cross sections and the respective uncertainties for CH_2, Carbon targets. Finally the calculated values for the reaction with protons.

Using the same Particle inclusive neutron knockout, but now requiring a signal in Crystal Ball detector however, no hadronic signals requirement, a significant increase of data was obtained with the inclusion of a different trigger pattern. Transverse momentum distributions were achieved, however due to the difficulty in determining the detection efficiency for the Crystal Ball system under the considered conditions, the reaction cross section could not be determined. Figure 8.5 shows the differential transverse momentum for the Y direction.

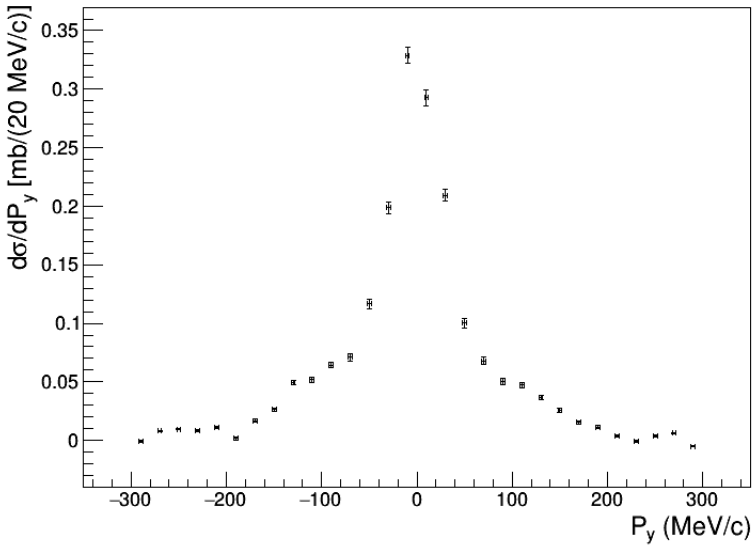

Figure 8.5: Inclusive transverse momentum distribution for the Y direction of ^{15}C neutron breakup reaction measured with TPAT8.

8.3.2 Particle Exclusive Neutron Knockout

In the particle exclusive approach transverse momentum distribution widths of (43±10) MeV/c and (35±10) MeV/c were obtained respectively for CH_2 and Carbon targets.

The extraction of total cross sections implied the determination of Crystal Ball efficiency to detect a proton and a neutron in coincidence. Using Montecarlo simulations an efficiency of (15.25±0.87)% was determined, using the *standard* and *Bertini physics lists*.

Table 8.2 shows the results for the exclusive cross sections and the respective uncertainties for the ^{15}C neutron breakup on CH_2, Carbon and proton targets.

Target	**Cross Section(mb)**
CH_2	172 ± 3
Carbon	101 ± 3
Proton	35 ± 4

Table 8.2: Resume table for the exclusive cross sections and the respective uncertainties on CH_2, Carbon and reconstructed protons target.

In this approach the proton and neutron which emerged from the reaction were detected in Crystal Ball. The proton-neutron angular correlations (figure 8.6) from the ^{15}C(p,pn)^{14}C reaction exhibited opening angles on the polar coordinate θ around 80° and around 180° for the difference in the azimuthal coordinate φ. This indicates the strong QFS behavior in this reaction, in opposition to the correlations obtained with the Carbon target reactions.

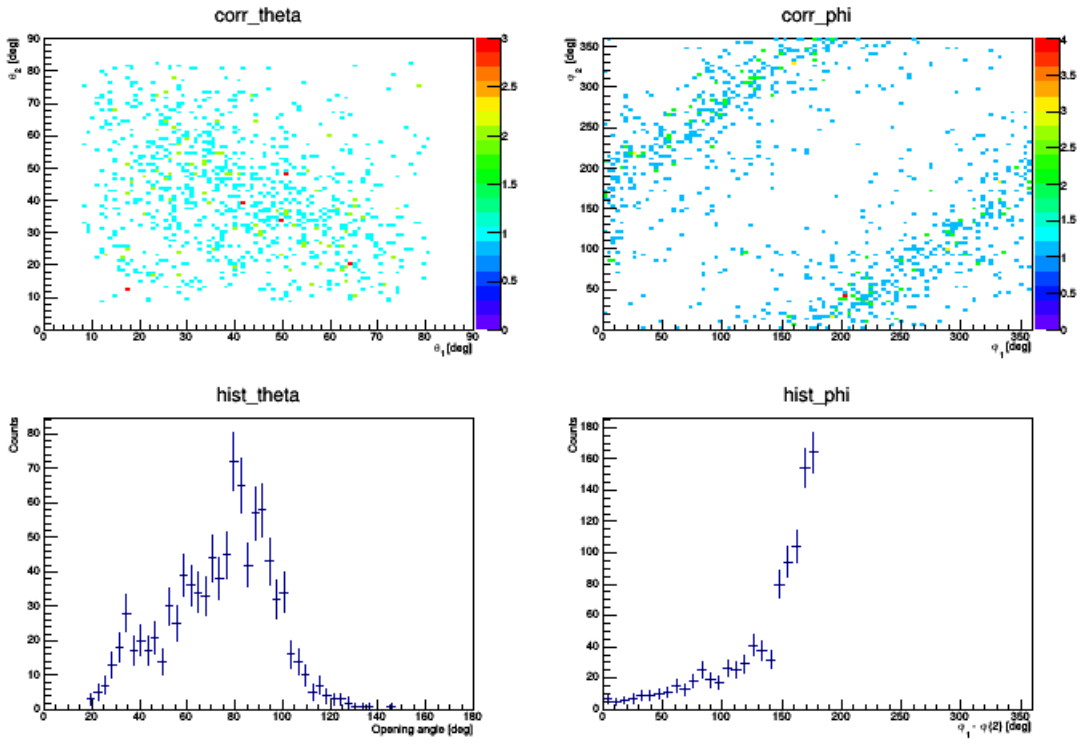

Figure 8.6: Proton-Neutron angular correlations for a breakup reaction with a CH_2 target at at approximately 500 MeV/u.

8.4 Faddeev/AGS theoretical calculations

Considering the reaction under study, the ^{15}C(p,pn)^{14}C knockout reaction in inverse kinematics and the ^{15}C ground state configuration, it is expected that the knocked out neutron be removed from the valence shell or from an inner shell. Figure 8.7 shows schematic representation of the two possible reaction mechanism of ^{15}C(p,pn)^{14}C under quasi-free conditions. The knocked out neutron can be from the valence shell or the inner shell.

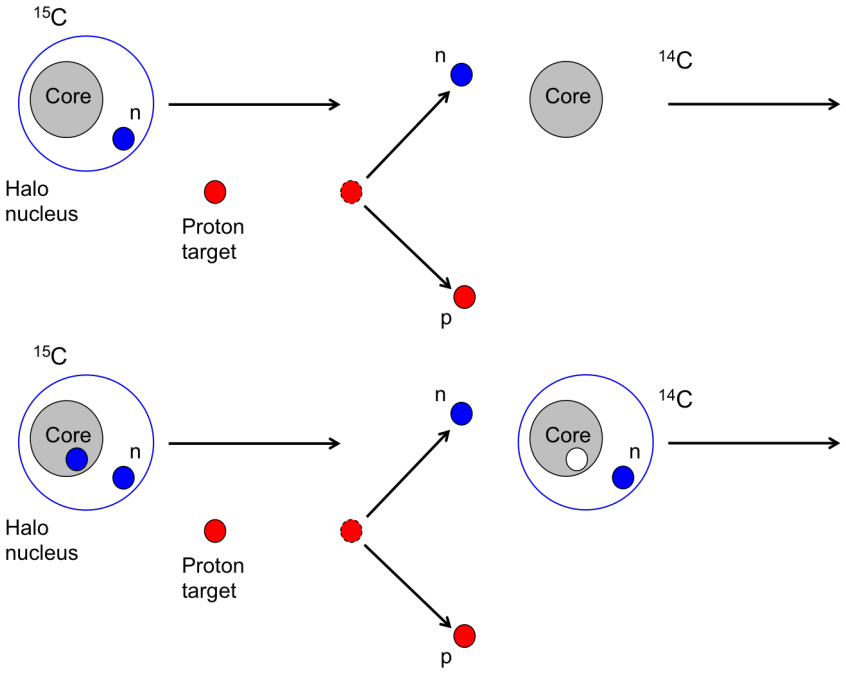

Figure 8.7: Scheme of ^{15}C(p,pn)^{14}C neutron knockout reaction at relativistic energies. In the top the valence neutron is removed from the ^{15}C nucleus. Bottom the scheme shows a removed inner neutron.

The experimental was compared with observables calculated using the Faddeev/AGS reaction framework. The calculated theoretical curves of momentum distribution for a neutron knocked out from the s-shell and removed from a p-shell is shown in Figure 8.8.

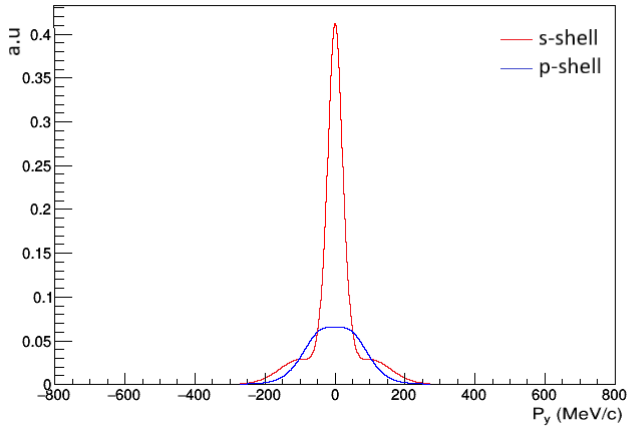

Figure 8.8: Theoretical curves of momentum distribution for the ^{15}C(p,pn)^{14}C calculated with the Faddeev/AGS formalism. In red for a neutron removed from a s-shell and in blue from a neutron removed form a p-shell.

By fitting the theoretical total transverse momentum distribution to the experimental exclusive transverse momentum distribution, the normalization factors a and b (table 8.3) were obtained.

	Normalization factor
***a* (Valence)**	0.56
***b* (Inner)**	1.31

Table 8.3: Normalization factors obtained for the particle exclusive neutron knockout

By applying the a and b normalization factors to the valence and inner contribution in core distributions, the total theoretical momentum differential cross section distribution was obtained, which is shown in figure 8.9.

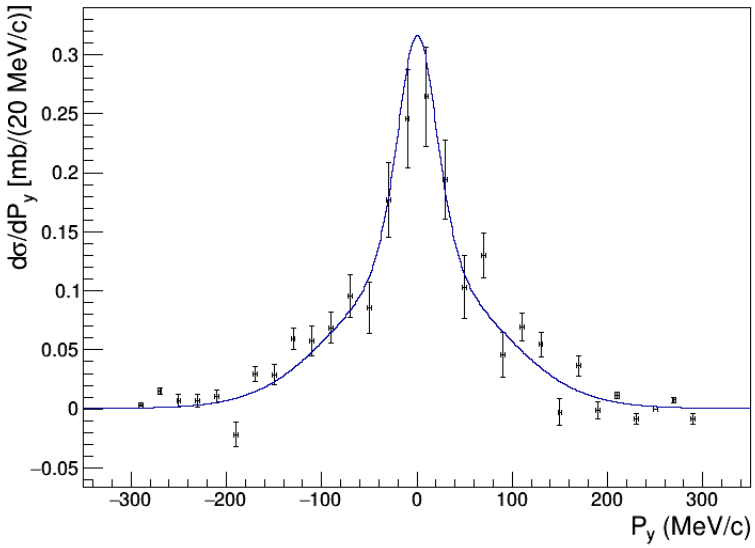

Figure 8.9: Comparison of Faddeev/AGS theoretical curve with the 0.56 and 1.31 reduction factors at blue with the experimental plot for the ^{15}C(p,pn)^{14}C exclusive breakup reaction.

Table 8.4 summarize the obtained information in the comparison.

	$\sigma_{Theo.}$**(mb)**	**Norm. Factor**	**Weight(%)**
s-shell	30.9	0.56	49
p-shell	13.7	1.31	51

Table 8.4: Summary of s and p shells contribution to total cross section.

In figure 8.10 the theoretical curves were adjusted to the experimental data obtained to the inclusive breakup reaction with a signal in Crystal Ball.

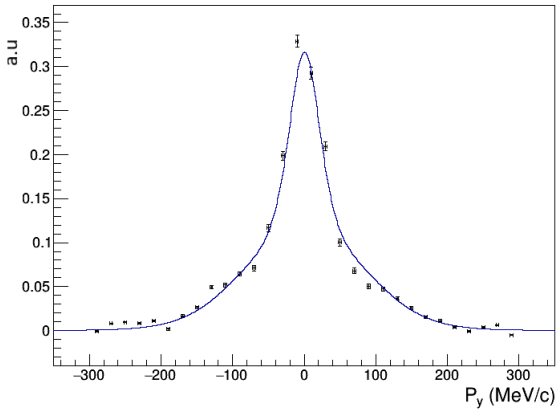

Figure 8.10: Comparison of Faddeev theoretical curve with the at blue with the experimental plot for the ^{15}C(p,pn)^{14}C inclusive breakup reaction with a signal in Crystal Ball.

8.5 Gamma analysis

By analysing the gamma energy spectrum measured in coincidence with the fragment, its can give information about the excitation of the ^{14}C core after the reaction. Figure 8.11 shows excitation levels scheme and the gamma spectra.

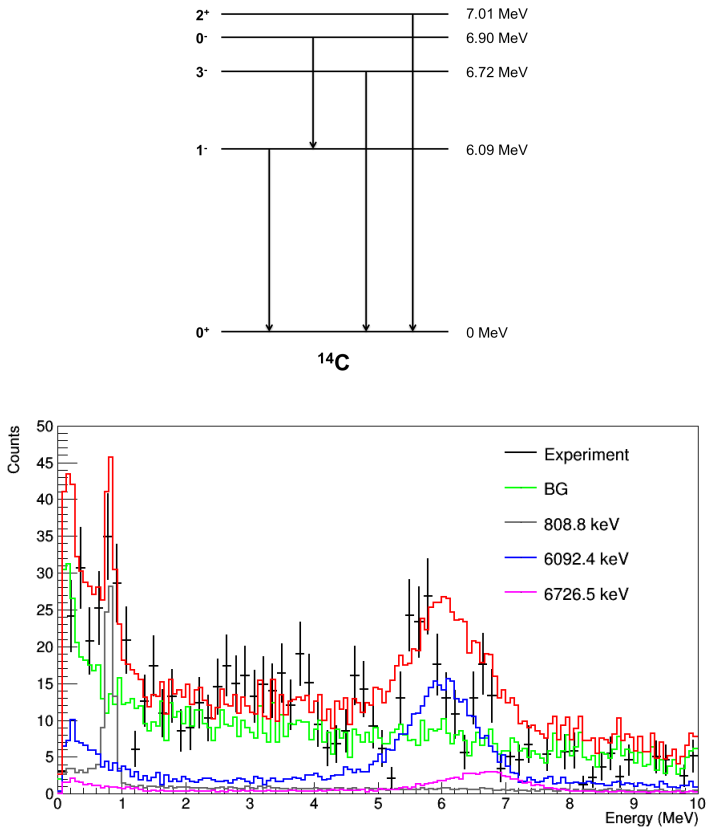

Figure 8.11: Gamma scheme for ^{14}C with the most probable observable levels.

The decay gamma energy spectrum measured with Cristal Ball for the ^{15}C(p,pn)^{14}C breakup reaction which has been corrected by subtracting the background due to reaction on carbon is shown in the bottom of the figure. To reproduce the background it was simulated the gamma spectrum obtained for the proton and the neutron in the quasi-free conditions with the Chulkov code without any gamma. In order to obtain the relative population of the excited states to the ground state simulated spectra for 808.8 KeV, 6092.4 keV and 6726.5 keV were obtained. The simulated spectra for the background and both states have been fitted to the experimental one.

By plotting the momentum distribution with a gate in the 6.09 MeV gamma (5.2 Mev - 6.5 MeV) in the Crystal Ball the wider distribution obtained, is shown in Figure 8.12.

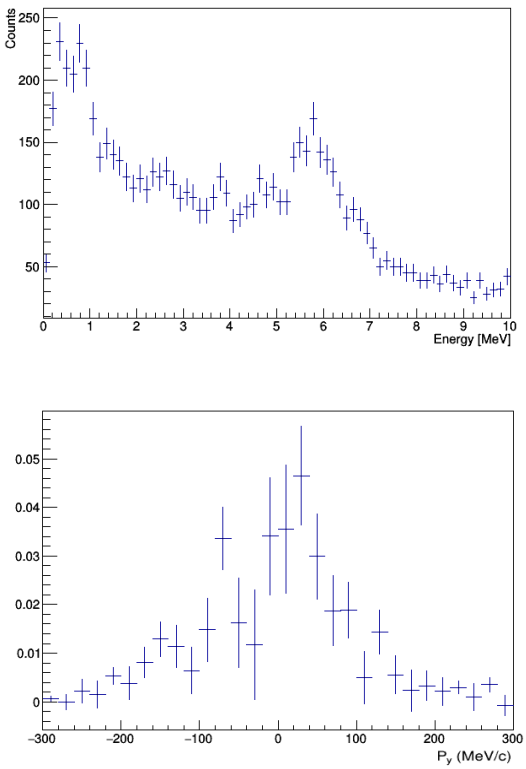

Figure 8.12: Transverse momentum distribution with a gate on the gamma of 6.09 MeV.

By adjusting the momentum with a Gaussian fit, a FWHM of 97.61 MeV/c was obtained, with a larger width than the momentum distribution gated without the gamma. This is compatible with the knockout of a neutron from a p-shell.

A

Study of an aperture cut on the cross section

The cross section calculation strongly relies on the number of detected fragments and projectiles. In order to gate the correct fragment mass we selected events from a bi-dimensional elliptical cut on the TFW energy versus the fragment mass. A study of stability for differential momentum distributions was performed. This study was made considering variations of 0.2 sigma in the elliptical cut on the CH_2 and Carbon runs.

Figure A.1 shows the performed study applied to the inclusive differential cross section, considering variations of 0.2 sigma in the elliptical cut. Figure A.2 shows the same performed study for the exclusive differential cross section.

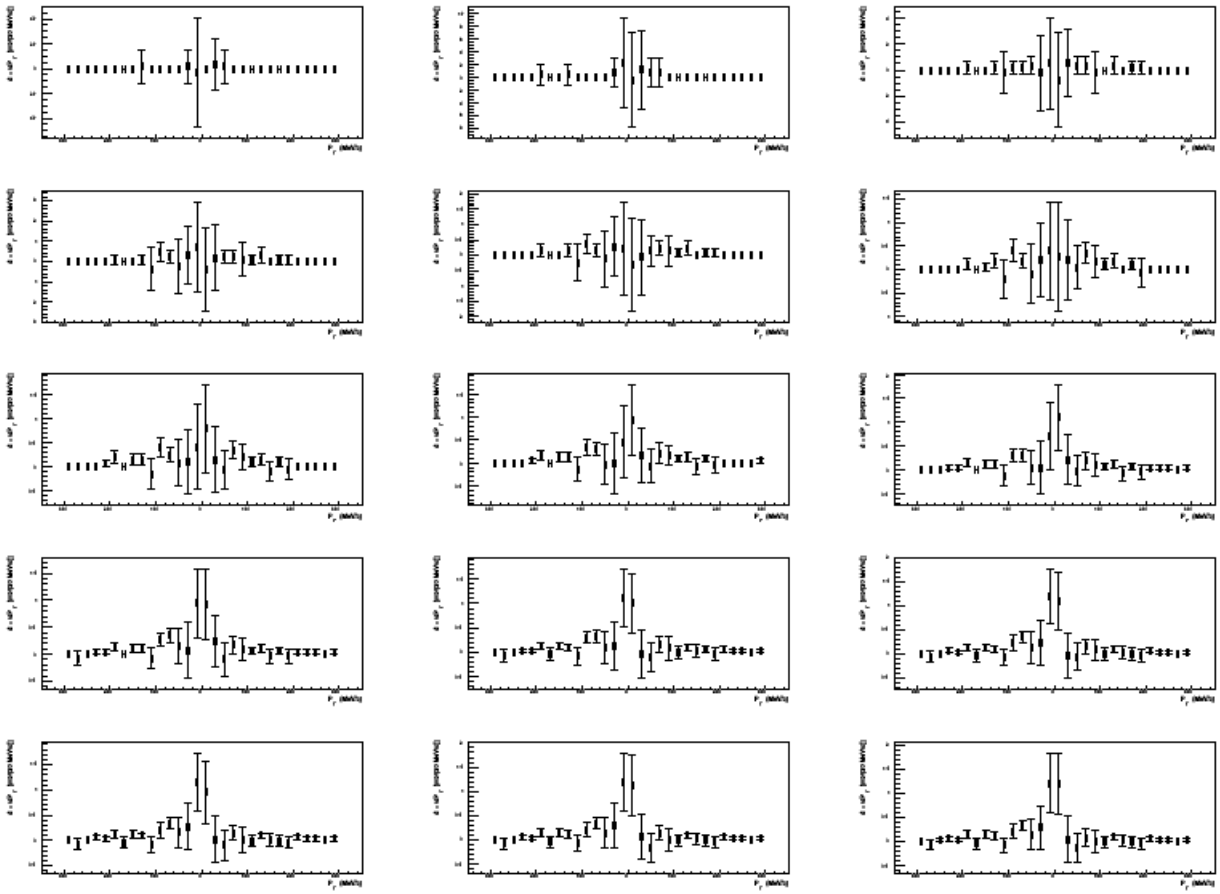

Figure A.1: Aperture cut study for the inclusive differential cross section

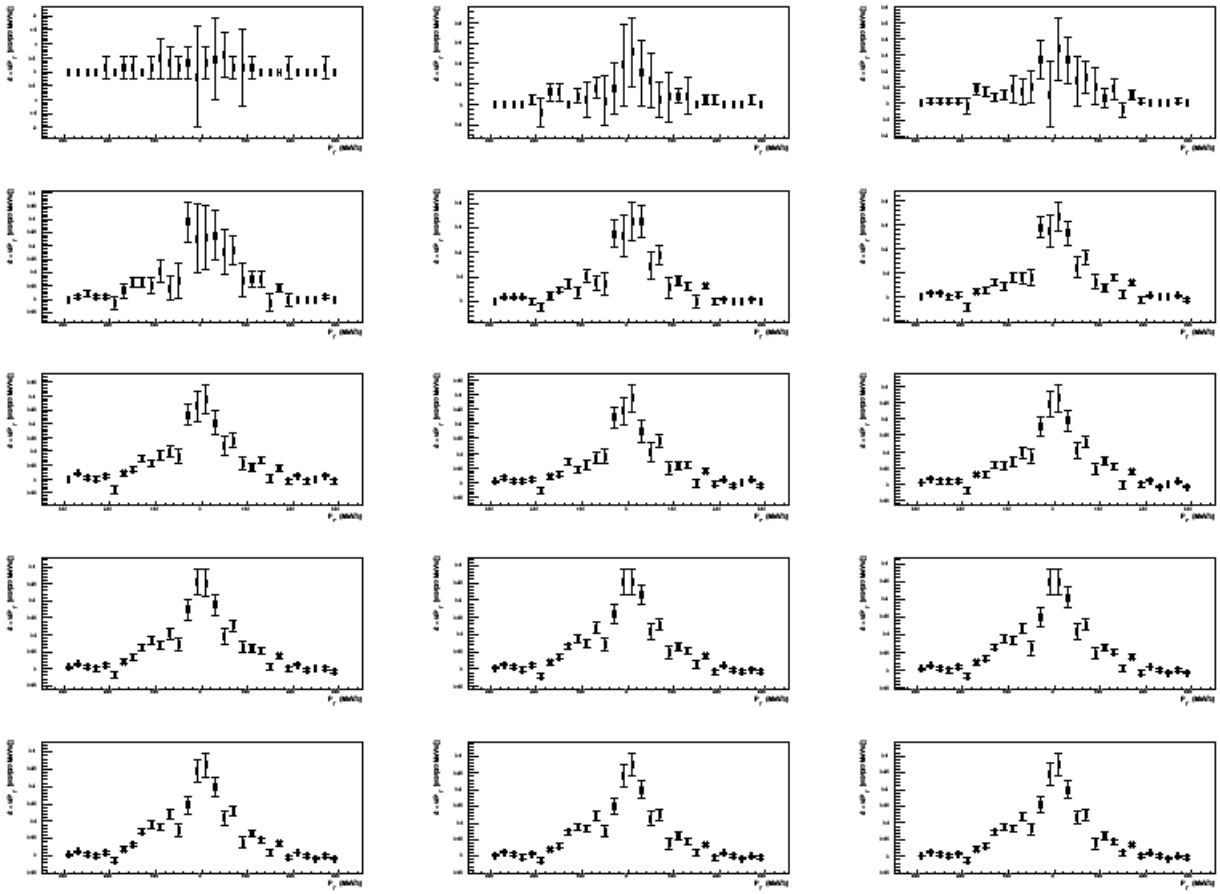

Figure A.2: Aperture cut study for the exclusive differential cross section

Bibliography

[1] E. Rutherford, "The scattering of alpha and beta particles by matter and the structure of the atom," *Philosophical Magazine*, vol. 21, pp. 669–688, 1911.

[2] J. Chadwick, "Possible existence of a neutron," *Nature*, vol. 129(3252), p. 312, 1932.

[3] "http://www.nndc.bnl.gov/," national Nuclear Data Center. [Online]. Available: http://www.nndc.bnl.gov/

[4] M. G. Mayer, *On Closed Shells in Nuclei*, 1948, vol. 74, no. pp. 235-239.

[5] O. Haxel, J. Jensen, and H. Suess, "On the magic numbers in nuclear structure," *Physical Review*, vol. 75, 1766, 1949.

[6] M. Mayer, *Phys. Rev.*, vol. 78, pp. 22–23, 1950.

[7] S. Paschalis, "Relativistic one-nucleon removal reactions," Ph.D. dissertation, University of Liverpool, 2008.

[8] B. Jonson, "Light dripline nuclei," *Physics Reports*, vol. 389, p. 1â[U+0080][U+0093]59, 2004.

[9] A. J. P. Hansen and B. Jonson, *Annual Review of Nuclear and Particle Science*, vol. 45, pp. 591–634, 1995.

[10] I. Tanihata, *Journal of Physics G: Nuclear and Particle Physics*, vol. 22, 2, p. 157, 1996.

[11] B. Jonson, "American institute of physics conference series," *American Institute of Physics Conference Series*, vol. 495, pp. 3–8.

[12] Y. P. M. Zhukov and J. Vaagen, *Physics of Atomic Nuclei*, vol. 65, 4, pp. 746–751, 2002.

[13] J. Al-Khalili, "An introduction to halo nuclei," in *The Euroschool Lectures on Physics with Exotic Beams, Vol. I*, ser. Lecture Notes in Physics, Ernst, Ed. Springer Berlin Heidelberg, 2004, vol. 651, pp. 77–112.

[14] D. F. e. a. A. Jensen, K. Riisager, *Rev. Mod. Phys.*, vol. 76, pp. 215–261, 2004.

[15] O. H. e. a. I. Tanihata, H. Hamagaki, *Phys. Lett. B*, vol. 160, 6, pp. 380–384, 1985.

[16] K. Riisager, "Nuclear halos and experiments to probe them," in *The Euroschool Lectures on Physics with Exotic Beams, Vol. II*, ser. Lecture Notes in Physics, Ernst, Ed. Springer Berlin Heidelberg, 2006, vol. 700, pp. 1–36.

[17] P. Hansen and B. Jonson, *EPL (Europhysics Letters)*, vol. 4, p. 409, 1987.

[18] I. Tanihata, H. Hamagaki, O. Hashimoto, Y. Shida, N. Yoshikawa, K. Sugimoto, O. Yamakawa, T. Kobayashi, and N. Takahashi, "Measurements of interaction cross sections and nuclear radii in the light p-shell region," *Phys. Rev. Lett.*, vol. 55, pp. 2676–2679, Dec 1985.

[19] I. Tanihata, H. Savajols, and R. Kanungo, "Recent experimental progress in nuclear halo structure studies," *Progress in Particle and Nuclear Physics*, 2012.

[20] N. k Glendenning, *Direct Nuclear Reactions*. World Scientific Publishing Co. Pte. Ltd., 2004.

[21] P. Hansen and J. Tostevin, *Annual Review of Nuclear and Particle Science*, vol. 53, pp. 219–261, 2003.

[22] D. Cortina-Gil, "Lecture notes in physics," *Lecture Notes in Physics, Berlin Springer Verlag*, vol. 879, p. 183.

[23] T. Aumann, "Reactions with fast radioactive beams of neutron-rich nuclei," *The European Physical Journal A*, vol. 26(3), p. 441â[U+0080][U+0093]478, 2006.

[24] F. Wamers, "Quasi-free-scattering and one-proton-removal reactions with the proton-dripline nucleus ^{17}Ne at relativistic beam energies," Ph.D. dissertation, Institut Fuer Kernphysik Technische Universität Darmstadt, 2011.

[25] L. Faddeev, *Theor. Fiz.*, vol. 1459, 1960.

[26] P. Grassberger and W. Sandhas, *Nucl. Phys. B2*, vol. 167, 1967.

[27] W. Glockle, *The Quantum Mechanical Few-Body Problem*, B. Springer-Verlag, Ed., 1983.

[28] O. Chamberlain and E. Segrè, *Phys. Rev.*, vol. 87, pp. 81–83, 1952.

[29] J. B. Cladis, W. N. Hess, and B. J. Moyer, *Phys. Rev.*, vol. 87, 425, 1952.

[30] T. Aumann, C. A. Bertulani, and J. Ryckebusch, *Phys. Rev. C*, vol. 88, p. 064610, 2013.

[31] P. FernÃ¡ndez and et.al, "Quasifree (p, pN) scattering of light neutron-rich nuclei near N = 14," *Phys. Rev. C*, vol. 97,024311, 2018.

[32] G. Jacob and T. A. J. Maris, *Rev. Mod. Phys.*, vol. 38, pp. 121–142, 1966.

[33] R. Crespo, A. Deltuva, M. Rodriguez-Gallardo, E. Cravo, and A. C. Fonseca, "Spectroscopy of unbound states under quasifree scattering conditions: One-neutron knockout reaction of ^{14}Be," *Phys. Rev. C*, vol. 79, p. 014609, 2009.

[34] E. Cravo, R. Crespo, A. Deltuva, and A. C. Fonseca, "Resonant and nonresonant breakup of ^{11}Be on a proton target," *Phys. Rev. C*, vol. 79, p. 064610, Jun 2009.

[35] J. A. Tostevin, D. Bazin, B. A. Brown, and et al, *Phys. Rev. C*, vol. 66, p. 024607, 2002.

[36] R. Crespo, E. Cravo, and A. Deltuva, "Three-body calculations for (p, pN) reactions: Kinematically inclusive, semi-inclusive, and fully exclusive cross sections," *Phys. Rev. C*, vol. 99, 054622, 2019.

[37] R. Crespo, E. Cravo, A. Deltuva, M. Rodriguez-Gallardo, and A. C. Fonseca, "Rescattering effects in proton elastic scattering from halo nuclei: A test of the glauber approximation," *Phys. Rev. C*, vol. 76, p. 014620, 2007.

[38] A. Deltuva, A. M. Moro, E. Cravo, F. M. Nunes, and A. C. Fonseca, "Three-body description of direct nuclear reactions: Comparison with the continuum discretized coupled channels method," *Phys. Rev. C*, vol. 76, p. 064602, 2007.

[39] R. Crespo, M. Rodriguez-Gallardo, A. M. Moro, A. Deltuva, E. Cravo, and A. C. Fonseca, "Resonant breakup of ^{19}C on a proton target," *Phys. Rev. C*, vol. 83, p. 054613, 2011.

[40] A. D. R. Crespo and A. M. Moro, *Phys. Rev. C*, vol. 83, p. 044622, 2011.

[41] E. Cravo, R. Crespo, and A. Deltuva, "Valence neutron-core interaction effects on the breakup of halo nuclei," *Phys. Rev. C*, vol. 87, 034612, 2013.

[42] E. Cravo, R. Crespo, and A.Deltuva, "Distortion effects on the neutron knock-out from exotic nuclei in the collision with a proton target," *Phys. Rev. C*, vol. 87, 034612, 2016.

[43] G. Murillo, S. Sen, and S. E. Darben, *Nucl. Phys. A*, vol. 579, p. 125, 1994.

[44] J. D. Goss and et al, *Phys. Rev. C*, vol. 12, p. 1730, 1975.

[45] U. Datta-Pramanik and et al, *Phys. Lett. B*, vol. 551, p. 63, 2003.

[46] T. Nakamura and et al, *Phys. Rev. C*, vol. 79, p. 035805, 2009.

[47] D. Bazin, W. Benenson, B. A. Brown, J. Brown, B. Davids, M. Fauerbach, P. G. Hansen, P. Mantica, D. J. Morrissey, C. F. Powell, B. M. Sherrill, and M. Steiner, "Probing the halo structure of ^{19,17,15}C and ^{14}B," *Phys. Rev. C*, vol. 57, pp. 2156–2164, 1998.

[48] V. Maddalena and et al, *Nucl. Phys. A*, vol. 682, 332c, 2001.

[49] "http://www.nscl.msu.edu/."

[50] "GSI Helmholtzzentrum für Schwerionenforschung GmbH," http://www.gsi.de/.

[51] T. Kubo and et al., *Nucl. Instrum. Methods B*, vol. 70, 309, 1992.

[52] "http://www.riken.go.jp/en/."

[53] E. Sauvan and et al, "One-neutron removal reactions on neutron-rich psd-shell nuclei," *Phys. Lett. B*, vol. 491, p. 1â[U+0080][U+0093]7, 2000.

[54] "www.ganil-spiral2.eu."

[55] "Technical proposal for the design of the *reactions with relativistic radioactive beams* setup," http://www-win.gsi.de/r3b/Documents/R3B-TP-Dec05.pdf, December 2005.

[56] T. R. collaboration, "Neutron-rich nuclei at and beyond the dripline in the range Z=4 to Z=10 studied in kinematically complete measurements of direct reactions at relativistic energies," *S393 Proposal*, 2009.

[57] T. Aumann, "Neutron-rich nuclei at and beyond the dripline in the range Z=4 to Z=10 studied in kinematically complete measurements of direct reactions at relativistic energies," The R^3B Collaboration, Tech. Rep., 2009.

[58] C. Caesar, J. Simonis, T. Adachi, and et al, *Phys. Rev. C*, vol. 88, p. 034313, 2013.

[59] C. Caesar, "Beyond the neutron drip-line: Superheavy oxygen isotopes," Ph.D. dissertation, Technische Universität Darmstad, 2012.

[60] A. Najafi, "Quasi-free proton and neutron knockout reactions in ^{20}O," Ph.D. dissertation, University of Groningen, 2013.

[61] P. FernÃ¡ndez, "An investigation into quasi-free scattering of light neutron-rich nuclei around N=14," Ph.D. dissertation, Universidade de Santiago de Compostela, 2013.

[62] M. Holl, "Quasi-free scattering from relativistic neutron-deficient carbon isotopes," Ph.D. dissertation, Technische Universität Darmstadt, 2014.

[63] M. Holl and et. al, "Quasi-free neutron and proton knockout reactions from light nuclei in a wide neutron-to-proton asymmetry range," *Physics Letters B*, vol. 795, pp. 682–688, 2019.

[64] M. Heine, "Measurement of (n,γ)-rates of light neutron-rich nuclei for the r-process nucleosynthesis," Ph.D. dissertation, Technische Universität Darmstadt, 2015.

[65] M. Heine and et al., "Determination of the neutron-capture rate of ^{17}C for r-process nucleosynthesis," *Phys. Rev. C*, vol. 95, p. 014613, Jan 2017.

[66] G. Ribeiro, "Studies beyond the neutron dripline using quasifree (p,2p) reactions: the case of ^{13}Be," Ph.D. dissertation, CSIC - Instituto de Estructura de la Materia, 2015.

[67] R. Thies, "Prototype tests and pilot experiments for the R^{3}B scintillator-based detection systems," *M.Sc. thesis, Chalmers university of technology, Goteborg, Sweden*, 2011.

[68] R. Thies and et. al, "Systematic investigation of projectile fragmentation using beams of unstable b and c isotopes," *Phys. Rev. C*, vol. 93, 054601, 2016.

[69] J. Boillos, "Quasi-free scattering of light neutron-deficient nuclei," Ph.D. dissertation, Universidade de Santiago de Compostela, 2019.

[70] L. Atar, "Investigation of the single-particle structure of oxygen isotopes in quasi-free knockout reactions at the R^{3}B/land setup," Ph.D. dissertation, Technische Universität Darmstad, 2015.

[71] L. Atar and et al., "Quasifree (p, $2p$) reactions on oxygen isotopes: Observation of isospin independence of the reduced single-particle strength," *Phys. Rev. Lett.*, vol. 120, p. 052501, Jan 2018.

[72] G. Ribeiro and et al., "Structure of ^{13}Be studied in proton knockout from ^{14}B," *Phys. Rev. C*, vol. 98, p. 024603, Aug 2018.

[73] M. Vandebrouck and et al., "Effective proton-neutron interaction near the drip line from unbound states in ^{25,26}F," *Phys. Rev. C*, vol. 96, p. 054305, Nov 2017.

[74] M. Röder and et al., "Coulomb dissociation of ^{20,21}N," *Phys. Rev. C*, vol. 93, p. 065807, Jun 2016.

[75] S. Altstadt and et al., "^{13,14}B(n, γ) via coulomb dissociation for nucleosynthesis towards the r-process," *Nuclear Data Sheets*, vol. 120, pp. 197 – 200, 2014.

[76] J. Alcaraz, B. Alpat, G. Ambrosi, P. Azzarello, R. Battiston, B. Bertucci, J. Bolmont, M. Bourquin, W. Burger, M. Capell *et al.*, "The alpha magnetic spectrometer silicon tracker: Performance results with protons and helium nuclei," *Nuclear Instruments and Methods in Physics Research Section A: Accelerators, Spectrometers, Detectors and Associated Equipment*, vol. 593, no. 3, pp. 376–398, 2008.

[77] K. Blasche, "The heavy ion synchrotron SIS," in *In EPAC 92: Third European Particle Accelerator Conference*, 1992, pp. 9–13.

[78] H. Geissel, "The GSI projectile fragment separator (FRS): a versatile magnetic system for relativistic heavy ions," *Nuclear Instruments and Methods in Physics Research B*, vol. 70, pp. 286–297, 1992.

[79] "Facility for antiprotons and ion research," http://www.fair-center.eu/.

[80] H. T. Johansson, "The DAQ always runs. Licenciate thesis," *Chalmers University of Technology, GÃ¶teborg*, 2006.

[81] V. Metag, "The Darmstadt-Heidelberg-Crystal-ball," *Proc. Geiger Memorial Meeting*, 1982.

[82] V. Metag and et al, "Physics with 4π-γ-detectors," *Nuclear Physics A*, vol. 409, p. 331â[U+0080][U+0093]342, 1983.

[83] L. Collaboration and et al, "A large area detector for high-energy neutrons," *Nuclear Instruments and Methods in Physics Research Section A: Accelerators, Spectrometers, Detectors and Associated Equipment*, vol. 314, p. 136â[U+0080][U+0093]154, 1992.

[84] "Land collaboration website."

[85] D. Rossi, "Investigation of the dipole response of nickel isotopes in the presence of a high-frequency electromagnetic field," *Ph.D. thesis, Johannes Gutenberg-UniversitÃt, Mainz*, 2010.

[86] K. Mahata, H. Johansson, S. Paschalis, H. Simon, and T. Aumann, "Position reconstruction in large-area scintillating fibre detectors," *Nuclear Instruments and Methods in Physics Research Section A: Accelerators, Spectrometers, Detectors and Associated Equipment*, vol. 608, p. 331, 2009.

[87] H. Johansson, "Hunting tools beyond the driplines performing large-scale nuclear physics experiments," Ph.D. dissertation, Chalmers University of Technology, 2010.

[88] "http://web-docs.gsi.de/ rplag/land02/." [Online]. Available: http://web-docs.gsi.de/~rplag/land02/

[89] R. Brun and F. Rademakers, "ROOT - An object oriented data analysis framework," *Nuclear Instruments and Methods in Physics Research Section A: Accelerators, Spectrometers, Detectors and Associated Equipment*, vol. 389, no. 1-2, pp. 81–86, 1997, new Computing Techniques in Physics Research V.

[90] C. Langer, "Coulomb dissociation of ^{31}Cl and ^{32}Ar - constraining the rp process," *PhD thesis, Johann-Wolfgang-Goethe University of Frankfurt, Germany*, 2012.

[91] A. Movsesyan, "Quasi-free one-proton and one-neutron knockout reactions on ^{57}Ni," *Technische Universität Darmstadt*, 2013.

[92] F. Warmers, "Quasi-free-scattering and one-proton-removal reactions with the proton dripline nucleus ^{17}Ne at relativistic beam energies," Ph.D. dissertation, Technische Universität Darmstadt, 2011.

[93] A. Henriques, "Nucleon knockout of 11be ^{11}Be from the collision with a proton target at high energies," Ph.D. dissertation, Faculdade de CiÃªncias da Universidade de Lisboa, 2017.

[94] V. Panin, "Fully exclusive measurements of quasi-free single-nucleon knockout re-actions in inverse kinematics," Ph.D. dissertation, Technische Universität Darmstadt, 2012.

[95] K. Olive and et al, *Chin. Phys. C*, vol. 38, p. 090001, 2014.

[96] R. Plag, *http://ralfplag.de/tracker/*.

[97] "http://www.gsi.de/gsi-future/cdr." [Online]. Available: http://www.gsi.de/GSI-Future/cdr

[98] "Geant4 users' documents," in *Physics Reference Manual*, . ed., Ed., 2015.

[99] S. Qingbiao, "Systematics of nucleon-nucleon total, elastic and inelastic scattering cross sections and elastic scattering angular distributions up to 10 gev," *Tech. rep. China Nuclear Information Centre, Beijing (China)*, 2000.

[100] A. J. Hartzler and R. T. Siegel, *Phys. Rev.*, vol. 185, p. 95.

[101] S. Agostinelli and et al., "Geant4-a simulation toolkit," *Nuclear Instruments and Methods in Physics Research Section A: Accelerators, Spectrometers, Detectors and Associated Equipment*, vol. 506, no. 3, pp. 250–303, 2003.

[102] A. Deltuva, A. C. Fonseca, and P. U. Sauer, "Calculation of proton-deuteron breakup reactions including the coulomb interaction between the two protons," *Phys. Rev. Lett.*, vol. 95, p. 092301, 2005.